Atomic Layer Processing of Thin Film Superconductors for Superconducting Electronics

Thesis by
Azmain Abrawr Hossain

In Partial Fulfillment of the Requirements for the Degree of
Doctor of Philosophy,
Applied Physics

CALIFORNIA INSTITUTE OF TECHNOLOGY
Pasadena, California

2026
Defended March 27

For mumu and my bunbun

Azmain Abrawr Hossain
ORCID: 0000-0002-8441-0183

ACKNOWLEDGEMENTS

I remember how worried I was during summer of 2021 before coming to Caltech. I was yet to pick an advisor or research direction. Out of nowhere I received an email from Austin Minnich to hop on a Zoom call and talk about this new future direction he was planning to pursue. Austin was not even on my radar at this point because his group was doing computational work in different fields. At this point in time I did not truly appreciate Austin's dedication to scientific research. I just thought it was odd for a professor to pursue experimental nanofabrication while doing quantum computing and transport calculations. Little did I know this was not his first time completely changing research direction. Regardless, I met with David who was a G1 at the time. I was surprised by how confident he felt in pursuing work in a completely new field and how much faith he had in Austin's vision. I was sold, and I do not think I have looked back since then. Austin, I want to thank you for all your support and guidance. I appreciate how you would sit with me when I was a G1 trying to make sense of your huge Sciwheel collection. I appreciate how much you value each group member's opinion even when they turn into a heated argument. I do not think we ever argued that aggressively, but I always appreciated how much you respected your graduate students. Thank you for taking the time to guide me and be my Ph.D. advisor, I do not think I could have picked a better one.

I want to extend my gratitude to my thesis committee members, Dr. Mirhosseini, Dr. Falson, and Dr. Kooi for their valuable time and collaboration. I want to thank Mohammad for always stopping by my posters and thinking of ways we can collaborate together. I want to thank Joe for sharing his unparalleled knowledge on UHV systems, and letting us stop by his lab when we need help. I want to thank Jacob for always being a phone call away when I cannot make sense of something. I appreciate it when you call to chat, or just to grab coffee at Red Door. Additionally, I want to thank my other collaborators. Dan Cunnane, for introducing me to MgB_2 and its joys and woes, and for taking me on as your future postdoc. Jonathan Greenfield for training me on the MgB_2 deposition system. I used to look forward to our long chats early in the morning. I also want to thank the KNI staff, especially Kelly and Tiffany for their support.

To the Minnich lab, I want to thank everyone who has helped me during my time at Caltech. Everyone has been amazing and thoughtful. I want to thank David and Haozhe for teaching me when I knew nothing about nanofabrication. Ivy, for

always bringing snacks and smiles, even on bad days. Anthony, for always being there when I need help running an experiment outside my expertise. Mete, for his incredible dedication to his work, for taking on projects I did not have the time for, and for listening when I had no clue what I was saying. Yifei, for starting the MgB_2 project with me. Fin for always having a fun story to share when I would go into the office and for telling me all the latest gossip. Jiayin, for taking the time out of your busy schedule to help with the EBPG and for answering my lithography questions.

Outside of Caltech, I would like to thank my friends for keeping me sane. Thank you Shumit for keeping in touch even when I am terrible at doing so. Thank you for being my sounding board and letting me be yours. Thank you Jiayin, for keeping me humble on the ping pong table table. Hope we all get to try more boba together. To Jonny and Leighton, I still can not believe how we went from wasting away weekends playing BO3 zombies to wasting away weekends playing smash. I could not have picked better people to tutor algebra with.

To mom and dad, thank you for being my parents in another country. Thank you for teaching me how to crab (both catching and eating), how to play hearts, mahjong, and pickleball. Thank you for treating me like your son and accepting me for who I am.

To my beautiful wife Laurie, I am sure you know how I feel. Thank you for your never ending support. Thank you for pouring me water when I finish my cup and forget to refill it because I have been writing all day. Thank you for making dinner when I am in the lab until midnight. Thank you for taking a break and playing video games with me. I will forever be grateful for your love and support. I hope to make your morning coffee for the rest of my life.

Words cannot express my gratitude to baba, ma, and apu. I would not be who I am today if not for you all. Thank you Nasheetah for thinking of me, your kindness and thoughtfulness has always inspired me. Thank you baba for teaching me about life. Thank you ma for teaching me about love and sacrifice. I could never fathom the challenges you endured to migrate to a foreign country for your children's future. Thank you for always caring for me, I love you.

THESIS ABSTRACT

Superconducting thin films are the building blocks of superconducting quantum electronics. State-of-the-art devices such as superconducting qubits, microwave kinetic inductance detectors (MKIDs), and superconducting-insulator-superconducting (SIS) mixers are fabricated using dry etching, typically reactive ion etching (RIE). The microwave performance of MKIDs and qubits is currently limited by interface and surface loss thought to arise from nanofabrication-induced damage and atmospheric exposure. For SIS mixers, it is important to fabricate layers with sub-nanometer etching precision and low surface roughness (< 0.5 nm). However, RIE is generally unable to meet these criteria due to the continuous nature of the etching process and the use of high energy ions. Additionally, RIE has been shown to lead to almost 10 nm of sub-surface damage, which can limit the performance of superconducting devices where the interfaces are critical to performance. In all of these devices, improving etch-depth control and achieving low surface roughness through a low-damage etching process is essential to improving state-of-the-art devices and enabling new device architectures.

In this thesis, we investigate atomic layer processing techniques for thin-film superconductors, namely atomic layer deposition (ALD) and atomic layer etching (ALE) being of special focus. ALD and ALE are nanofabrication methods capable of Angstrom-scale control and result in substantially less damage than standard methods such as RIE. Beyond ALD and ALE, we also develop and investigate a new plasma chemistry to etch magnesium diboride, which previously did not have a known chemical dry etch. We then use these techniques to fabricate superconductor-insulator-superconductor junctions and analyze their current-voltage characteristics.

We first report an isotropic plasma-thermal ALE process for titanium nitride (TiN). While ALE processes for TiN have been reported, they either employ HF vapor, incurring practical complications; or the etch rate lacks the desired Angstrom-scale control. We identify a new etching chemistry for TiN based on sequential exposures of molecular oxygen and an SF_6/H_2 plasma. For certain ratios of SF_6:H_2 flow rates, we observe selective etching of TiO_2 over TiN, enabling self-limiting etching within a cycle. We measure etch rates with *ex situ* ellipsometry, which vary from 1.1 Å/cycle at 150 °C to 3.2 Å/cycle at 350 °C. We further demonstrate that the superconducting critical temperature of the etched film does not decrease beyond that expected from the decrease in film thickness, highlighting the low-damage nature of the process.

These findings are relevant for applications of TiN in microwave kinetic inductance detectors and superconducting qubits. Our ALE chemistry using SF_6/H_2 plasma is applicable to other materials, and is the starting point for studying our next material.

Next we report a plasma-thermal atomic layer etching recipe for niobium nitride (NbN). Prior to this work, no ALE recipe had been reported for NbN, likely due to the complex chemistry of Nb. We develop a self-limiting ALE recipe using sequential exposures of O_2 plasma and H_2/SF_6 plasma, with an etch rate of 1.77 Å/cycle at 125 °C. Exposure to O_2 plasma rather than O_2 gas yields a greater fraction of Nb in the +5 oxidation state, which is then volatilized by NbF_5 formation. The SF_6:H_2 flow rate ratio is chosen to produce selective etching of Nb_2O_5 over NbN. The T_c of ALE-etched NbN is higher than that of an RIE-etched film of a similar thickness. Our low-damage process is ideal for NbN-based single-photon detectors and superconducting microresonators. We now turn our attention to a more exotic superconductor lacking reliable RIE chemistry.

Finally, we investigate new dry chemical etching techniques for magnesium diboride (MgB_2), a superconductor of interest due to its high T_c of 39 K. Most of the reported MgB_2 etching methods are ballistic instead of chemical due to the non-volatile nature of magnesium halides. Physical etching lacks nanometer etch-depth control and can damage the superconducting properties of the film. Due to these reasons, a chemical etch of MgB_2 is highly desirable. We report the use of H_2 plasma to etch boron and MgB_2 at 125 °C with etch rates of 9.5 and 4.4 Å/min respectively. After etching with H_2 plasma, we also find that the films are passivated by a hydride barrier, which impedes the typical T_c degradation upon atmospheric exposure seen in unpassivated MgB_2 films. We also use this barrier to fabricate Nb-MgB_2 hybrid SIS junctions. Current-voltage characteristics of the junction are discussed, where interesting subgap physics is observed, with the capability to diagnose the different gaps that contribute to tunneling in the Nb-MgB_2 junction.

PUBLISHED CONTENT AND CONTRIBUTIONS

1 Azmain A. Hossain, Sela Murphy, David S. Catherall, Anthony J. Ardizzi, and Austin J. Minnich. "Atomic layer etching of niobium nitride using sequential exposures of O_2 and H_2/SF_6 plasmas". *Journal of Vacuum Science & Technology A*, 43(4), July 2025. DOI: 10.1116/6.0004548.
A.A.H. designed the research, conducted the experiments, analyzed the data, and wrote the manuscript.

2 Azmain A. Hossain, Haozhe Wang, David S. Catherall, Martin Leung, Harm C. M. Knoops, James R. Renzas, and Austin J. Minnich. "Isotropic plasma- thermal atomic layer etching of superconducting titanium nitride films using sequential exposures of molecular oxygen and SF_6/H_2 plasma." *Journal of Vacuum Science & Technology A*, 41(6), November 2023. DOI: 10.1116/6.0002965.
A.A.H. designed the research, conducted the experiments, analyzed the data, and wrote the manuscript.

3 David S. Catherall, Yifei Yan, Finley B. Donachie, Azmain A Hossain, and Austin J. Minnich. "Characterization of ultrathin nickel films deposited by thermal laser evaporation."*Applied Physics Letters*, January 2026. DOI: 10.1063/5.0309594
A.A.H. assisted in the collection and analysis of experimental results.

4 Ivy I. Chen, Jennifer Solgaard, Ryoto Sekine, Azmain A. Hossain, Anthony Ardizzi, David S. Catherall, Alireza Marandi, James R. Renzas, Frank Greer, and Austin J. Minnich. "Isotropic atomic layer etching of MgO-doped lithium niobate using sequential exposures of H_2 and SF_6/Ar plasmas." *Journal of Vacuum Science & Technology A*, 42(6), October 2024. DOI: 10.1116/6.0003962.
A.A.H. assisted in the collection and analysis of experimental results.

5 David S. Catherall, Azmain A. Hossain, Anthony J. Ardizzi, and Austin J. Minnich. "Atomic layer etching of SiO_2 using sequential exposures of $Al(CH_3)_3$ and H_2/SF_6 plasma. *Journal of Vacuum Science & Technology A*, 42(5), September 2024. DOI: 10.1116/6.0003793.
A.A.H. assisted in the collection and analysis of experimental results.

6 Haozhe Wang, Azmain Hossain, David Catherall, and Austin J. Minnich. "Isotropic plasma-thermal atomic layer etching of aluminum nitride using SF_6 plasma and $Al(CH_3)_3$". *Journal of Vacuum Science & Technology A*, 41(3), May 2023. DOI: 10.1116/6.0002476.
A.A.H. assisted in the collection and analysis of experimental results.

TABLE OF CONTENTS

LIST OF ILLUSTRATIONS

Number *Page*

Chapter 1

INTRODUCTION

Devices based on superconductivity have found applications in various domains and are constantly pushing the boundaries of scientific research. The main technology that underpins many applications is the Josephson junction. The Josephson junction has paved the way for superconducting quantum bit (qubit) technology for quantum computing, superconducting quantum interference devices (SQUIDs) which are used as ultra-sensitive magnetometers in fields ranging from medicine to geology, and for rapid single-flux quantum (RSFQ) technology in wireless communications [9]. In this thesis we will focus on the use of superconducting electronics for micro- and millimeter-wave radiation detection. These frequencies ranging from approximately 300 GHz – 30 THz play a crucial role across astronomy, communications, Earth science, security, and fundamental physics. Superconducting electronics such as microwave kinetic inductance detectors (MKIDs) [32], and superconducting-insulator-superconducting (SIS) mixers [203] are typically used as detectors in this regime.

In Section 1.1 we build the foundations for understanding some important phenomena in superconductors. We then build upon these foundations to describe the physics of an SIS junction. Most importantly, we will look at how current nanofabrication techniques are limiting the quality of these junctions and how atomic layer processing and new materials can revolutionize SIS junction fabrication.

1.1 Superconductivity

The discovery of superconductivity is often credited to Kamerlingh Onnes for his discovery of a zero resistivity state in liquid helium cooled mercury in 1911 [146]. A key property of a superconductor is the existence of a critical temperature (T_c) below which the electrical resistivity goes to zero. He termed this state 'supraconductivity' which later became superconductivity. This remarkable discovery more than a hundred years ago is still one of the frontiers of modern physics research.

The second key feature of superconductivity is the Meissner effect, discovered by Meissner and Ochsenfeld in 1933 [126]. Once cooled below T_c, a superconductor was found to become a perfect diamagnet, repelling external magnetic fields from

the interior. This effect was soon found to be dependent on the external magnetic field, leading to the observation of a critical field, H_c, above which the superconductor would become a normal metal. Further discoveries were made showing the existence of Type-II superconductors, where above some lower critical field, H_{c1}, flux vortices formed in the superconductor, allowing the material to remain at zero resistivity while maintaining some non-zero magnetic field internally. The type-II superconductor was found to remain a superconductor until the field exceeded some higher critical field, H_{c2} [60].

Using these physical phenomena, two important theoretical frameworks were developed. In 1935, the London equations were published to describe the electrodynamics in a superconductor [111].

$$\frac{\partial}{\partial t}\mathbf{J_s} = \frac{n_s q^2}{m}\mathbf{E} \tag{1.1}$$

$$\nabla \times \mathbf{J_s} = -\frac{n_s q^2}{m}\mathbf{B} \tag{1.2}$$

J_s is the supercurrent density, n_s is the density of supercurrent carriers, q and m are the charge and mass of the supercurrent carriers, respectively. Equation (1.1) describes perfect conductivity with no resistance, and Equation (1.2) can be combined with Ampere's Law to obtain $\nabla^2\mathbf{B} = \lambda^{-2}\mathbf{B}$. The general solution to this leads to a decaying magnetic field inside a superconductor given by $B(z) = B(0)e^{-z/\lambda}$, where z is the thickness dimension of the superconductor. The main outcome of this analysis is the idea that a magnetic field inside a superconductor decays over a length scale called the London penetration depth, described by Equation (1.3).

$$\lambda = \sqrt{\frac{m}{\mu_0 n_s q^2}} \tag{1.3}$$

So, the London equations can be used to explain both perfect conductivity and diamagnetic properties of a superconductor, but not the existence of H_c or Type-II superconductors.

In 1950, Ginzburg and Landau (GL) treated superconductivity as a second-order phase transition and expressed the superconductor's free energy as the function of a complex variable [58]. This variable is called the superconducting order parameter, $\psi = \sqrt{n_s}e^{i\phi}$, where $|\psi|^2$ gives the supercurrent carrier density, and ϕ describes the

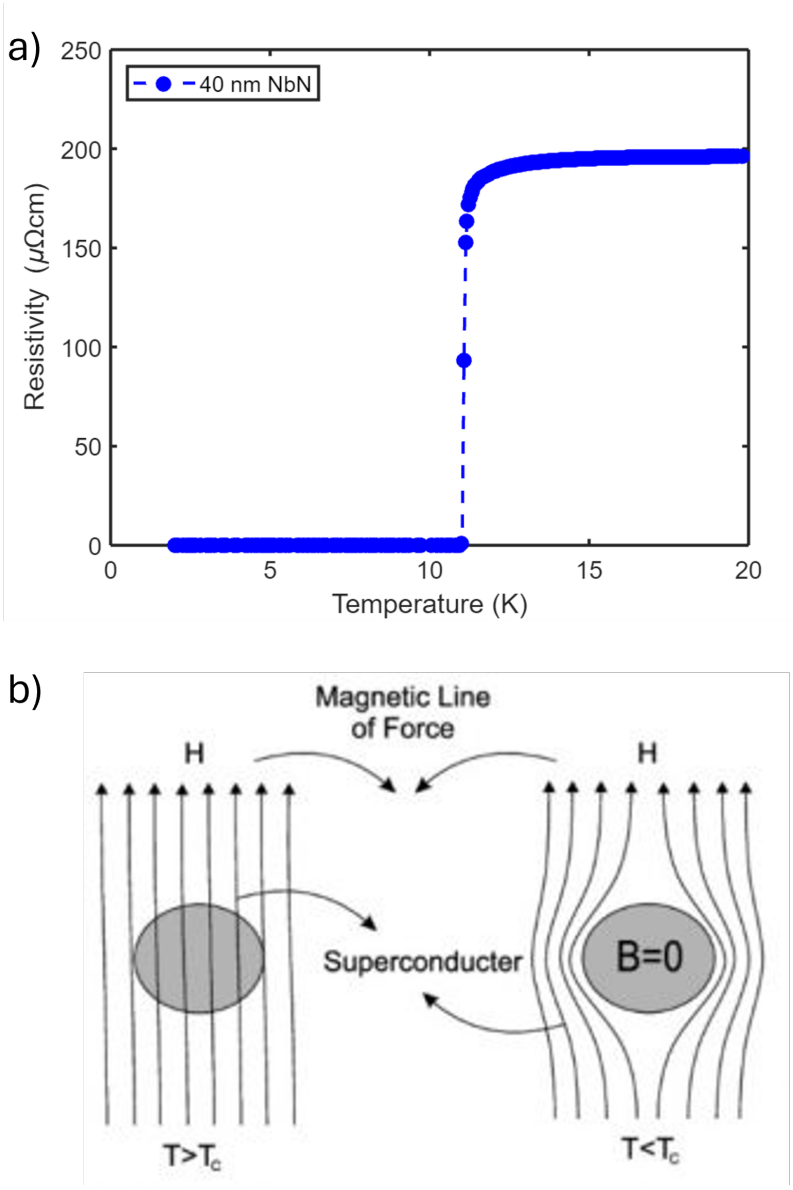

Figure 1.1: a) Resistivity versus temperature plot for a 40 nm NbN film showing a rapid drop in the resistivity and becoming a superconductor below T_c = 11 K. b) Schematic showing a material repelling external magnetic fields below its T_c. Additionally, $B = \mu_0(1 + \chi)H$ goes to zero as the magnetic susceptibility of a superconductor approaches -1.

phase of the order parameter. The phase will be relevant in the Josephson effect discussion Section 1.1. By assuming the superconducting phenomenon known at present such as the existence of H_c, GL theory arrived at two length scales for describing any superconductor. The first is the London penetration depth in Equation (1.3). The second length scale is the scale over which the superconducting wavefunction 'heals' itself after being perturbed, called the GL coherence length. The coherence length is temperature dependent and is given by Equation (1.4).

$$\xi = \sqrt{\frac{\hbar}{q}\frac{1}{\mu_0 H_c}} \tag{1.4}$$

In 1957 Abrikosov used GL theory to calculate the conditions that favor the formation of flux vortices. This led to a unitless parameter, $\kappa = \lambda/\xi$, where $\kappa > \frac{1}{\sqrt{2}}$ is required for Type-II superconductors [1].

It is important to note that while the London and GL frameworks may explain some of the properties of a superconductor, they are phenomenological and do not provide any microscopic explanation for the behavior. The understanding of superconductivity reached a major milestone with BCS theory in 1957 [10]. Simply put, BCS theory stated that electron-phonon interaction results in a weak attraction between electrons. The simplified microscopic image that accompanied this theory was that as an electron moved through a lattice, the negatively charged electron attracted the positively charged ions slightly and shrunk the lattice spacing locally. The first electron moved away from the region before any interaction with the lattice took place, but the smaller lattice spacing increased the charge density in that region, which in turn attracted a second electron. This second electron would then be bonded to the first as it moved in the first electron's positively charged shadow. At low enough temperatures in certain materials, this phonon-mediated attraction can result in the formation of bound electron pairs called Cooper pairs. These Cooper pairs were shown to be bosons, which form a ground state condensate making all the Cooper pairs merge into one quantum mechanical wavefunction. A single particle excitation above this condensate ground state (superconducting state) requires some minimum energy. This minimum energy is called the superconducting energy gap (not too dissimilar from the bandgap of a semiconductor), where an excitation of energy 2Δ is needed to break the Cooper pair. Δ is also temperature-dependent and given by Equation (1.5) at 0 K. The formation of Cooper pairs further explained

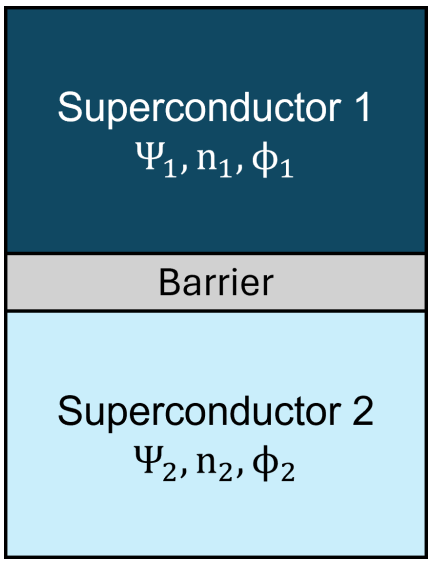

Figure 1.2: Schematic representation of two superconductors separated by a thin barrier. Each superconductor has some Cooper pair density, n, and some phase, ϕ.

why the charge of the supercurrent charge carrier was found to be $q = 2e$, in prior equations.

$$2\Delta_0 = 3.52\ k_B T_c \tag{1.5}$$

This excitation idea can be thought of as analogous to semiconductors, where an electron is excited away from the conduction band to form an exciton. In superconductors, Cooper pairs are excited away from the ground state to form quasiparticles (QP). The superconducting energy gap is on the order of an meV or more, which inhibits the kind of collision interactions that lead to ordinary resistivity, causing superconductivity.

Josephson and SIS Junctions

In 1962, B. Josephson argued using BCS theory and quantum tunneling that it should be possible for Cooper pairs to tunnel across a barrier between two superconductors in the absence of a potential difference [81]. Josephson's prediction was noteworthy because, naively one would expect the current traversing a barrier to be dissipative. However, he predicted that the Cooper pairs could 'leak' into the barrier and allow a dissipation-less supercurrent to flow from one superconductor to the other. The setup for the problem is shown in Figure 1.2. Josephson junctions (JJ) can be

made of superconductor-insulator-superconductor (SIS) or superconductor-metal-superconductor (SNS) stacks. We will focus on SIS type junctions in this thesis.

A single wavefunction is used to describe each superconductor, $\Psi_k = \sqrt{n_k}e^{i\phi_k}$, where n_k is the Cooper pair density in the corresponding superconductor, and ϕ_k is its phase (similar to GL theory). By assuming some arbitrary coupling between the two wavefunctions, one can derive the Josephson equations. Symmetric electrodes ($n_1 = n_2$) are also assumed below:

$$I = I_c \sin(\phi) \tag{1.6}$$

$$\partial_t \phi = \frac{2e}{\hbar} V(t) \tag{1.7}$$

$\phi = \phi_2 - \phi_1$ is the difference in the phase of the two wavefunctions, and I_c is called the critical current. Equation (1.6) describes the current flowing across the junction, and Equation (1.7) describes how an applied bias across the junction can affect the phase difference between the two superconductors. For $V = 0$, ϕ is a constant, and therefore a constant current can be measured across the junction. Depending on the phase factors (which can be manipulated by an external magnetic field or other methods), the current at zero voltage can reach a maximum of I_c. This is the DC Josephson effect. For a constant non-zero voltage, we can integrate Equation (1.7) from zero to some time t and plug the result into Equation (1.6). Thus, we get the AC Josephson effect, where ϕ_0 is the phase difference before any bias is applied.

$$I(t) = I_c \sin(\phi_0 + \frac{2e}{\hbar} Vt) \tag{1.8}$$

Equation (1.8) tells us that when a constant voltage is applied, we get a current across the junction that is oscillating in time, with a frequency of $\omega_J = \frac{2eV}{\hbar}$.

Josephson junctions are now regularly used as a circuit element in various devices in quantum sensing and quantum computing due to its ability to host quantum phenomena on a macro scale. In this thesis the primary application area we will discuss is the use of superconducting junctions as micro- and millimeter-wave radiation detectors. The natural frequency of JJs, $\omega_J = 484$ GHz/mV is in the right range for microwave detection using Cooper-pair tunneling. However, Cooper-pair tunneling is non-dissipative, making it inefficient for photon absorption due to

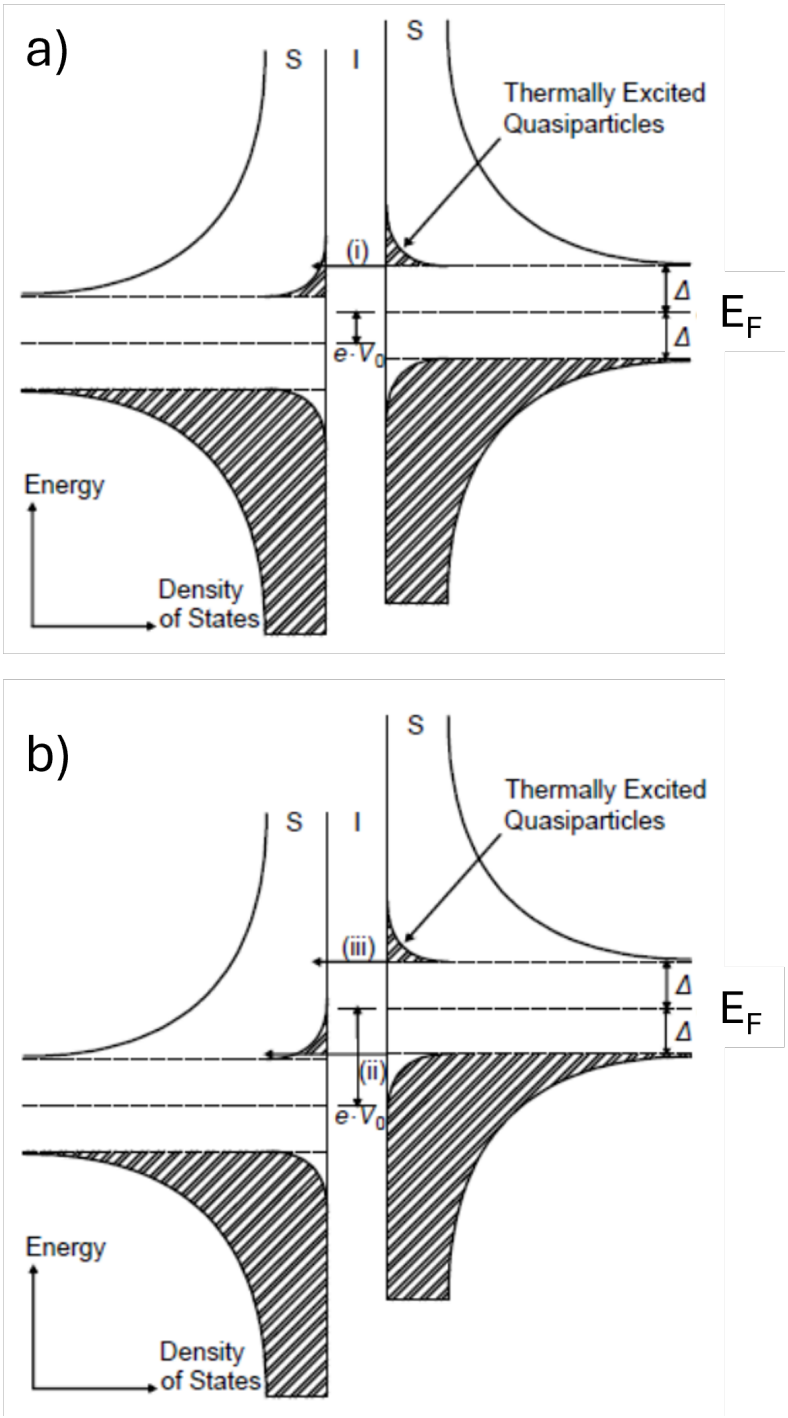

Figure 1.3: The semiconductor picture showing the density of states versus energy for the different layers of an SIS junction. The materials are labeled by S for superconductor and I for insulator on top of each figure. a) A bias V_0 is applied such that $eV_0 < 2\Delta$. b) The bias is now increased such that $eV_0 = 2\Delta$. The figure is motivated by Ref. [186] and Ref. [178].

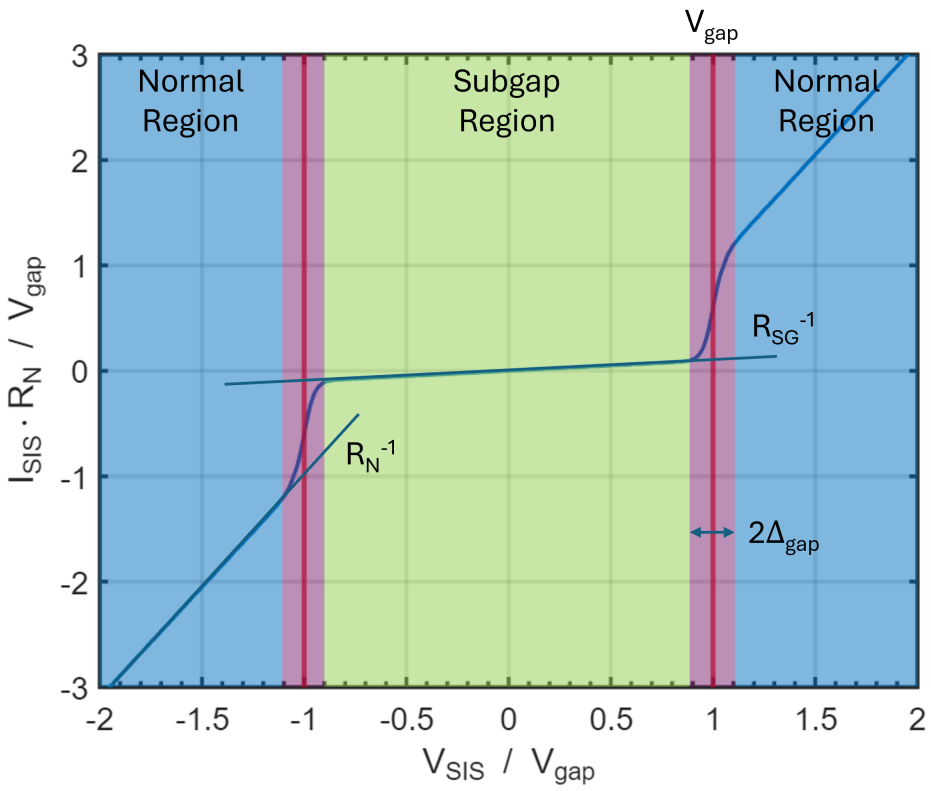

Figure 1.4: IV curve showing $I \cdot R_n/V_{gap}$ versus V/V_{gap}. Three distinct regions are shown: the subgap region (green), the transition region (purple), and the region of normal resistance (blue).

re-emission. Cooper pair tunneling also adds noise to the signal which requires additional suppression [70]. This leads us to the use of quasiparticle (QP) tunneling in SIS junctions.

Side note: A superconducting tunnel junction is called a JJ if Cooper pair tunneling is the main current measured across the junction, and called an SIS junction if QP tunneling is the main current measured across the junction. Physically however, they are the same structure.

SIS mixers are used as heterodyne mixers to shift the signals of mm-wave spectra down to microwave frequencies that are favorable for digital processing. SIS junctions have been shown to operate as quantum limited mixing elements with noise temperature approaching $\frac{hf}{2k_B}$ [100]. To qualitatively understand QP tunneling in SIS junctions it is useful to look at the energy diagram of a superconducting junction in Figure 1.3. No states are available in the insulator, while the superconductors have states available outside of an energy gap, Δ, around the Fermi surface, E_F.

Figure 1.3a shows the semiconductor picture with some applied bias, such that $eV_0 < 2\Delta = V_{gap}$. In this situation the Cooper pairs in the right superconductor cannot tunnel to the left superconductor due to energy conservation. However, there are thermally excited QPs that can tunnel across as QPs from the right side to the left side (arrow i in Figure 1.3a). This results in current flow where there should be none. This effect is called leakage current and occurs in the subgap regime ($eV_0 < V_gap$). Additionally, for a hybrid junction where the two superconductors are different, the gap voltage is described by $eV_{gap} = \Delta_1 + \Delta_2$, since the superconducting bandgap, Δ, is material dependent [178]. By setting $V_0 = 0$, we recover the Josephson effect, where Cooper pairs can tunnel across as the ground state condensate is at the same level. In Figure 1.3b $V_0 = V_{gap}$, now Cooper pairs below the energy gap can tunnel across from the right superconductor to the left as QPs (arrow ii). Additionally, thermally excited QPs can still tunnel across (arrow iii). While this qualitatively describes the QP tunneling effect, a full quantum mechanical treatment can be found in Refs. [177, 178].

The result of such tunneling manifests in an IV curve shown in Figure 1.4. The IV curve is symmetric about the origin and has three regions of interest.

- The subgap region, $|V| < V_{gap} - \Delta_{gap}$.
- The transition, $|V| \approx V_{gap} \pm \Delta_{gap}$.
- The normal region, $|V| > V_{gap} + \Delta_{gap}$.

In the subgap region, we see some non-zero current caused by thermally excited QPs tunneling across the barrier. The slope of the curve in this region gives the inverse of the subgap resistance, R_{SG}^{-1}. The subgap leakage current is given by Equation (1.9), where $g(x) = \sinh(x) \cdot K_0(x)$, and $\Delta = eV_{gap}$. The leakage current is mostly dependent on $\frac{k_B T}{eV_{gap}}$, such that decreasing T or increasing the V_{gap} exponentially suppresses the leakage current.

$$I_{sg}(V_0) = \frac{2}{eR_N} e^{-\Delta/k_B T} \frac{eV_0 + \Delta}{\sqrt{1 + \frac{eV_0}{2\Delta}}} \cdot g\left(\frac{eV_0}{2k_B T}\right) \tag{1.9}$$

The transition through V_{gap} is a non-linear region with some width, Δ_{gap}. Above V_{gap} superconductivity is broken and the resistance approaches that of a normal metal. The slope of the curve in this region is equal to the inverse of the normal

resistance, R_N^{-1}. The curve in this region follows Ohm's Law, leading to a linear IV curve.

In order for an SIS junction to be an effective heterodyne mixer with low noise, a strong non-linearity near V_{gap} is desired. This non-linearity is quantified using two quality factors. The first is the subgap ratio or resistance quality factor, Q_R, and the second is the IV quality factor, Q_{IV}.

$$Q_R = \frac{R_{SG}}{R_N} \tag{1.10}$$

$$Q_{IV} = \frac{I(V_{gap} + \Delta_{gap})}{I(V_{gap} - \Delta_{gap})} \tag{1.11}$$

The subgap ratio is more commonly used, but in both cases a high Q is desirable. Quantum-limited mixers have been demonstrated with $Q_R \geq 10$, while state-of-the-art junctions have also been reported with $Q_R \gtrsim 30$ using atomic layer deposition (ALD), and other unique deposition methods with no vacuum breaks [100, 184]. Both quality factors are dependent on material and fabrication properties. Transitions with $Q_{IV} < 5$ are caused by poor interfaces between the superconductor and insulator. Interface issues can lead to weaker local superconducting properties, such as reduced local T_c and increased superconducting transition width near the metal-insulator interface [122]. The interface issues can be attributed to contamination during deposition or etching, non-uniform interfaces from either a rough superconductor surface or rough dielectric surface ($R_q \gtrsim 2$ nm). Poor Q_R can similarly be explained by a high leakage current resulting in a low $R_{SG} < 5$. Low R_{SG} is often caused by issues in the barrier [122]. A barrier too thin is likely to have high surface roughness ($R_q \gtrsim 1$ nm) or pinholes, which can lead to high QP leakage through some parts of the junction. However, a barrier too thick will inhibit tunneling and reduce V_{gap}. Another significant metric is V_{gap} itself, as it is the upper bound for photon energy that can be detected by the SIS mixer. Increasing V_{gap} by using materials with higher T_c will result in an immediate increase in the bandwidth of the mixer. These interface and material related issues bring us to the heart of this thesis.

Interface, material, and surface issues in superconducting electronics are not limited to SIS mixers but appear in many other superconducting devices. In this thesis we study atomic layer processing methods in order to develop ultra-low damage, conformal, and smoothing deposition and etching methods that provide Angstrom-scale

thickness control. We study the effect of these processes on the surface morphology, chemistry, and transport properties of thin film superconductors typically used in superconducting electronics. In Section 1.2 we introduce the atomic layer processing methods used in this thesis.

1.2 Atomic layer processing for quantum devices

The way we investigate, understand, and manipulate materials at nanometer scales has led to the rapid development in nanotechnology. The progress made in nanotechnology has been largely enabled by the development of thin-film technology, using dielectric, metal, and insulating films with typical thicknesses ranging from microns to sub-nanometers. The development of advanced nanotechnology has allowed the investigation of various phenomena at the nanometer scale. Devices and patterns made by deposition, etching, and masking of thin films have allowed for progress in several fields, from astronomy to communications to biology. One cornerstone of nanoscience is Moore's 1965 prediction, which has had a tremendous effect on not just semiconductor manufacturing but society as a whole [183]. Constant improvements in nanotechnology allowed for the downscaling of integrated circuit fabrication, which has brought device feature sizes in the present to the atomic scale. However, processing on the atomic scale has many challenges. To address these challenges, deposition, lithography, and etching technologies and methods need to be advanced to the atomic scale. [18, 51, 86].

In this thesis we use atomic layer processing as a term to cover atomic layer deposition and atomic layer etching. Atomic layer processing has both been studied extensively for materials in the semiconductor industry [51, 84]. However, very few studies have been conducted on materials relevant to quantum devices [22, 113, 167]. Atomic layer processing is of significant benefit to quantum devices due to its Angstrom-scale depth control and smoothing effect. State-of-the-art quantum devices are currently performance limited by sub-nanometer to nanometer-scale imperfections. In quantum optics, the resonator quality factor is currently limited by scattering from sidewall roughness in SiO_2, SiN_x, lithium niobate, and other optical devices [150, 189, 201]. In superconducting devices based on microresonators, such as qubits and microwave kinetic inductance detectors, the device quality factor is limited by loss from two-level systems (TLS). The parasitic TLS currently limiting device performance is thought to reside in the $1-4$ nm native oxides and few nm thick nanofabrication-induced damaged layers [11, 47]. Nanofabrication-induced damage has also been shown to affect the internal efficiency of superconducting

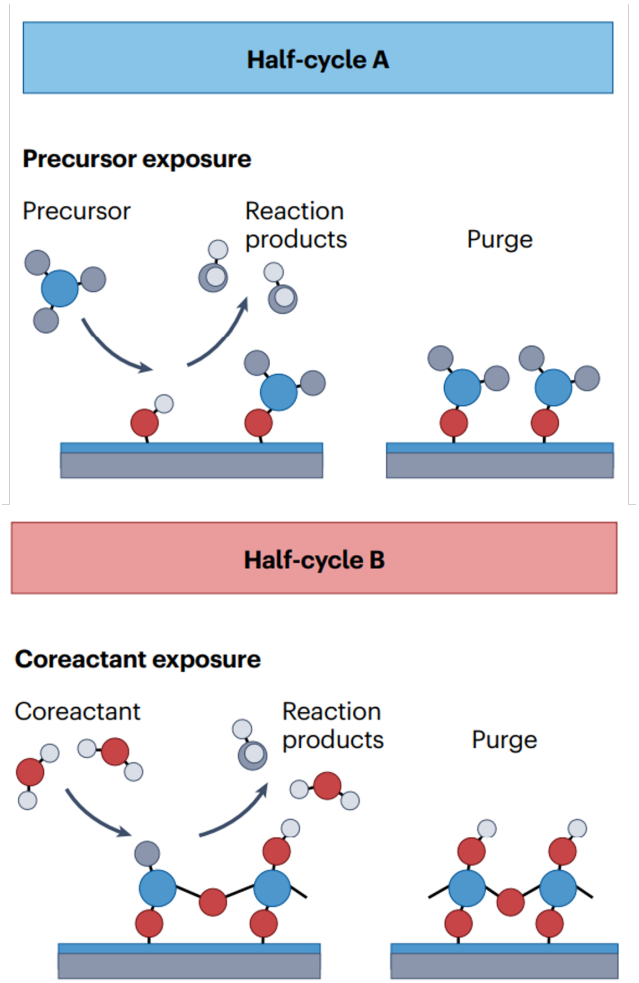

Figure 1.5: A schematic representation of an atomic layer deposition cycle in which a surface is alternately exposed to a precursor (half-cycle A) and a coreactant (half-cycle B). These two reaction steps are separated by purge steps. (Reprinted from Ref. [89], Copyright 2025 Springer Nature.)

nanowire single photon detectors (SNSPDs) by increasing sidewall roughness from etching [46]. The ability to make thin and smooth dielectrics is also of interest for making Josephson junctions in qubits and single photon detectors with high yield, consistency, and low pinhole density [14, 184]. ALD and ALE mechanisms are discussed in the subsequent sections.

Atomic Layer Deposition

Atomic layer deposition (ALD) is a vapor-phase deposition technique that uses sequential self-limiting reactions to produce atomic scale layer-by-layer growth. The discovery of ALD is somewhat debated, as it was invented independently under

two different names: in the 1970s, Suntola coined the term "Atomic Layer Epitaxy", and in the 1960s, Aleskovskii investigated "Molecular Layering" [119, 156]. Led by Suntola and others, ALD started as reactions based on single element reactions between Zn and S to form ZnS for electroluminescent flat panel displays [176]. Shevjakov *et al.* used the reaction between halides and water to form oxides, such as $TiCl_4$ and H_2O to grow TiO_2 [119]. Interest in ALD increased gradually since its discovery and started to take off in the 1990s and early 2000s due to the interest in ALD for scaling down microelectronics. In particular, ALD growth of oxides such as HfO_2 and Al_2O_3 for use as high dielectric constant oxides for thin gate electrodes, and passivation layers is what has made ALD such a workhorse in the semiconductor industry today [116]. Since the original work almost 50 years ago, ALD is now used regularly in industry in many forms, such as thermal ALD, plasma-enhanced ALD, spatial ALD, atmospheric ALD, and others [51, 89].

Figure 1.5 shows a typical binary reaction sequence, which is the most common type of ALD sequence used to deposit binary compounds of the form AB. The precursor in half-cycle A adsorbs to the surface. Saturation can be achieved in this step by increasing the time and/or pressure in this step to achieve maximal coverage of the surface. The precursor introduces the metallic compound A, and the unadsorbed precursors are purged. Half-cycle B then starts, and another reactant is introduced, which reacts with the precursor to remove the undesired parts of the precursor (often organic ligands or halides). The second reactant, commonly called the coreactant, often provides the B part of the desired compound. B is usually an oxide, nitride, sulfide, or halide [88]. Excess reactant is purged, and the cycle is repeated from half-cycle A [51, 89]. For any reaction to go to completion over the entire surface of the wafer, the reactant and coreactant must adsorb to the surface. After physisorption of the molecule, a chemical reaction is thought to occur by three main mechanisms that lead to chemisorption [155].

1. Dissociation: the molecule dissociates into several adsorbed species on the surface without releasing reaction products into the vapor phase

2. Association: the bonding of an intact molecule with the surface without release of ligands

3. Ligand exchange for organic precursors: the surface molecules and the organic groups (ligands) on the precursor react, where the organic groups are exchanged, leading to volatile reaction products

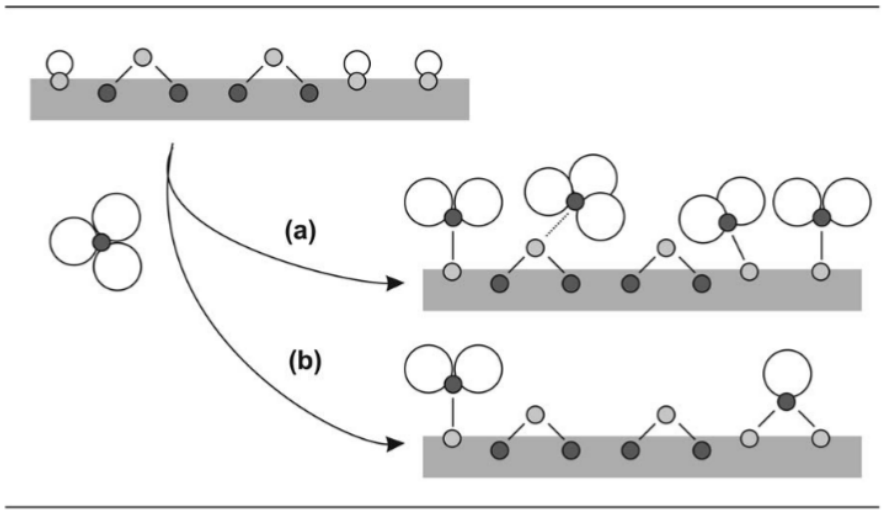

Figure 1.6: Premature saturation of the surface caused by a) steric hindrance of ligands, and b) number of reactive surface sites. (Reprinted from Ref. [155], Copyright AIP Publishing)

Thermal ALD is the most widely used and well studied ALD mechanism. For example, Al_2O_3 is often grown using thermal ALD by dosing $Al(CH_3)_3$ (TMA) in step A and water vapor in step B. Part of the TMA undergoes (-CH_3) ligand exchange with the surface reactive sites (-OH) to form CH_4 gas and a dangling -O-Al($(CH_3)_2$ molecule. This molecule no longer reacts with incoming precursor. The dosing of sufficient precursor leads to the occupation of virtually all the available surface sites until the surface is covered with precursor ligands. Unreacted precursors are purged, and then water is dosed. The water reacts with the dangling molecules to form more methane that is pumped away. Al-O and Al-OH bonds on the surface then act as the sites for ligand-exchange in the next cycle [155]. However, a typical ALD cycle in this method will result in growth of less than one monolayer per cycle. This is due to effects that suppress full coverage of the film. Two factors have been identified to cause the premature saturation of the surface with adsorbed precursors: steric hindrance of the ligands and the number of reactive surface sites [155]. Steric hindrance of the ligands can cause the ligands of the chemisorbed precursor to shield part of the surface from being accessible to the unreacted precursor. The surface is then considered "full." The number of bonding sites on the surface may also be less than that required for achieving the maximum ligand coverage, due to a lack of -OH terminations. In that case, although space remains available on the surface, no bonding sites are accessible. Both effects are illustrated in Figure 1.6.

The advantages of ALD are precise thickness control at the Ångstrom-scale. In saturated ALD recipes, the self-limiting aspect leads to conformal deposition. The conformal deposition has also been observed to lead to reduced surface roughness in the final surface compared to the starting surface [54]. However, achieving the reaction in half-cycle B using only molecular reactants requires higher temperatures, reactive precursors to react with the coreactants, and long purge times due to the high pressures needed to take reactions to completion. For these reasons, in many instances half-cycle B uses a plasma instead of a thermal molecular reaction. The use of plasma in half-cycle B creates charged particles such as electrons and ions, as well as neutral gas-phase species such as radicals, atoms, and molecules. The plasma creates more reactive species than a neutral molecule, which allows for faster saturation in step B. The overall process is then called plasma-enhanced ALD (PE-ALD). The main advantages of PE-ALD over thermal ALD are: the ability to use a lower temperature during deposition, improved film properties due to more surface reactions driven to completion and precursor ligand removal, reduced purge times leading to shorter cycle times, and the use of organometallic and other precursors that are unreactive to molecular reactants [152]. Due to these advantages, PE-ALD has found use in superconducting electronics by deposition of conformal thin-film superconductors for superconducting electronics [42, 97, 167] and dielectrics for Josephson junctions [184]. However, the use of plasma is also a drawback in PE-ALD due to its added complexity. The use of plasma creates multiple reaction pathways and heating effects that are difficult to model and study *in situ*. This has led to most of its advantages and results being described using empirical evidence.

Atomic Layer Etching

Alongside deposition, etching is necessary to create patterned devices by removing material. Etching is typically done using a wet or dry process. In wet etching, the film is placed in a solution that contains the etchant. In dry etching, the film is etched away by vapor species, and is typically carried out at low pressure ($\lesssim 2$ Torr). While wet etching is simple to use, it has some major disadvantages: timing is often manual, there can be local changes in etch rate due to stirring and evaporation, etch is always isotropic so vertical sidewalls cannot be obtained, increased surface roughness due to continuous etching, and etch products remain in the solution which can affect the etch through redeposition or other means. Such issues make achieving sub-nm etch depth control through wet etching almost impossible [38].

In dry etching, either a molecular phase etchant or a plasma is used. Dry etching

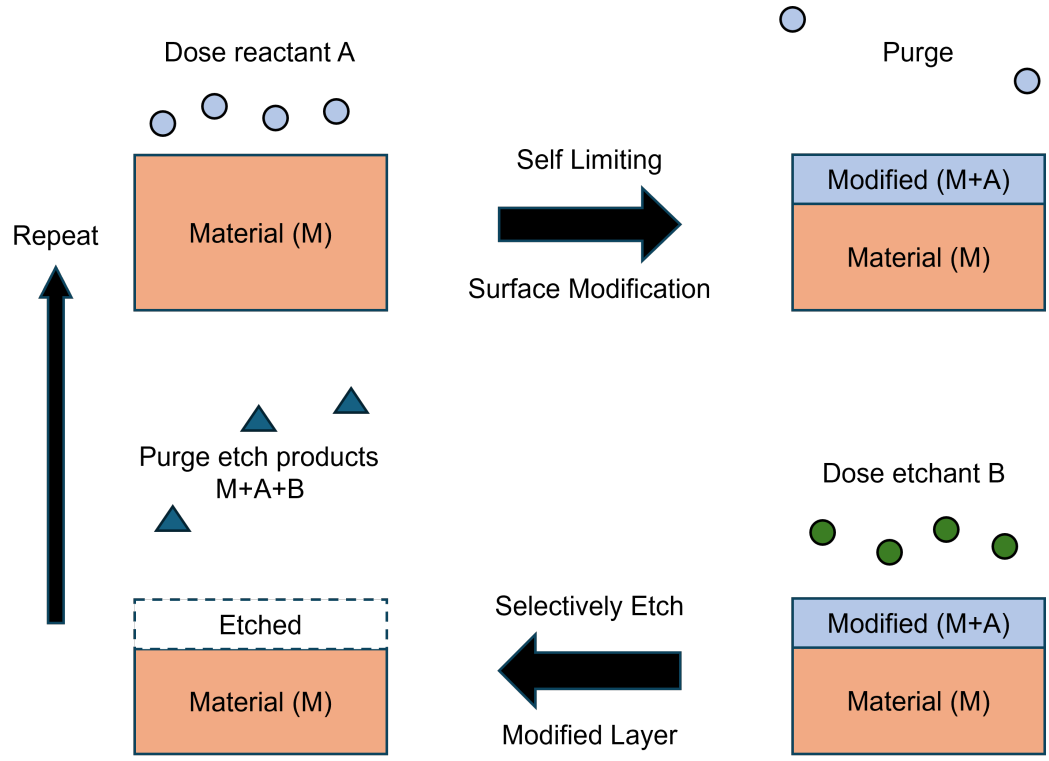

Figure 1.7: Schematic of a general atomic layer etching recipe, showing the four main steps. Dosing species A to modify the surface of some material M. Purge unreacted A and then dose the etchant of the modified surface. B reacts with M+A to form M+A+B volatile compounds that result in a self-limiting etch of Angstrom-scale thicknesses. Purge unreacted B and byproducts to start the cycle again.

has a number of advantages over wet etching: the reaction products of dry etching are typically volatile and pumped away in a vacuum, and due to the absence of a liquid processing temperature can be varied from cryogenic to hundreds of °C [144]. When using a plasma to etch, the plasma parameters and gas chemistry can be varied to make the etch more directional or isotropic as needed. Dry etching can also be performed without a chemical etchant, called ion milling or ballistic etching. A biased Ar plasma is often used in Ar milling to ballistically remove material using the kinetic energy of charged ions. In reactive ion etching (RIE), the chemical and physical nature of dry etching is combined. The reacted top layer is more weakly bonded to the bottom layers and is more easily milled away. This enables the use of lower power to obtain high directionality in the etch. RIE is commonly used by the semiconductor industry to achieve fast, reproducible etch rates [144]. However, even RIE processes struggle to obtain sub-nm or even single nm etch depth control in some cases, and have been shown to lead to ~ 10 nm of sub-surface damage [84, 86, 109]. RIE damage has been shown to limit the performance of

semiconductor, optical, and superconducting devices [94, 132, 161]. Therefore, an ultra-low damage etch process with Angstrom-scale etch depth control is desired in many applications to improve the functionality of devices and consistency of nanofabrication.

Atomic layer etching (ALE) is an emerging nanofabrication process with the potential to overcome the limitations of typical wet and dry etching [84, 86, 109, 143]. The etching counterpart of ALD was first reported by M. Yoder in 1988 for etching diamond [193]. Soon after, multiple papers were published in the 1990s with a focus on directional ALE as an alternative to RIE [73, 117, 160]. The idea was to separate the two effects of RIE that cause etching in order to create an etching method that would need at least two steps to remove material. Thus, ALE was born as "the inverse of ALD", where self-limiting subsequent cyclic steps are employed to remove material, shown in Figure 1.7. Directional ALE is based on surface modification by adsorption of a reactive species such as fluorine or chlorine, and subsequent sputtering of the modified surface with directional ions or neutral atoms of low energy exceeding only the sputtering threshold of the modified surface, as shown in Figure 1.8 [84, 143]. After this period of interest in directional ALE, there is a lull in the number of publications until renewed interest following the isotropic thermal ALE of alumina [105].

Thermal isotropic ALE processes rely on sequential, self-limiting surface chemical reactions without the requirement of plasma exposures [52, 53]. In thermal isotropic ALE, the film surface is modified to form a non-volatile layer that can then be removed through various selective mechanisms, as shown in Figure 1.9. The first report of thermal ALE used ligand-exchange transmetalation reactions [105]. There is also temperature cycling [129, 173], selective halogenation [74, 74], and others [52]. Since then, plasma-thermal ALE has also been reported in which radical species from a plasma are used for modification or volatilization [19, 22, 26, 185]. Isotropic thermal and plasma ALE processes have now been reported for various dielectrics, metals, and semiconductors such as Al_2O_3 [107], SiO_2 [19, 34], InP [98, 148], GaAs [6, 98], Cu [131, 168], W [80, 190], and others [45, 151, 162]. Surface smoothing of etched surfaces using ALE has also been reported for various metals and semiconductors [54, 85, 145, 204]. ALE is fundamentally less subject to process variability induced by transport limitations when compared to RIE, a direct consequence of the use of self-limiting cyclic steps. Although several ALE processes have been reported and mechanisms studied for materials relevant to the

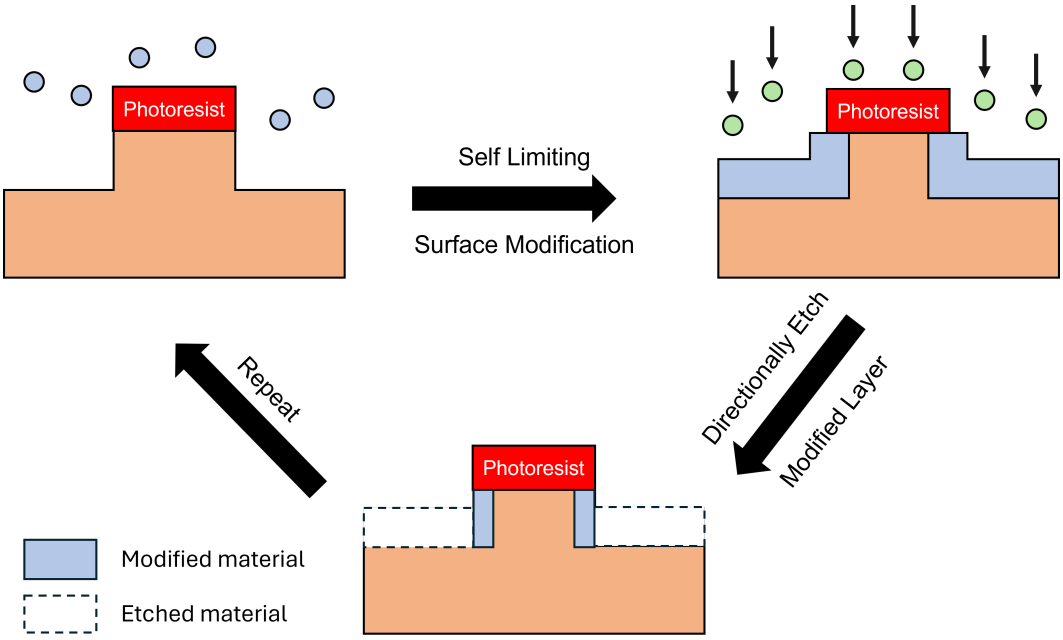

Figure 1.8: Schematic of a directional ALE process showing the accelerated directional particles in the second step, which lead to anisotropic removal of the modified blue surfaces. This leads to minimal undercut of the resist.

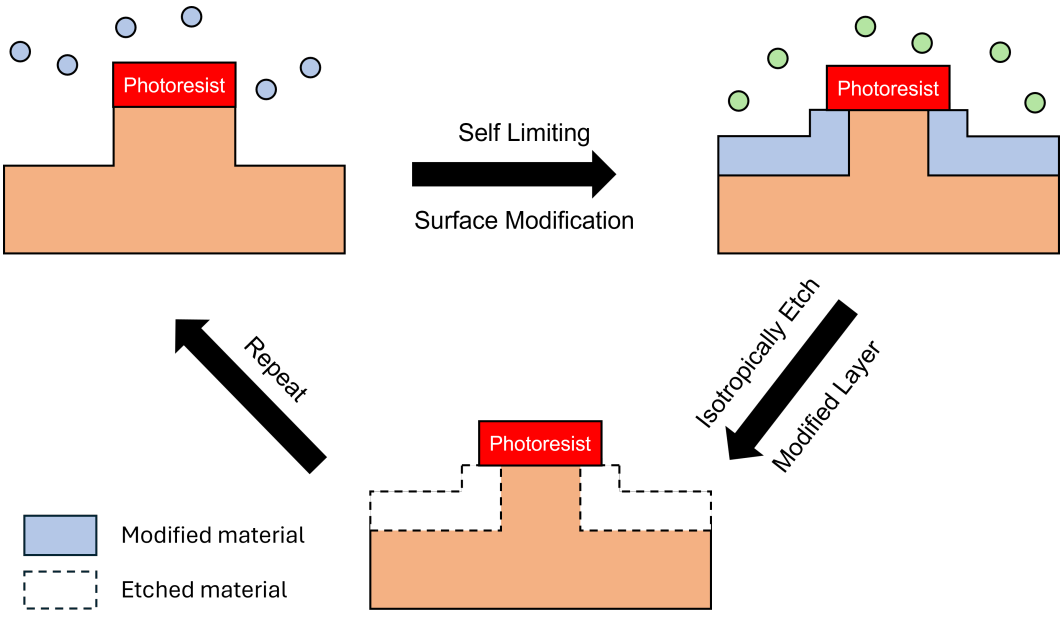

Figure 1.9: Schematic of an isotropic ALE process showing the non-directional species used in the second step, which leads to isotropic removal of the modified blue surface. This leads to some undercut of the resist.

semiconductor industry [84, 143], fewer studies have focused on materials relevant to quantum devices [22, 74], let alone superconducting thin films.

1.3 Thesis outline

In this thesis we develop atomic layer processing tools for titanium nitride and niobium nitride. We also explore novel approaches to etch a more exotic superconducting metal, MgB_2. Finally, we use these processes to fabricate superconductor-insulator-superconductor junctions and examine their current-voltage characteristics.

In Chapter 2, we focus on the ALD and ALE of titanium nitride. Titanium nitride has a high kinetic inductance, low microwave loss, and high absorption coefficient in the infrared and optical frequencies. These properties make it a promising material for single photon detectors such as microwave kinetic inductance detectors and qubits. In these applications, the quality factor for the superconducting resonator is thought to be limited by microwave surface loss associated with two-level systems (TLS) in various interfaces. Subtractive nanofabrication methods based on typical wet or dry etching processes are unsuitable for mitigating TLS density in these devices due to the lack of Angstrom-scale precision in etching and the sub-surface damage they induce. To overcome these limitations, we develop a new chemistry for atomic layer etching of TiN in this chapter. Prior recipes to etch TiN make use of HF vapor, which is dangerous to work with and incompatible with commercial plasma tools capable of wafer-scale processing. The chapter details a recipe utilizing a much less-hazardous plasma in a commercial ALD tool. We develop and demonstrate such an ALE process for TiN using O_2 gas and an H_2/SF_6 plasma. We investigate the gas ratios for selective etching, saturation curves, temperature dependence, surface contamination, smoothing, effect on bulk chemistry, and cryogenic electrical transport properties.

In Chapter 3, we focus on the ALD and ALE of niobium nitride. Niobium nitride (NbN) is a material of interest for superconducting electronics due to its high superconducting critical temperature of up to 16 K and high kinetic inductance ($>$ 150 pH/□). These properties make it a promising material for single photon detectors such as kinetic inductance detectors, superconducting nanowire single photon detectors (SNSPDs), and hot electron bolometers. The high T_c of NbN film compared to other common superconductors such as Al and TiN (1.2 K and 5.5 K, respectively) also allows for higher operating temperatures, alleviating space,

weight, and power constraints of space missions. However, the figures of merit of these devices are negatively impacted by fabrication-induced damage. In addition to the same losses seen in TiN microresonators, the constriction factor of NbN SNSPDs is often limited by sidewall roughness caused by RIE-induced damage, which will in turn reduce the cutoff operational wavelength and limit internal efficiency near the long wavelength cutoff. ALE has the potential to alleviate these limitations. However, no ALE process had been reported for NbN, and this chapter outlines the development process for the first NbN ALE recipe reported in literature. The chapter details a recipe that takes inspiration from Chapter 2 by utilizing an H_2/SF_6 plasma in a commercial ALD tool. We develop and demonstrate an ALE process for NbN using O_2 plasma and an H_2/SF_6 plasma. The O_2 plasma is used to preferentially form the +5 oxidation state of Nb over the lower oxidation states, which then facilitates volatilization in the etch step. We investigate the gas ratios for selective etching, saturation curves, surface contamination, smoothing, effect on bulk chemistry, and cryogenic electrical transport properties.

In Chapter 4, we describe fabrication methods for superconducting-insulator-superconducting junctions for use as heterodyne mixers. We first report a new etching chemistry for a high T_c superconductor, MgB_2, using hydrogen plasma. We then examine the current-voltage characteristics of an MgB_2-Nb hybrid junction made using the new etching chemistry. Finally, we also detail the fabrication of all-ALD junctions and challenges encountered in their fabrication. MgB_2 has garnered significant interest due to its bulk T_c of 39 K. The bandwidth of SIS mixer detectors is proportional to the T_c of the superconductors used through its superconducting bandgap Δ. State-of-the-art detectors use NbTiN and Nb, which have a T_c of 13 and 9 K, respectively. While materials with higher T_c exist, there are challenges in achieving thin film deposition with sub-nm roughness, along with a limited ability to pattern such materials. Due to recent advancements in MgB_2 deposition allowing for < 0.5 nm surface roughness wafers, it has become a viable candidate for wafer-scale production of SIS mixers capable of THz radiation detection. We investigate the etch rate dependence on power and temperature, we measure the surface morphology and surface chemistry of MgB_2 films after etching, as well as the passivation effect of the hydrogen etching on MgB_2 films. We also examine the use of the hydride barrier for SIS junctions and the corresponding current-voltage characteristics.

Chapter 2

A NEW ATOMIC LAYER ETCHING RECIPE FOR TITANIUM NITRIDE

This chapter has been adapted from

Azmain A. Hossain, Haozhe Wang, David S. Catherall, Martin Leung, Harm Knoops, James R. Renzas, and Austin J. Minnich. "Isotropic plasma-thermal atomic layer etching of superconducting titanium nitride films using sequential exposures of molecular oxygen and SF_6/H_2 plasma." *Journal of Vacuum Science & Technology A*, 41(6), November 2023. DOI: 10.1116/6.0002965.

A.A.H. designed the research, conducted the experiments, analyzed the data, and wrote the manuscript.

2.1 Introduction

Titanium nitride (TiN) is a superconducting metal with a $T_c \sim 5.6$ K. TiN is of interest for microelectronics and superconducting quantum devices. Its high kinetic inductance, low microwave loss, and high absorption coefficient in the infrared and optical frequencies make it a promising material for single photon detectors [103, 181], ultra-sensitive current detectors [91], quantum-limited parametric amplifiers [72], and qubits [21, 67]. Superconducting microwave resonators based on TiN routinely exhibit internal quality factors $Q_i > 10^6$ [21, 167, 181]. TiN is also used for microelectronic applications in which it is used as a copper diffusion barrier and metal gate electrode [95, 110, 199]. In many of these applications, imperfections at film interfaces are the primary limitation to figures of merit for various devices. For instance, the quality factor of superconducting microresonators is presently thought to be limited by microwave surface loss associated with two-level systems (TLS) in various interfaces [11, 48, 49]. Subtractive nanofabrication methods based on typical wet or dry etching processes are unsuitable for mitigating TLS density in these devices due to the lack of Angstrom-scale precision in etching and the sub-surface damage they induce [2, 50, 161].

For TiN, ALE processes based on fluorination and ligand-exchange with $Sn(acac)_2$, trimethylaluminum (TMA), dimethylaluminum chloride (DMAC), and $SiCl_4$ did not

lead to etching [108]. When fluorinated, TiN retains its 3+ oxidation state, yielding TiF_3. TiF_3 either formed non-volatile ligand-exchange products or did not react with the precursors, and hence no etching occurred. This difficulty was overcome by first converting the Ti to the 4+ oxidation state with exposure to ozone or H_2O_2, which upon fluorination using HF produced volatile TiF_4 [106]. A conceptually similar process has also been reported using O_2 plasma and CF_4 plasma [171].

Despite these advances, limitations remain. The use of HF vapor incurs practical complications. The process of Ref. [171] based on O_2 plasma and CF_4 requires a heating and cooling step per cycle which can lead to impractical time per cycle on conventional plasma tools. Additionally, the recipe achieves nm/cycle etch rates, which lacks the desired Angstrom-scale control and low damage characteristics. Previous reports did not examine the effects of ALE on the superconducting properties of the samples. Identifying alternate reactants to HF vapor while maintaining Angstrom-level precision over the thickness, and ensuring that superconducting properties are not degraded, all remain topics of interest for TiN ALE.

Here, we report the isotropic atomic layer etching of TiN using sequential exposures of O_2 gas and SF_6/H_2 plasma. The process is based on the selective etching of TiO_2 over TiN for certain ratios of SF_6:H_2. The observed etch rates varied from 1.1 Å/cycle up to 3.2 Å/cycle for temperatures between 150 °C and 350 °C respectively, as measured using ex-situ ellipsometry. The etched surface was found to exhibit a $\sim$ 40% decrease in surface roughness. The superconducting transition temperature was unaffected by ALE beyond the expected change due to the decrease in film thickness, highlighting the low-damage nature of the process. Our findings indicate the potential of ALE in the processing of TiN for superconducting quantum electronics and microelectronics applications.

Methods

The plasma-thermal ALE process of this work is illustrated in Figure 2.1. An exposure of molecular oxygen was used to oxidize the surface of TiN to TiO_2, followed by a purge. Next, a mixture of SF_6 and H_2 gas was introduced into the chamber and ignited to form SF_6/H_2 plasma. After this exposure, the reactor was again purged to complete the cycle. The use of SF_6/H_2 plasma was motivated by noting that HF does not etch TiN, but fluorine radicals will spontaneously etch TiN [106, 149]. Studies on SiN and Si etching using hydrogen and fluorine-containing plasma have shown that the plasma formed by the mixture yields different products

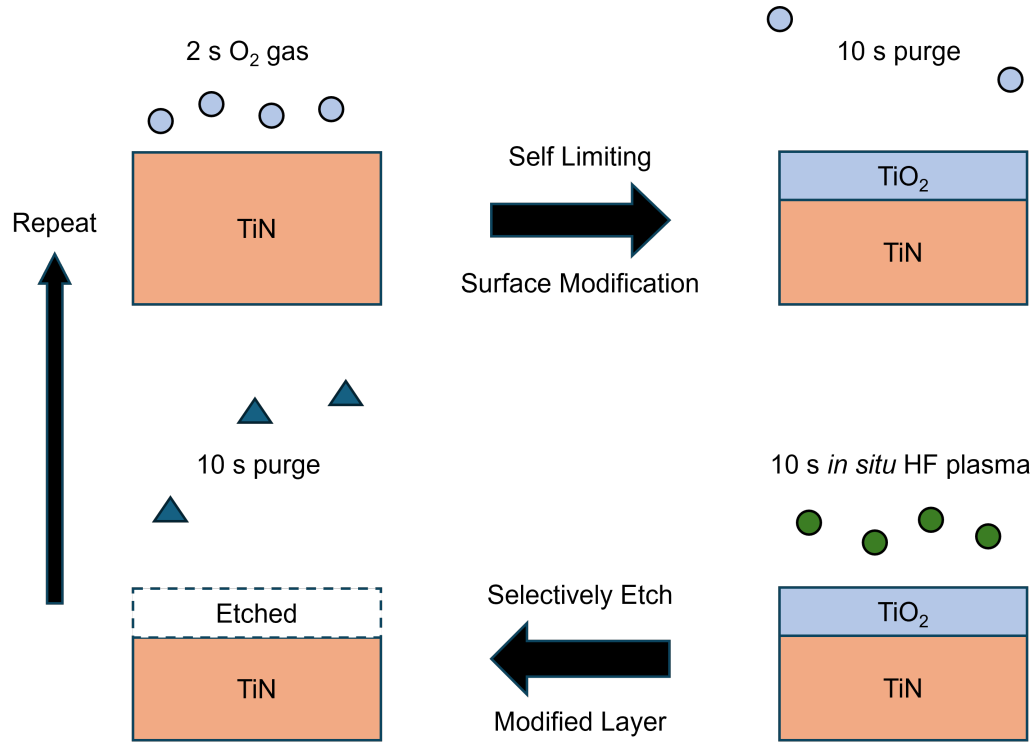

Figure 2.1: Schematic of the TiN ALE process involving exposures to molecular oxygen to oxidize the surface (O_2, blue dots), followed by SF_6/H_2 plasma (green dots) to produce volatile etch products.

at different plasma concentration ratios, including HF molecules at high hydrogen concentrations (H_2 to F-containing gas flow rate ratio $\gtrsim$ 2) [83, 147, 182]. We therefore expected to observe an effect similar to that reported in Refs. [83, 147, 182], in which fluorine radicals were found to combine with hydrogen radicals via multiple pathways to form vibrationally excited HF with negligible F radical concentration [182]. If this process did occur, the HF formed *in situ* could then react with the film and selectively etch TiO_2 over TiN, with minimal spontaneous etching from F radicals at sufficiently high H_2 concentrations. The etch selectivity of TiO_2 over TiN is due to the differing oxidation states of Ti in each compound, as previously observed in Ref. [106]. The formation of HF in the SF_6/H_2 plasma is referred to as "*in situ* HF plasma" throughout the paper. SF_6 gas was used in this work because of its successful use in previous work on the isotropic ALE of alumina and aluminum nitride [25, 185].

We investigated this approach to ALE of TiN using an Oxford Instruments FlexAL atomic layer deposition (ALD) system with an inductively-coupled plasma source, as described in Refs. [28, 179]. The substrate table temperature varied between

150 °C to 350 °C, as measured by the FlexAL substrate table thermometer. The minimum temperature in our study was restricted to 150 °C by the tool. The sample was placed on a silicon carrier wafer which sits on the substrate table, which may cause a difference between the true sample temperature and the table temperature. Prior to introducing the sample into the chamber for etching, the chamber walls and carrier wafer were conditioned by coating with 50 nm of Al_2O_3 using 300 cycles of Al_2O_3 ALD [179]. Alumina was selected as it does not form volatile fluoride species on exposure to SF_6 plasma.

For TiN ALE, the sample was first exposed to 50 sccm O_2 and 50 sccm Ar gas for 2 s at 100 mTorr pressure, followed by a 10 s purge. Next, a mixture of 20 sccm H_2 and 4 sccm SF_6 was stabilized at 100 mTorr for 5 s before striking the plasma at 100 W for 10 s. The excess reactants were purged for 10 s before repeating the cycle. The recipe resulted in a total time of $\sim$ 40 s per cycle. Before the sample was moved to the loadlock, the chamber was pumped down for 60 s. The sample was additionally held in the loadlock for one hour to cool down before exposure to air to reduce oxygen diffusion into the sample.

The film thickness before and after etching was measured by ex-situ spectroscopic ellipsometry (J.A. Woolam M2000) at 60° and 70° from 370 nm to 1000 nm. Thickness was determined using 5 points on a 5×5 mm^2 square array. Subsequently, the data were fit using a Lorentz model to obtain the thickness of the samples [102, 106]. The thickness and uncertainty values are the average and standard deviation of the 5 points, respectively. XPS analysis was performed using a Kratos Axis Ultra x-ray photoelectron spectrometer using a monochromatic Al Kα source. Depth profiling was performed using an Ar ion beam with a 60 s interval for each cycle. The estimated milling depth was calculated based on initial and final film thickness measured by ex-situ ellipsometry and assuming a constant ion milling rate. The XPS data was analyzed in CASA-XPS from Casa Software Ltd. We adopt universal Tougaard background and sub-peak fitting routines from Refs. [79, 115].

The film surface topography was characterized using a Bruker Dimension Icon atomic force microscope (AFM) over a 0.25×0.25 μm^2 area. The raw height maps collected on the AFM were processed by removing tilt via linear plane-fit. The surface roughness and power spectral density (PSD) were computed from the plane-fit height maps using procedures outlined in previous literature [54, 78]. The PSD provides a quantitative measure of the lateral distance over which the surface profile varies in terms of spatial frequencies [37, 78]. The PSD was calculated by taking

the absolute square of the normalized 1D-discrete Fourier transform of each row and column from the plane-fit AFM scan. The transformed data was then averaged to produce a single PSD curve. Reported roughness values were found to be vary by < 7% over 3 spots on each film.

Electrical resistivity measurements were performed on a Quantum Design DynaCool Physical Property Measurement System (PPMS). The TiN films were connected to the PPMS sample holder by four aluminum wires, wirebonded with a Westbond 7476D Wire Bonder. The film resistivity (ρ) was measured using a 4-point setup [167]. The resistivity was measured from 6 K to 1.7 K, and the data was used to calculate the superconducting critical temperature (T_c) of the films.

The samples consisted of 50 and 60 nm thick TiN films on high resistivity Si (100) wafers (> 20 kΩcm, UniversityWafer) prepared using ALD with the same FlexAL system. The development of the TiN ALD process is discussed in Section 2.2. The final recipe used to make films for the ALE study consisted of sequential half-cycles of exposure to tetrakis(dimethylamino)titanium (TDMAT) and nitrogen plasma with a 20 W DC bias at 350 °C, similar to the procedure reported in Refs. [41, 167]. The resistance at 6 K and T_c of a 60 nm thick ALD TiN film were measured to be 210 $\mu\Omega$cm and 3.22 ± 0.06 K, respectively; these values are comparable to those reported for other TiN films made using TDMAT [41, 135, 167]. The chemical composition of the deposited films are described in Section 2.3. The titania (TiO_2) films used for demonstrating etch selectivity in Section 2.3 were made by oxidizing TiN samples under an oxygen plasma for 5 minutes at 300 °C, yielding a 5 nm thick TiO_2 film on top of the TiN film. The thicknesses of the TiO_2 films were measured using ex-situ ellipsometry.

2.2 TiN ALD using TDMAT and H_2 plasma

ALD of TiN has been studied based on $TiCl_5$, tetrakis(dimethylamino)titanium (TDMAT), and a handful of other precursors [88]. The FlexAL in the KNI is fitted with TDMAT, so our study was limited to the TDMAT precursor. The first films were grown using the default recipe on the tool at 300 °C using a N_2/H_2 plasma. The 80 nm film grown had a resistivity of 480 $\mu\Omega$cm at 1 K with no superconducting transition down to 500 mK. Based on the works in Refs. [41, 167] a series of changes were made to the default KNI recipe to improve the TiN film quality.

The precursor dose step was fixed at 200 mTorr for 300 ms. The plasma step and temperature were changed in the following ways. The resistivity versus temperature

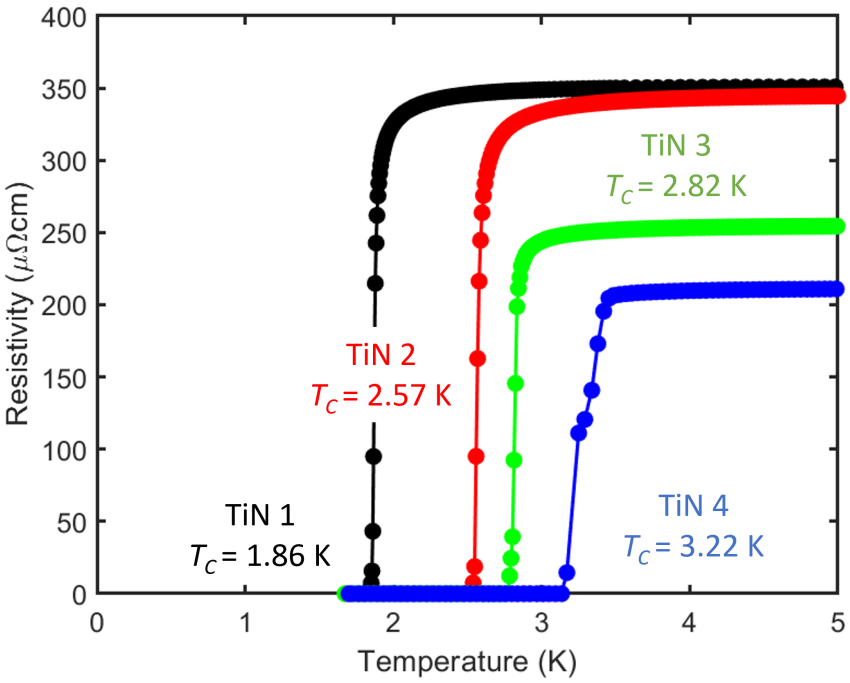

Figure 2.2: Resistivity versus temperature for four selected 60 nm TiN films. Each film shows an increase in T_c compared to the previous one. The dashed lines are guides to the eye.

curves of the improved 60 nm thick films are shown in Figure 2.2. TiN 1 (black) is the first superconducting TiN film made in this project, with a T_c of 1.86 K. This was achieved by changing the plasma chemistry from an N_2/H_2 gas mix to a pure N_2 gas plasma. This change was shown to improve the stoichiometry of the film closer to a 1:1 Ti:N ratio in prior work [41, 167]. From TiN 1 to TiN 2 (red), the plasma time was increased from 4 s to 8 s. The increase in plasma time pushes the ALD into the saturation zone and ensures full reaction with the precursor. Resulting in a T_c of 2.57 K for TiN 2. The resistivity at 5 K from TiN 1 to TiN 2 was roughly the same at $\sim$ 350 $\mu\Omega$cm. From TiN 2 to TiN 3 (green) the temperature was increased from 300 °C to 350 °C, and plasma power was increased from 300 W to 500 W. The higher temperature had been shown to improve film crystallinity and reduce film resistivity, while the higher power was shown to reduce the carbon contamination in the film. Film 3 had a T_c of 2.82 K and a resistivity of $\sim$ 250 $\mu\Omega$cm at 5 K. The final improvement was the introduction of a 20 W DC bias in the plasma step leading to the TiN 4 (blue) curve, with a T_c of 3.22 K and a resistivity of 210 $\mu\Omega$cm at 5 K. The use of a bias in the plasma step had been shown to increase the size and density of crystal grains, leading to improved T_c. Work on TiN ALD stopped here as the resistivity and T_c was comparable to other works [41, 135, 167], and the films were

a good example of TiN films for testing ALE recipes on.

The final recipe was 500 ms TDMAT at 40 mTorr with 100 sccm Ar, followed by a 3 s purge with 200 sccm Ar. The plasma half-step consisted of 10 s of 80 sccm N_2 at 20 mTorr with plasma parameters of 500 W ICP and 20 W DC bias. The cycle was completed with a 2 s purge of 200 sccm Ar. The recipe resulted in a growth rate of 0.86 Å/cycle. Additional improvements were made to the ALD process in Ref. [42], achieving a T_c of 4.2 K. The use of a lower plasma pressure and breaking the plasma step into a two-step plasma exposure was shown to reduce the oxygen contamination observed in the TiN films in this thesis.

2.3 TiN ALE using O_2 gas and in-situ HF plasma

Selective etching with SF_6/H_2 Plasma

We begin by examining the etch rate of TiO_2 and TiN films for various SF_6:H_2 flow rate ratios, η. Figure 2.3a shows the etch rates of TiN and TiO_2 versus η at 300 °C. For $\eta \lesssim 0.05$, negligible etching of either film is observed. At $\eta = 0$ we measure an etch rate of −0.03 Å/cycle. This value is within the measurement error of the ellipsometer, and as such we do not attribute physical significance to the negative value. The other negative etch rates correspond to an increase in the thickness of the film, which we assume to be growth of non-volatile TiF_3. For $\eta \geq 0.1$, we observe spontaneous etching of TiO_2, with the etch rate monotonically increasing with η. For TiN, we observe no etching for $\eta \leq 0.2$, but for $\eta \geq 0.25$ etching occurs. We attribute these observations to the formation of *in situ* HF along with negligible fluorine radical concentration for $0.05 < \eta \leq 0.2$. For $\eta \geq 0.25$, the concentration of F radicals becomes sufficient to spontaneously etch the TiN, leading to increasing etch rates for both films. From our measurements, we find that $0.1 \leq \eta \leq 0.2$ achieves selective etching of TiO_2 over TiN. To obtain the highest etch selectivity of TiO_2 over TiN, we select $\eta = 0.2$ for our experiments. This 1:5 ratio of SF_6:H_2 plasma is used throughout the rest of the paper.

TiN ALE using O_2 and in-situ HF plasma exposures

Figure 2.3b shows the thickness change of TiN versus number of cycles for both half cycles, and for the full ALE recipe at 200 °C and 300 °C. For the half-cycles, the thickness change was measured after exposure to only molecular oxygen or *in situ* HF plasma. No etching was observed for either half-cycle. In contrast, we observe a decrease in the thickness with increasing number of cycles when using both steps. The etch rate is calculated by dividing the total thickness change by the number of

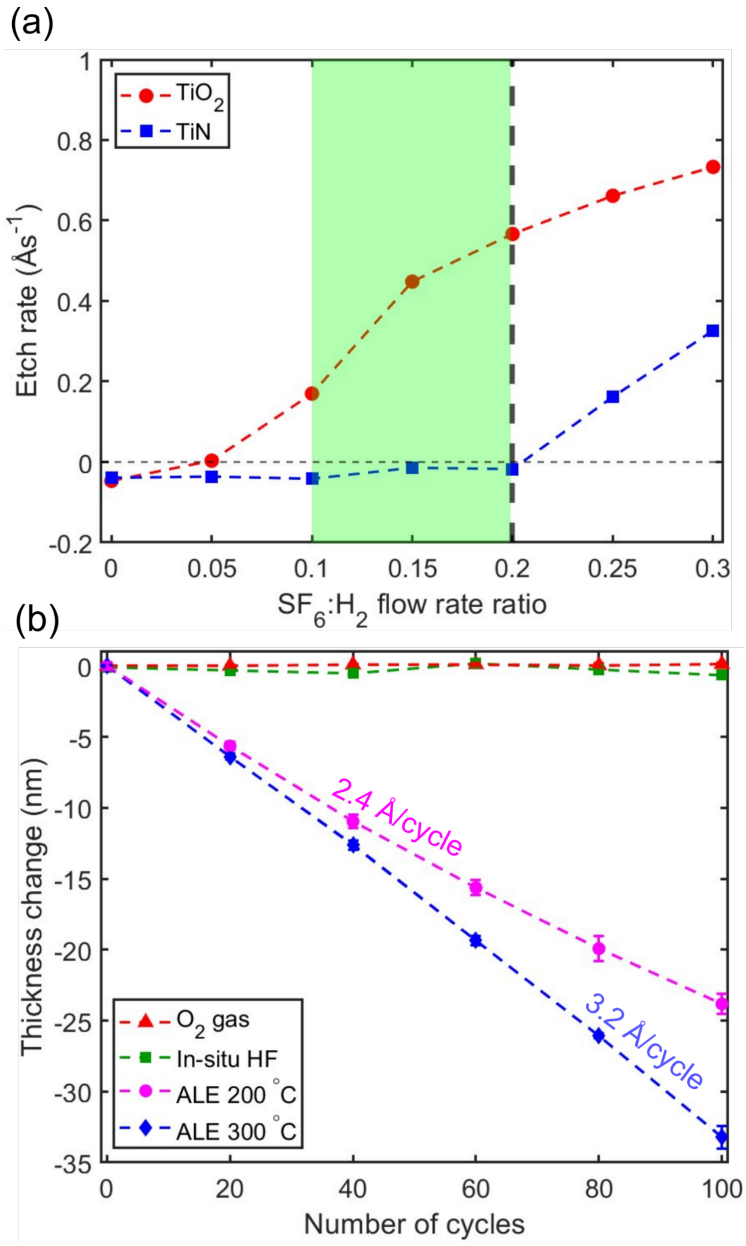

Figure 2.3: (a) Etch rate of TiO_2 and TiN versus the SF_6:H_2 flow rate ratio. The green shaded area represents the flow rate ratios for which selective etching of TiO_2 over TiN was achieved. The black line at a ratio of 0.2 represents the ratio used in the ALE experiments. (b) TiN thickness change versus number of cycles with exposure only to O_2 gas (red triangles), *in situ* HF plasma (green squares), full ALE process at 200 °C (purple circles) and 300 °C (blue diamonds). The dashed lines are guides to the eye.

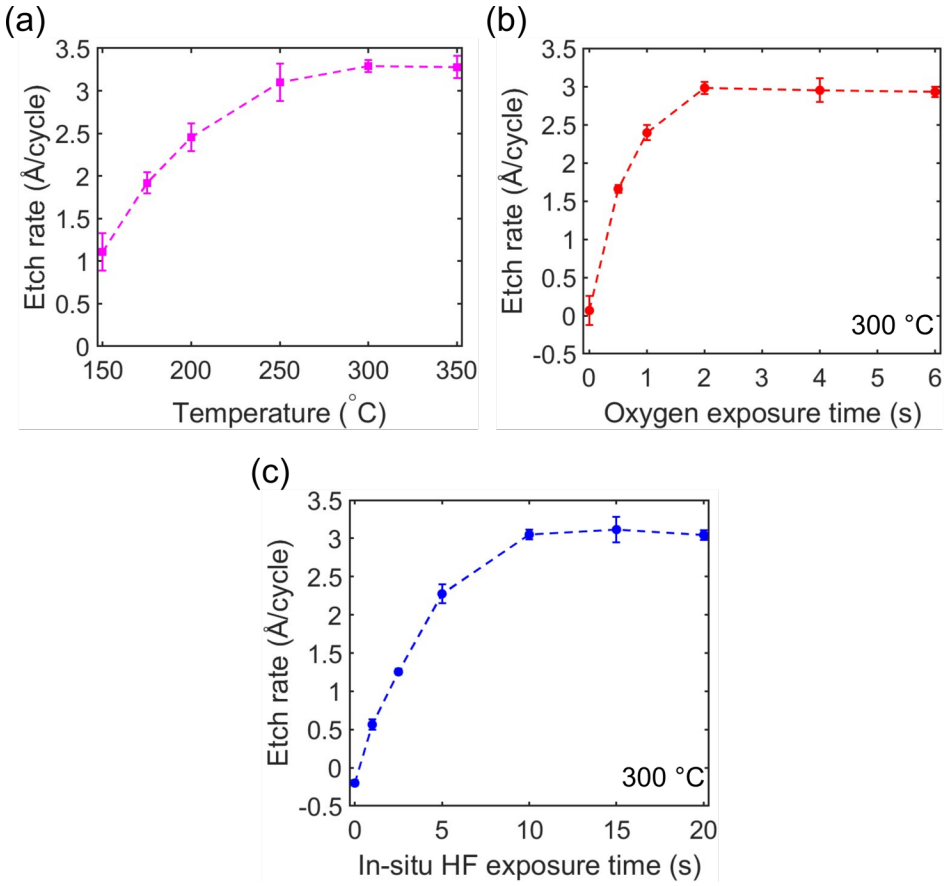

Figure 2.4: (a) TiN ALE etch per cycle (EPC) versus substrate table temperature. (b) EPC versus O_2 gas exposure time with *in situ* HF plasma exposure time fixed at 10 s at 300 °C. (c) EPC versus *in situ* HF plasma time with O_2 exposure time fixed at 2 s at 300 °C. The etch rates are observed to saturate with exposure time, demonstrating the self-limiting nature of the ALE process. The dashed lines are guides to the eye.

cycles, giving values of 2.4 ± 0.16 Å/cycle at 200 °C and 3.2 ± 0.10 Å/cycle at 300 °C.

We further examine the effect of temperature on the etch rate. Figure 2.4a shows the etch per cycle (EPC) versus table temperature ranging from 150 °C and 350 °C. The etch rates are calculated from the thickness change over a 100 cycles. We find that the etch rate increases from 1.1 Å/cycle at 150 °C to 3.2 Å/cycle at 300 °C. In analogy to other works [52, 106, 171], we attribute the etch rate increase with temperature to the higher diffusion rates at higher temperatures in the oxidation step, leading to thicker oxides which are etched at each step. We also observe a constant etch rate from 300 °C to 350 °C, similar to what is reported in Figure 7 of Ref. [106].

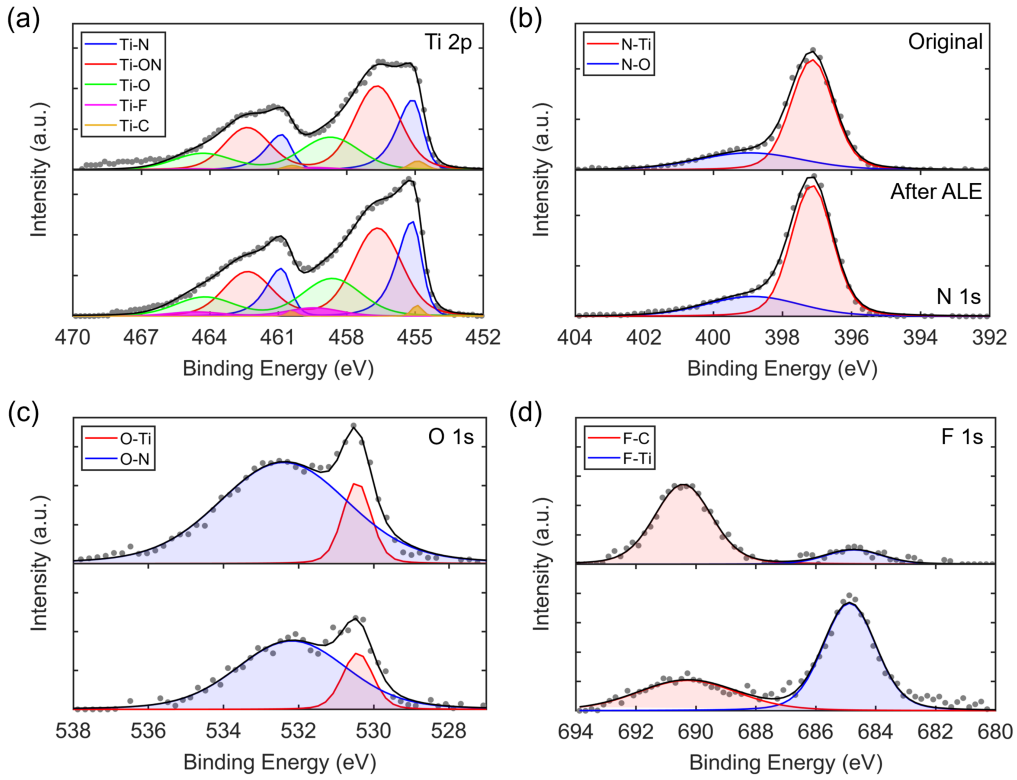

Figure 2.5: Surface XPS spectra showing (a) Ti2p, (b) N1s, (c) O1s and (d) F1s spectra. The spectra is shown for (top) original and (bottom) etched TiN films. The measured (gray dots) and fit spectra (black lines) intensity are reported in arbitrary units (a.u.) against the binding energy on the x-axis. The y-axis scale is identical between panels within each subfigure.

We also explored the self-limiting nature of the process by measuring the saturation curves of each half-cycle. For each saturation curve the temperature is set to 300 °C, and the purge times and one half-cycle time are fixed while the other is varied. In Figure 2.4b, the *in situ* HF plasma step is fixed at 10 s, while the etch rate is measured versus the oxygen exposure time. The etch rate is observed to saturate to ~ 3 Å/cycle above 2 s, which is consistent with the self-limiting nature of the oxidation step. In Figure 2.4c, the oxidation step is fixed at 2 s, while the etch rate is measured versus *in situ* HF plasma exposure time. The etch rate saturates to ~ 3 Å/cycle above 10 s, which is consistent with the selectivity of the *in situ* HF to etch TiO_2 and terminate on the TiN.

Characterization of film composition

We next characterize the chemical composition of the TiN films before and after ALE using XPS. In Figure 2.5, we show the core levels of Ti2p, N1s, O1s, C1s and F1s. For the Ti2p XPS spectra in Figure 2.5a, we observe five components. Each component is a doublet consisting of a $2p_{3/2}$ and a $2p_{1/2}$ subpeak. We observe subpeaks corresponding to Ti-C (454.9 eV and 460.4 eV) [114, 136, 163], Ti-N (455.1 eV and 460.8 eV) [20, 101, 159], Ti-ON (456.5 eV and 462.3 eV) [20, 101, 159], Ti-O (458.5 eV and 464.2 eV) [20, 101, 159], and Ti-F (459.4 eV and 465.6 eV) [134, 139]. In Figure 2.5b, we report the N1s spectra with two subpeaks at 397.1 eV and 398.9 eV, belonging to N-Ti and N-O bonds, respectively [20, 101, 159]. In Figure 2.5c, we report the O1s spectra with two subpeaks at 530.4 eV and 532.2 eV, corresponding to O-Ti and O-N bonds, respectively [20, 101, 159]. In Figure 2.5d, we report the F1s spectra with two subpeaks at 684.9 eV and 690.3 eV, corresponding to F-Ti and F-C bonds, respectively [13, 134, 139].

We observe that the Ti2p spectra is dominated by oxides and oxynitrides, consistent with the presence of a native oxide on TiN [135, 159]. After ALE (bottom panels of Figures 2.5a to 2.5c), an increase in the magnitude of the Ti-N and N-Ti peaks is observed along with an overall decrease in the O1s peak magnitude. The decreased O1s signal implies a reduced native oxide concentration after ALE, as has been observed in ALE of other materials [68, 128, 185]. The F1s spectra for the original sample may be attributed to contamination from using the same chamber for deposition and etching, which is consistent with the reduced magnitude of the F1s peak in the original sample compared to that in the ALE-treated sample (bottom panel of Figure 2.5d).

We also performed depth-profiling XPS to determine the atomic concentrations on the surface and in the bulk. In Figure 2.6, we show the atomic concentrations of Ti, N, F, C, and O versus sputtering time and estimated depth in the original and ALE-treated films. In the original sample (Figure 2.6a), the atomic concentrations on the surface are 31.9% (Ti), 37.6% (N), 16.1% (O), 12.0% (C), and 2.4% (F). After 120 s Ar milling ($\sim$ 3.5 nm), the atomic concentrations plateau to their bulk values of 48.6% (Ti), 42.3% (N), 6.1% (O), 1.9% (C), and 1.1% (F). The carbon and oxygen levels are consistent with other reported ALD TiN films made using TDMAT [36, 43, 135]. The carbon signal on the surface is observed to be predominantly C-O and C-H bonds, expected from adventitious carbon which occurs on exposure to atmosphere. The carbon signal in the bulk is from C-Ti bonds, which has been

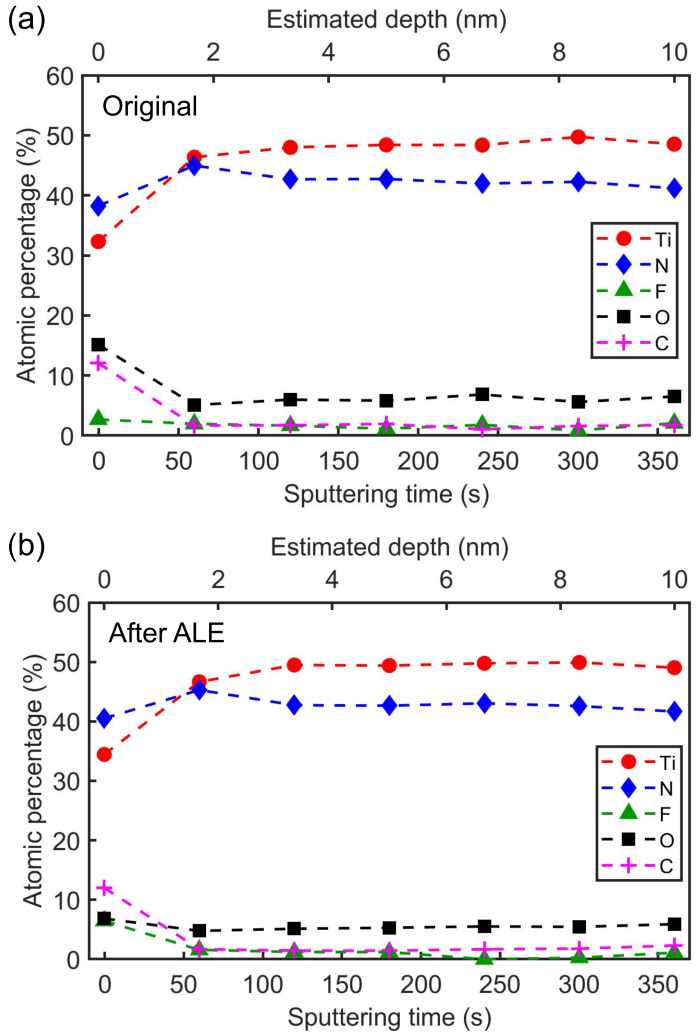

Figure 2.6: Atomic concentrations of Ti, N, O, F, and C versus Ar milling time and estimated depth, for (a) original and (b) ALE-treated TiN thin film. The dashed lines are guides to the eye.

attributed to the decomposition of TDMAT during ALD in prior studies [135]. The carbon and oxygen contamination in the bulk is known to cause higher resistivities and lower T_c compared to films with lower contamination concentrations [135, 153]. For the ALE-treated sample (Figure 2.6b), the atomic concentrations on the surface are 34.2% (Ti), 39.5% (N), 7.9% (O), 11.9% (C), and 6.5% (F). After 120 s Ar milling ($\sim$ 3.5 nm), the atomic concentrations plateau to their bulk values of 49.0% (Ti), 42.2% (N), 5.9% (O), 1.8% (C), and 1.1% (F). We observe a $\sim$ 49% decrease in the surface oxygen concentration in the ALE-treated film. An increase in the surface fluorine concentration of the ALE-treated film is also observed, consistent with other works involving the interactions of fluorine-containing plasma with dielectric films [44, 68, 185]. The atomic concentrations in the bulk of the ALE-treated film are

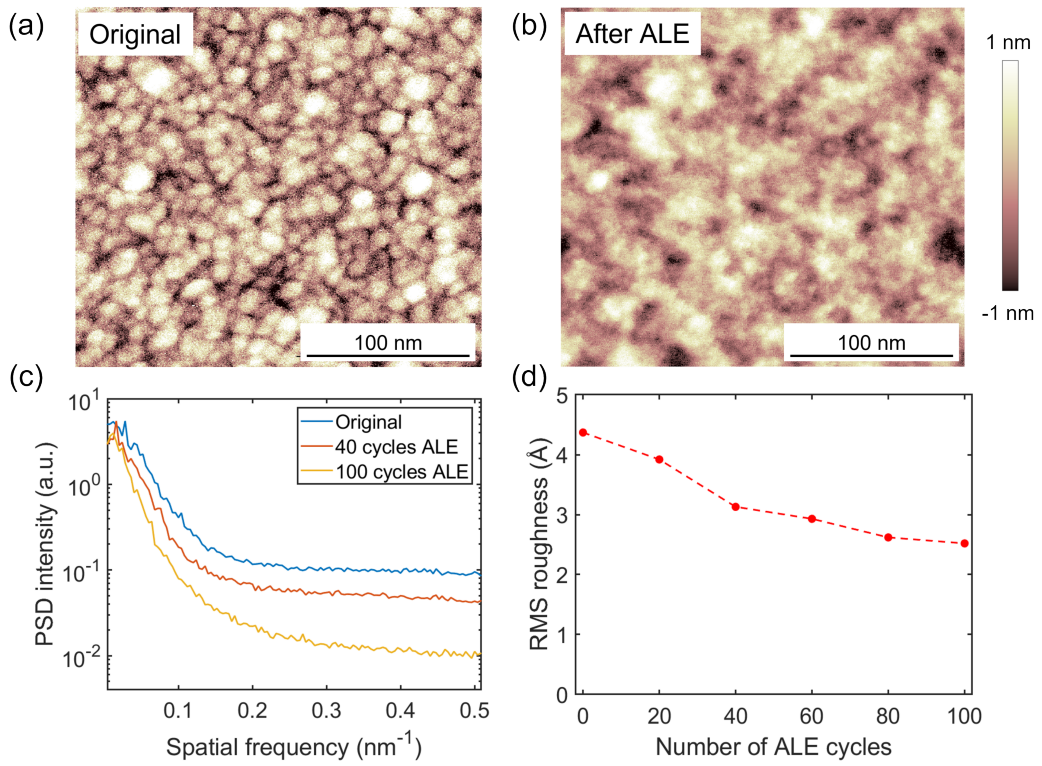

Figure 2.7: AFM scan showing height-maps of original ALD sample (a) and after 100 ALE cycles (b). (c) Progression of the height-map PSD with increasing ALE cycles, showing decrease across all spatial frequencies. (d) RMS roughness computed from AFM height-map against number of ALE cycles. The dashed line is a guide to the eye.

within 95% of the values in the original film. Therefore, we conclude that the effect of ALE is confined to a few nanometers of the surface, with negligible effect on the bulk chemical composition.

Surface roughness characterization

We characterized the roughness of the TiN films before and after ALE using AFM. Figure 2.7a shows the plane-fit height map of the film as deposited using ALD. Figure 2.7b shows the plane-fit height map after 100 cycles of ALE at 300 °C. Figure 2.7c shows the PSD curves for the original film, after 40 ALE cycles and after 100 ALE cycles at 300 °C. We observe a decrease in the PSD intensity across all length scales as the number of ALE cycles is increased, indicating that features with length scales from $\sim 2 - 20$ nm are smoothed by the ALE process. In Figure 2.7d, the RMS roughness is plotted versus the number of ALE cycles at 300 °C. We observe a monotonic decrease in RMS roughness from 4.4 Å to 2.5 Å after 100

cycles. This 43% reduction in roughness was observed across 3 different positions on the sample.

Electrical and superconducting properties

We investigated the effect of ALE on the electrical and superconducting properties of the TiN films by measuring their resistivity from 6 K to 1.7 K. A 60 nm TiN film was deposited using ALD, which was etched to 50 nm using ALE. Another 50 nm TiN film was prepared using ALD to compare to the ALE-treated 50 nm film. The measured resistivity versus temperature for the three films is shown in Figure 2.8. The resistivity at 6 K of the 60 nm ALD film is found to be 222 $\mu\Omega$cm, with a superconducting critical temperature $T_c = 3.22 \pm 0.06$ K. The resistivity of the TiN film is consistent with those previously reported for ALD TiN films [135, 167], and the T_c reported is similar to the T_c of other TiN films grown with TDMAT [153, 167]. After 40 cycles of ALE at 200 °C, the TiN thickness decreased to 50 nm, with a resistivity of 201 $\mu\Omega$cm at 6 K and $T_c = 3.13 \pm 0.04$ K. For comparison, the 50 nm ALD film had a resistivity of 227 $\mu\Omega$cm at 6 K, and $T_c = 3.11 \pm 0.05$ K. We therefore find that the change in T_c of the TiN film after ALE is consistent with that expected with a decrease of 10 nm in thickness, without any additional decrease due to process-induced damage. This observation highlights the improved quality of the processed films compared to those obtained from processing methods which lack atomic control. For example, nitrogen plasma treatment of Nb films resulted in a T_c decrease of $\sim 9\%$ [200]. The reduced 6 K resistivity of the ALE-treated film is thought to arise due to the removal of the native oxide. To test this hypothesis, the ALE-treated film's electrical properties were measured after two months in ambient atmosphere. The resistivity at 6 K and T_c were measured as 214 $\mu\Omega$ cm and 3.09 ± 0.02 K, respectively. The T_c change is within the uncertainty of the initial ALE-treated film's T_c of 3.13 ± 0.04 K. The aged resistivity increased from 201$\mu\Omega$cm, as expected due to re-oxidation of the film after ALE with exposure to atmosphere. However, the resistivity did not increase to the value of the 50 nm ALD film (227 $\mu\Omega$cm). We hypothesize that the lower resistivity of the ALE-treated sample is due to the fluorinated surface serving as a diffusion barrier for oxygen, similar to the effect observed in Ref. [68]. These results warrant further investigation and is a topic of future study.

We now discuss the characteristics of our plasma-thermal TiN ALE process in context with isotropic thermal ALE processes for TiN and related materials. Thermal ALE of TiN has been reported using molecular O_3 or H_2O_2 and HF vapor [106], and

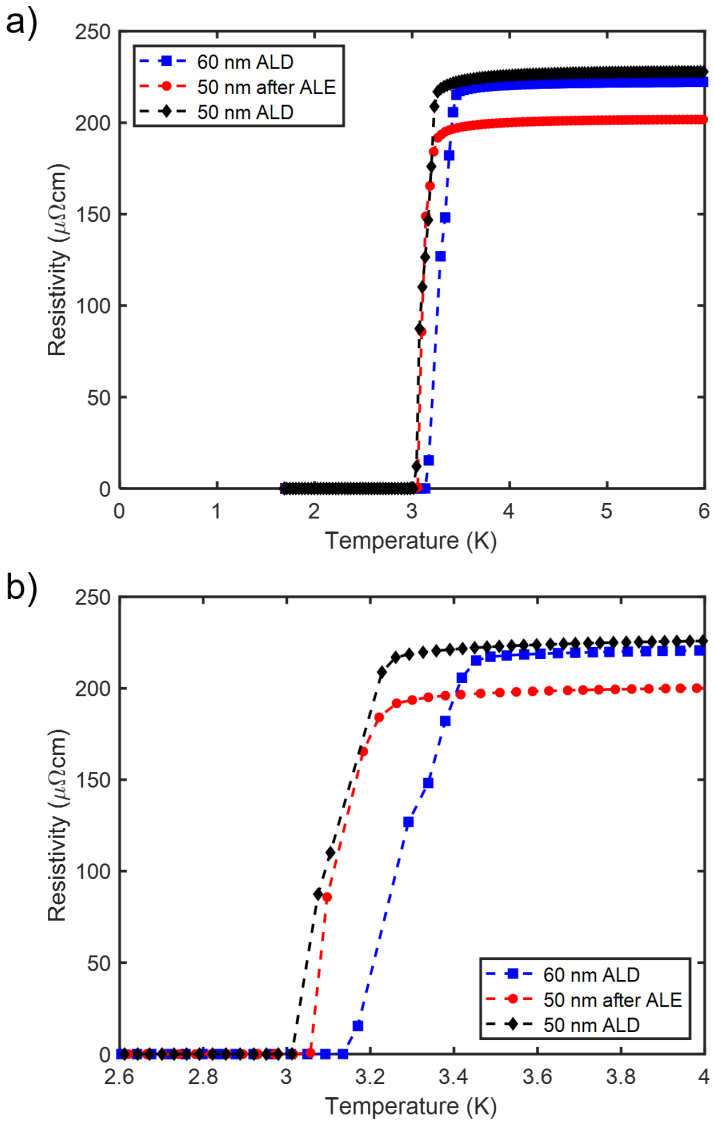

Figure 2.8: a) Resistivity versus temperature for original 60 nm TiN film (blue), ALE-treated film of 50 nm thickness (red) and a 50 nm ALD TiN film (black) for comparison. The difference in T_c between the 50 nm ALD film and ALE-treated 50 nm film is negligible. b) Resistivity versus temperature plot with a truncated x-axis to highlight the superconducting transitions. Zoomed The dashed lines are guides to the eye.

O_2 plasma and CF_4 plasma [171]. The first process leads to an etch per cycle (EPC) of 0.20 Å/cycle at 200 °C, achieving atomic-scale control of etching. However, the recipe requires the use of HF vapor which incurs practical complications. The second process based on O_2 plasma and CF_4 plasma achieves an EPC of 17.1 Å/cycle at 200 °C, which is a larger EPC than is desired for manipulating the surface region of the films. The second process also requires an additional heating step, which can lead to impractical process times on conventional tools. The present recipe achieves an EPC of 2.4 Å/cycle at 200 °C, providing etch rates between the previous reported recipes. The present recipe also avoids the use of HF, requiring only an SF_6/H_2 plasma that also yields etching selectivity of TiO_2 over TiN.

Our isotropic plasma-thermal ALE may find potential applications in the fabrication of TiN-based superconducting microresonators for microwave kinetic inductance detectors and qubits, where the native oxide hosts parasitic TLS that presently limit the device performance. Based on our XPS and resistivity measurements, ALE-treated films have a reduced oxygen concentration while maintaining unaltered bulk chemistry and electrical properties. These properties make ALE promising for reducing the number of TLS in the metal-air interface and thereby improving the quality factor of superconducting microresonators. While isotropic etching is less suitable for pattern transfer compared to anisotropic etching, isotropic ALE may find application as a post-treatment process by removing the few-nanometer-thick surface region hosting TLS after the primary etch process. The smoothing effect and isotropic Angstrom-scale EPC of the present ALE recipe is also relevant for fabricating TiN-based nanoscale metal gate electrodes in CMOS devices and various transistor designs, where the metal layers are required to have thickness on the order of $\sim$ 10 nm with uniformity $\lesssim$ 4% [121, 199]. The ALD system in our work (Oxford Instruments, FlexAL) has demonstrated high uniformity on 200 mm diameter substrates [179], and therefore our process has the potential to extend to wafer-scale applications.

2.4 Conclusion

We have reported an plasma-enhanced atomic layer deposition and an isotropic plasma-thermal atomic layer etching process for TiN. TiN ALD was performed using TDMAT and H_2 plasma achieving growth rates of $\sim$ 0.86 Å/cycle, consistent with work reported in [41, 135]. Multiple optimizations were required to arrive at the reported ALD recipe, such as plasma power control, plasma time and the inclusion of a DC bias during plasma exposure. Our final films had a T_c of 3.22 K

and resistivity of 222 $\mu\Omega$cm at 6 K. The deposited films also had an RMS surface roughness of $\sim$ 0.42 nm.

ALE was achieved using sequential exposures of molecular oxygen and SF_6/H_2 plasma. The SF_6/H_2 plasma selectively etched TiO_2 over TiN for SF_6:H_2 flow rate ratios between 0.1 and 0.2. The etch rate varied from 1.1 Å/cycle at 150 °C to 3.2 Å/cycle at 350 °C. We observed a smoothing effect from ALE, corresponding to a $\sim$ 43% reduction in RMS roughness after 100 cycles. The surface oxygen concentration was reduced by $\sim$ 49% after 100 cycles of ALE, indicating a decrease in the volume of surface oxide. We also found that ALE does not induce any change in T_c beyond that expected from the decrease in film thickness, highlighting the low-damage nature of the process.

We anticipate that the ability to engineer the surface of TiN films on the Angstrom-scale using ALE and ALD will facilitate applications of TiN in superconducting resonators and microelectronics.

Chapter 3

THE FIRST ATOMIC LAYER ETCHING RECIPE FOR NIOBIUM NITRIDE

This chapter has been adapted from:

Azmain A Hossain, Sela Murphy, David S Catherall, Anthony J Ardizzi, and Austin J Minnich. "Atomic layer etching of niobium nitride using sequential exposures of O2 and H2/SF6 plasmas". Journal of Vacuum Science & Technology A, 43(4), July 2025. DOI: 10.1116/6.0004548.

A.A.H. designed the research, conducted the experiments, analyzed the data, and wrote the manuscript.

3.1 Introduction

Niobium nitride (NbN) is a material of interest for superconducting electronics due to its high superconducting critical temperature T_c (up to 16 K) [172], kinetic inductance (> 150 pH/□) [4, 47], and high absorption coefficient in the infrared and optical wavelengths [3, 180]. These properties make it promising for devices such as kinetic inductance detectors (KIDs) [7], superconducting nanowire single-photon detectors (SNSPDs) [59], qubits [96], hot electron bolometers (HEBs) [99], and other superconducting quantum devices [4, 5, 76]. The high T_c of NbN film compared to other common superconductors such as Al and TiN (1.2 K and 5.5 K, respectively) also allows for higher operating temperatures which alleviates space, weight, and power constraints of space missions [12, 123].

State-of-the-art NbN devices are typically fabricated using reactive ion etching (RIE) with fluorine-containing plasmas [39, 64]. RIE fabricated devices such as superconducting microwave resonators based on NbN have been reported with single-photon internal quality factors $Q_i > 10^5$ [17, 47]. NbN SNSPDs have been demonstrated with > 95% system efficiency and timing jitter < 70 ps [196, 197]. However, the figures of merit of these devices are negatively impacted by fabrication-induced damage. For example, the quality factor of superconducting microresonators is presently thought to be limited by cryogenic microwave surface loss associated with two-level systems (TLS) or other mechanisms at various interfaces [11, 49]. In addition, the constriction factor of SNSPDs is often limited by sidewall roughness

caused in part by RIE-induced damage, which will in turn reduce the cutoff operational wavelength and limit internal efficiency near the long wavelength cutoff [27, 46, 87].

Typical dry etching processes for pattern transfer employ plasmas with energetic ions, making sample damage difficult to avoid for non-negligible etch rates. Atomic layer etching (ALE) is an emerging nanofabrication process with potential to overcome these limitations [84, 86, 109, 143]. Although several ALE processes have been reported for materials relevant to the semiconductor industry [84, 143], fewer studies have focused on materials relevant to quantum devices [22, 74]. No ALE process for NbN had been reported until this work. Several ALE processes have been demonstrated for a related material, TiN, based on leveraging the volatility of higher oxidation state fluorides compared to lower oxidation state fluorides [74, 106]. However, due to the complexity of the oxidation chemistry of Nb, whether these approaches were applicable to NbN was unclear.

Here, we report a plasma-thermal ALE process for NbN using sequential exposures of O_2 plasma and H_2/SF_6 plasma. The O_2 plasma is used to preferentially form the +5 oxidation state of Nb over the lower oxidation states, which then facilitates volatilization as NbF_5 by exposure to a H_2/SF_6 plasma mixture. The etch rate is measured to be 1.77 Å/cycle at 125 °C using *ex situ* ellipsometry. The etched surface was found to exhibit a 55% decrease in surface roughness and a 59% decrease in surface oxygen concentration over 50 cycles. The superconducting transition temperature of the ALE-etched sample is higher than that of an RIE-etched film of a similar thickness, indicating that ALE induces less damage in the film. Our findings suggest that our NbN ALE process could be used to mitigate surface loss and hence improve the performance of NbN superconducting electronics.

Methods

ALE processes were performed in an Oxford Instruments FlexAL II atomic layer deposition (ALD) system. In this reactor, the substrate is placed below an inductively coupled plasma source with direct line of sight to the plasma [179]. The temperature of the substrate table was maintained at 125 °C as measured by the substrate table thermometer. As the lowest possible process temperatures are generally desired to maintain film quality, we did not consider temperatures higher than 125 °C, the minimum temperature in the reactor. Before loading the sample into the chamber, preconditioning was performed to keep the chamber conditions as consistent as

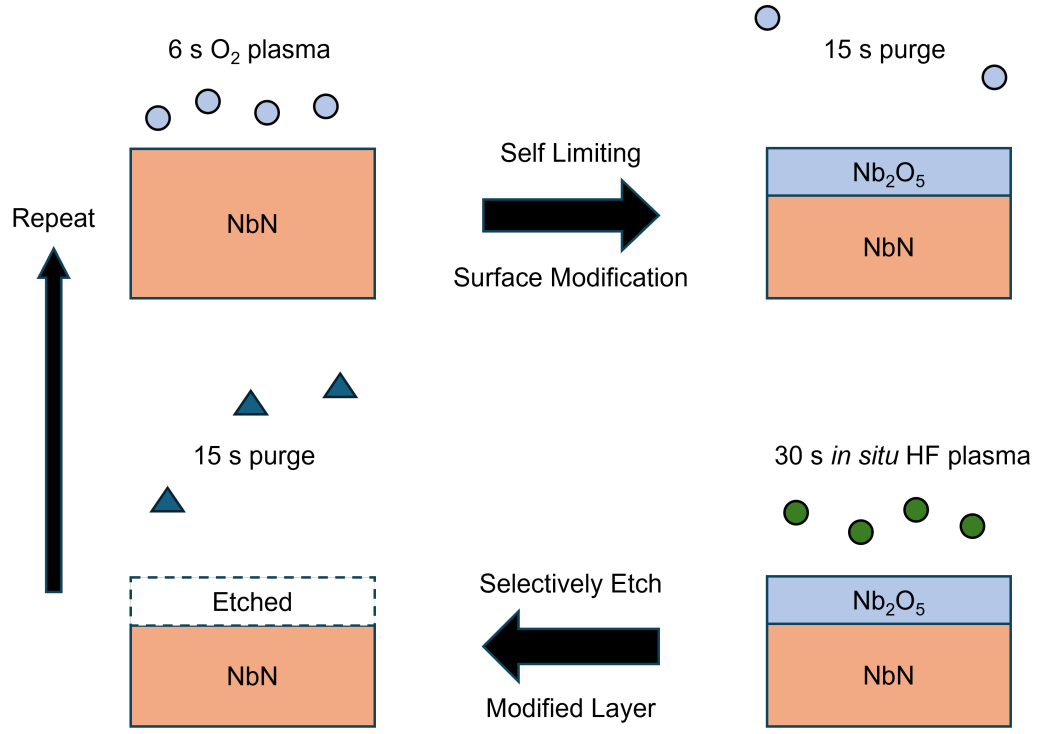

Figure 3.1: Schematic of the NbN ALE process. The surface is first modified by exposure to O_2 plasma (orange dots) to oxidize NbN to its +5 oxide of Nb_2O_5. Nb_2O_5 is then exposed to an H_2/SF_6 plasma (green dots) to produce volatile etch products.

possible between different runs on the shared tool. The preconditioning consisted of 10 minutes of an SF_6/O_2 plasma to clean the chamber of contaminants with volatile fluoride species, followed by 300 cycles (~ 50 nm) of alumina ALD [179], and another 5 minutes of SF_6/O_2 plasma to react with the remaining precursor. Alumina was used as it forms a stable AlF_3 layer when exposed to SF_6 plasma.

The plasma-thermal ALE process of this work is illustrated in Figure 3.1. Each ALE cycle starts with a 6 s exposure of the oxygen plasma with 50 sccm O_2 to oxidize the surface of NbN to Nb_2O_5. This step is followed by a 15 s purge using Ar with a flow rate of 400 sccm. Then, H_2 and SF_6 gas are flowed at a fixed flow rate ratio before striking a plasma and exposing for 30 s. After another 15 s purge of 400 sccm Ar, the cycle is complete. For each plasma step, the chamber pressure is held at 100 mTorr and the plasma is struck at 400 W. After ALE processing, the chamber is pumped down for 60 s before unloading the sample. The overall process has a cycle time of ~ 68 s/cycle.

The etched amounts were calculated based on thickness measurements of a 10×10

mm^2 chip before and after processing using *ex situ* ellipsometry on a J.A. Woolam M2000 ellipsometer. The film thickness was determined by scanning 9 points at 60° and 70° from 370 – 1000 nm. NbN optical data were obtained from Ref. [125]. The data was fit to an NbN/SiO_2/Si film stack to determine the thickness at each point. The thickness and uncertainty reported are the average and standard deviation of the 9 ellipsometry data points, respectively.

The film surface topography was characterized using a Bruker Dimension Icon atomic force microscope (AFM) over a 250×250 nm^2 area using PeakForce Tapping mode. The raw height maps collected on the AFM were processed by removing tilt using the Bruker Analysis linear flatten function. Surface roughness and power spectral density (PSD) were calculated from plane-fit height maps using procedures outlined in the previous literature [19, 54, 74]. The PSD provides a quantitative measure of the lateral distance over which the surface profile varies in terms of spatial frequencies [78].

Film composition was characterized using X-ray photoelectron spectroscopy (XPS) performed on a Kratos Axis Ultra X-ray photoelectron spectrometer using a monochromatic Al Kα source. Depth profiling was performed using an Ar ion beam with a 25 s interval for each cycle. The estimated milling depth was calculated based on initial and final film thickness measured by *ex situ* ellipsometry and assuming a constant ion milling rate. The XPS data was analyzed in CASA-XPS from Casa Software Ltd using bond binding energies and fitting procedures outlined in prior literature [31, 82, 112, 191].

Cryogenic electrical measurements were performed on a Quantum Design DynaCool Physical Property Measurement System (PPMS). The NbN films were connected to the PPMS sample holder by four aluminum wires, wirebonded with a Westbond 7476D Wire Bonder. Film resistivity (ρ) was measured using a 4-point probe setup. The resistivity was measured from 5 K to 20 K, from which the superconducting critical temperature (T_c) of the films was computed. The T_c reported is defined as the temperature value at which resistivity drops to half of the 20 K resistivity value, and the uncertainty reported is half the width of the superconducting transition temperature range (ΔT_c).

NbN films on a Si wafer were provided by the Jet Propulsion Laboratory. The films were deposited by reactive sputtering at room temperature on a high resistivity 500 µm Si (100) wafer with a 240 nm thermally grown SiO_2 buffer layer. The initial thickness was 30 ± 1 nm. The process followed those developed for NbN SNSPDs

[30, 175]. Individual sample chips were obtained by dicing the 4 inch wafer into 10×10 mm^2 squares.

The resistivity at 20 K and T_c of the films was measured as 291 $\mu\Omega$cm and 11.22 $\pm$ 0.14 K, respectively. The T_c of our samples is within 10% of those of sputtered NbN films on Si reported in literature [175, 197]. Several sets of films were prepared for various portions of the study. To develop the ALE process, two samples were oxidized with either O_2 gas (120 s at 100 mTorr) or O_2 plasma (120 s at 100 mTorr and 400 W) at 125 °C. Both samples were etched with SF_6 plasma at 125 °C (15 s at 100 mTorr and 400 W) prior to oxidation. The pre-processing removed the NbN native oxide and also etched $\sim$ 3 nm of NbN to emulate oxidation in the middle of an ALE process.

To test etch selectivity, niobium oxide films were prepared. NbN samples were exposed to an O_2 plasma (120 s at 100 mTorr) at 125 °C. The oxidized sample was then exposed to an H_2/SF_6 plasma at 125 °C (30 s at 100 mTorr) for varying gas ratios. NbN films were also etched using RIE as a reference for surface roughness and electrical properties. The RIE-etched films were prepared in an Oxford Instruments Plasmalab 100 ICP-RIE 380 System. NbN films were exposed to an SF_6/Ar plasma (20 s at 10 mTorr and 400 W ICP with 100 W bias) at 20 °C. Plasma parameters were based on reported fluorine-based RIE parameters for the fabrication of NbN SNSPDs [39, 64]. The RIE-treated films were etched from 30.1 nm to 22.1 nm for a total etched thickness of 8.0 $\pm$ 0.3 nm. For comparison, 50 cycle ALE-treated films were etched from 30.0 nm to 21.1 nm for an etched thickness of 8.9 $\pm$ 0.1 nm.

3.2 NbN ALE using O_2 and H_2/SF_6 plasmas

NbN oxidation using O_2 plasma

Our NbN ALE process was inspired by our prior work on TiN ALE using sequential O_2 gas and H_2/SF_6 plasma mixture exposures [74]. As a first attempt, we used the same exposure sequence on NbN. However, unlike TiN, we observed that the etch rate plateaued toward zero after 10 to 15 cycles. This outcome is not unexpected because the oxidation chemistry of Nb is notoriously complex, with Nb taking on oxidation states ranging from +2 to +5 [63]. Further, NbF_5 is the most volatile fluoride while fluorides with lower oxidation states are less volatile [35, 40, 61], meaning that the desired surface oxide to produce etching upon fluorination is Nb_2O_5. Considering these points, we hypothesized that the plateauing etch rate could be attributed to the formation of lower oxidation-state fluorides with low volatility.

A potential route to circumvent this issue is oxidation via oxygen plasma. Oxygen plasma has been reported to oxidize with lower activation energy compared to oxidation by molecular oxygen [33]. There is also previous literature on the oxidation of niobium metal showing that oxygen plasma produces an oxide with a higher concentration of Nb_2O_5 relative to the native oxide [55, 75, 198].

To verify that oxygen plasma exposure would produce a higher fraction of Nb_2O_5, we prepared two samples oxidized with either O_2 gas or plasma, as described in Section 3.1, and characterized the surface chemical environment with *ex situ* XPS. Figure 3.2 shows the Nb 3d spectra for each sample. We observe three peaks, each consisting of a doublet due to spin-orbit coupling. These peaks are assigned as NbN, NbO_xN_y, and Nb_2O_5 [31, 82, 112, 191]. The binding energies are listed in Section 3.2. The Nb_2O_5 subpeaks correspond to the +5 oxidation state of Nb when bonded to oxygen. Between the +3 oxidation state (corresponding to NbN) and +5 oxidation state, another component is observed. However, the composition of this component is difficult to determine as it may correspond to oxides of lower oxidation state such as NbO_2 or an oxynitride such as NbON, both of which have very similar binding energies [31, 82, 112]. In our analysis, we denote the middle subpeaks by NbO_xN_y as it is likely a combination of NbO_2 and NbON.

The presence of Nb_2O_5 can be quantified by computing the area fraction for each component for each sample. The results of the analysis are reported on Figure 3.2. After exposure to O_2 gas, Figure 3.2a shows almost equal fractions of Nb_2O_5 and NbO_xN_y with 29% Nb_2O_5 bonding. Figure 3.2b shows the surface spectra after exposure to O_2 plasma, with a Nb_2O_5 fraction of 72%. These results confirm that Nb oxidation using a plasma forms more of the +5 oxidation state oxide and less of the lower oxidation state species. The +5 oxidation state is preferred as it forms volatile fluorides which lead to etching. The use of oxygen plasma is therefore advantageous over oxygen gas for facilitating the etching of NbN.

Selectivity of H_2/SF_6 plasma

We next examine the etch rates of Nb_2O_5 and NbN films for varying SF_6:H_2 flow rate ratio, η. The use of H_2/SF_6 plasma was motivated by noting that HF weakly fluorinates TiN without increasing the oxidation state [106], but fluorine radicals cause spontaneous etching of NbN [66]. Due to practical limitations, we are unable to use HF vapor, so we used an H_2/SF_6 plasma mixture instead. H_2 and fluorine-containing gas plasma mixtures have long been known to produce vibrationally-

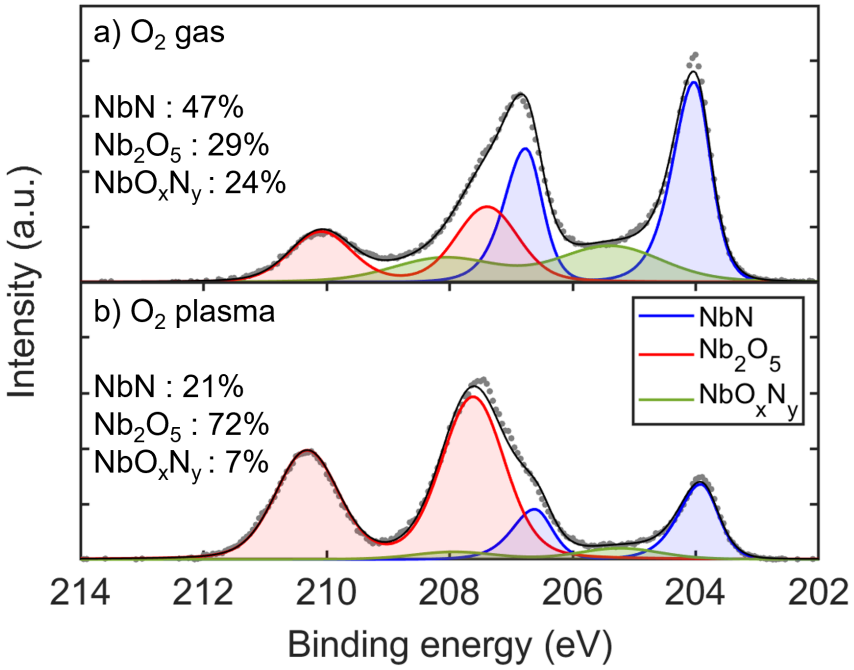

Figure 3.2: Surface XPS spectra showing Nb 3d spectra for NbN films exposed to (a) O_2 gas and (b) O_2 plasma for 120 s. The measured (gray dots) and fit spectra (black lines) intensity are reported in arbitrary units (a.u.) against the binding energy on the x-axis. The y-axis scales are identical for both spectra. The percent concentrations of the NbN, Nb_2O_5 and NbO_xN_y bonds are reported in the figure.

excited HF which has been exploited for realization of chemical lasers [69, 140, 142]. Prior studies using a hydrogen and fluorine-containing gas mixture plasma have shown that the products formed depend on the gas flow rate ratio. In particular, the formation of HF molecules and suppression of F radicals at sufficiently high H_2 flow rates has been studied as it leads to etch selectivity [56, 83, 147, 182]. We note that while the formation of vibrationally excited HF in the plasma has been established in prior studies [56, 83, 140, 147, 182], the actual state of the HF by the time it impinges onto the film surface in the present experiment is unknown.

Figure 3.3a shows the etch rates of NbN and Nb_2O_5 versus η at 125 °C. For $\eta \lesssim 0.1$, negligible etching is observed in both films. For $\eta \geq 0.1$, we observe spontaneous etching of Nb_2O_5, with the etch rate increasing with η. For NbN, we observe no etching for $\eta \leq 0.3$. Instead, negative etch rates ~ -0.05 Ås^{-1} are observed, corresponding to an increase in the thickness of the film, which we assume to be growth of non-volatile lower oxidation state niobium fluorides. For $\eta \geq 0.4$, etching of NbN is observed. The etch selectivity of the oxide over the nitride observed for

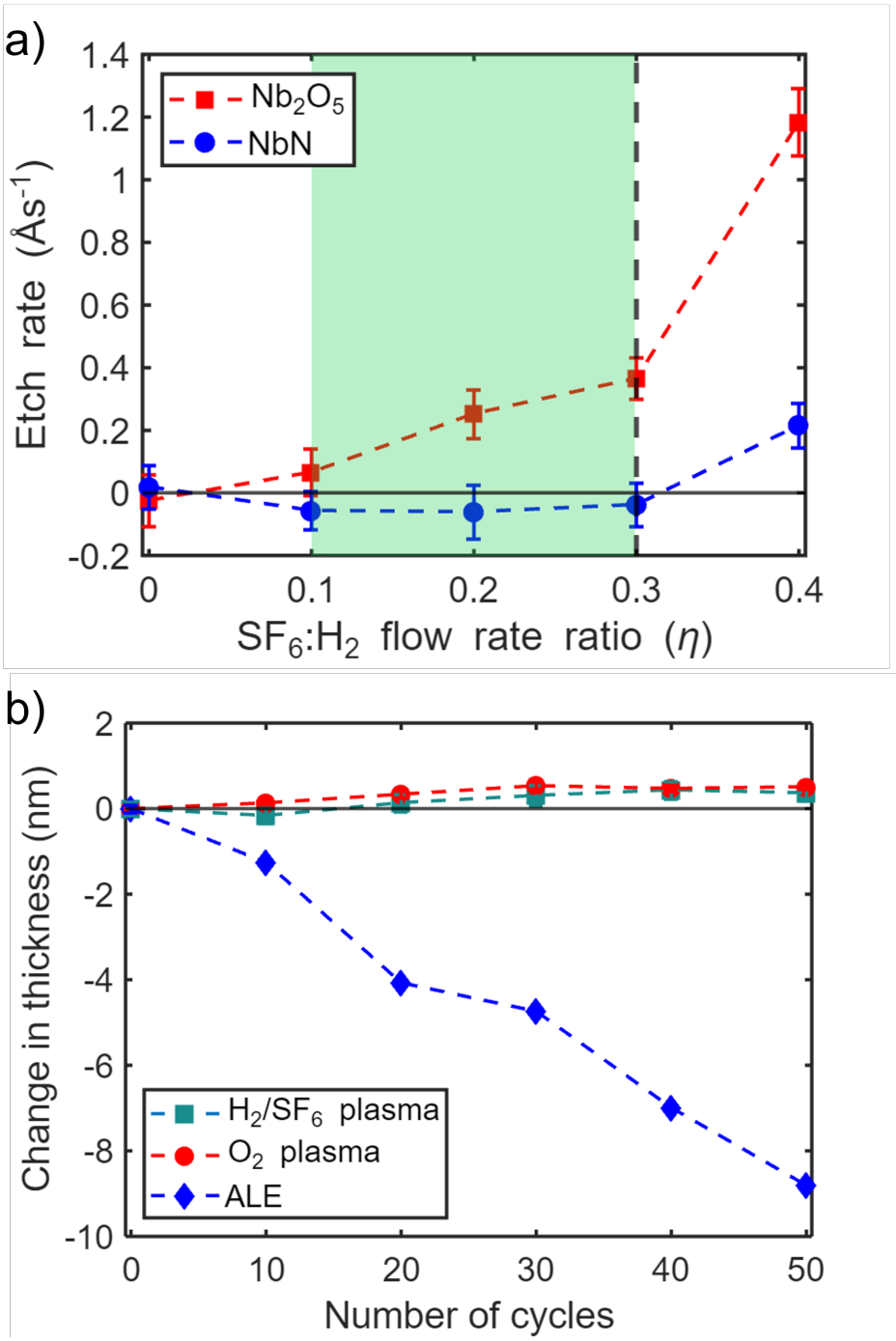

Figure 3.3: (a) Etch rate of NbO_x and NbN versus the SF_6:H_2 flow rate ratio. The green shaded area represents the flow rate ratios for which selective etching of NbO_x over NbN was achieved. The black dashed line at a ratio of 0.3 represents the ratio used in the ALE experiments, and a solid line at 0 Å/cycle is plotted as a reference. (b) NbN thickness change versus number of cycles with exposure only to O_2 plasma (red circles), H_2/SF_6 plasma (green squares) and full ALE process at 125 °C (blue diamonds). A solid line is plotted at 0 nm as a reference. The dashed lines are guides to the eye.

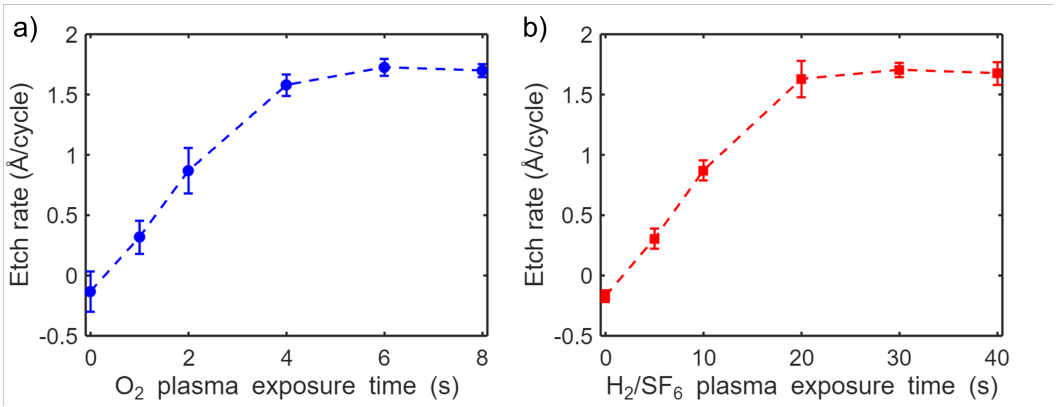

Figure 3.4: (a) NbN etch per cycle (EPC) versus O_2 plasma exposure time with H_2/SF_6 plasma exposure time fixed at 30 s. (b) EPC versus H_2/SF_6 plasma exposure time while O_2 plasma time is fixed at 6 s. The EPC is observed to saturate with increasing exposure time for each half step.

$0.1 < \eta \leq 0.3$, may be attributed to the *in situ* formation of HF molecules in the plasma mixture [56, 83, 147, 182]. For $\eta \geq 0.4$, the concentration of F radicals becomes sufficient to spontaneously etch the NbN, leading to etching of both films. From our measurements, we find that $0.1 \leq \eta \leq 0.3$ achieves selective etching of Nb_2O_5 over NbN. To obtain the highest etch selectivity of Nb_2O_5 over NbN, we select $\eta = 0.3$ for our experiments. This ratio is used throughout the rest of the paper.

NbN ALE using O_2 and H_2/SF_6 plasmas

Figure 3.3b shows the thickness change of NbN versus number of cycles for the oxidation step, fluorination step, and for the full ALE recipe at 125 °C. For the half-cycles, the thickness change was measured after exposure to only O_2 plasma or H_2/SF_6 plasma. No etching was observed for either half-cycle. In contrast, we observe a decrease in the thickness with increasing number of cycles when using both steps. The etch rate is calculated by dividing the total thickness change by the number of cycles, resulting in an etch per cycle (EPC) of 1.77 ± 0.06 Å/cycle at 125 °C. Based on the etch per cycle of the half cycles and overall cycle, the synergy is 100% [85].

We also measured the saturation curves of each half step. Figures 3.4a and 3.4b show the EPC versus exposure time of O_2 plasma and H_2/SF_6 plasma, respectively. For each saturation curve, the purge times and exposure time for one half-cycle are fixed, while the exposure time for the other half-cycle is changed. The reported EPC

values were calculated from the thickness change measured after 30 cycles at 125 °C. In Figure 3.4a, the H_2/SF_6 plasma time is fixed at 30 s and the O_2 plasma time is varied. The etch rate is observed to saturate to 1.75 ± 0.04 Å/cycle after 6 s of O_2 plasma exposure. Similarly, in Figure 3.4b the O_2 plasma time is fixed at 6 s while the H_2/SF_6 plasma exposure time is varied. The etch rate is found to saturate at 1.74 ± 0.06 Å/cycle after 30 s of H_2/SF_6 plasma exposure. The saturation of both half-cycles indicates that the process is atomic layer etching.

Surface morphology characterization

We characterized the effect of ALE and RIE on surface morphology using AFM. Figure 3.5a shows a 250×250 nm^2 height map of the original sputtered NbN film. The root mean square roughness of the scan was $R_q^{\text{original}} = 0.67$ nm. Figure 3.5b shows a height map of the RIE-treated film with $R_q^{\text{RIE}} = 0.97$ nm, which is 45% rougher than the original. Figure 3.5c shows a height map for the ALE-treated film after 50 cycles, which is 55% smoother with $R_q^{\text{ALE}} = 0.30$ nm. The R_q values were found to vary by $\lesssim 7\%$ between 3 locations on each film.

Figure 3.5d shows the calculated PSD for the original, ALE-treated, and RIE-treated samples. A comparison of the PSDs at different spatial frequencies indicates the extent of smoothing or roughening at various length scales. The RIE film's PSD is within $20 \pm 5\%$ of that of the original film over spatial frequencies from $\sim 0.05 - 0.14$ nm^{-1}. For spatial frequencies larger than 0.14 nm^{-1} and smaller than 0.05 nm^{-1}, the RIE-treated surface is significantly rougher than the original sputtered surface, with the RIE PSD being more than 100% larger at some spatial frequencies. We also observe that the ALE film's PSD is smaller than the original film's PSD across all spatial frequencies, indicating that ALE smooths the film over the length scales shown in Figure 3.5d.

Surface and bulk film composition

We next characterize the surface composition of NbN before and after ALE. In Figure 3.6, the XPS spectra for Nb 3d, N 1s, F 1s, and O 1s are shown for an untreated and an ALE-treated sample. In Figure 3.6a, we report the Nb 3d spectra for the original sample and ALE-treated film. We resolve three components consisting of doublets identical to the components shown in Figure 3.2. We observe subpeaks corresponding to NbN (203.8 and 206.6 eV), NbO_xN_y (206.7 and 207.1 eV), and Nb_2O_5 (207.1 and 209.8 eV) bonding [31, 82, 112, 191]. The binding energy values corresponds to the $3d_{5/2}$ and $3d_{3/2}$ peaks, respectively. Figure 3.6b shows the N 1s

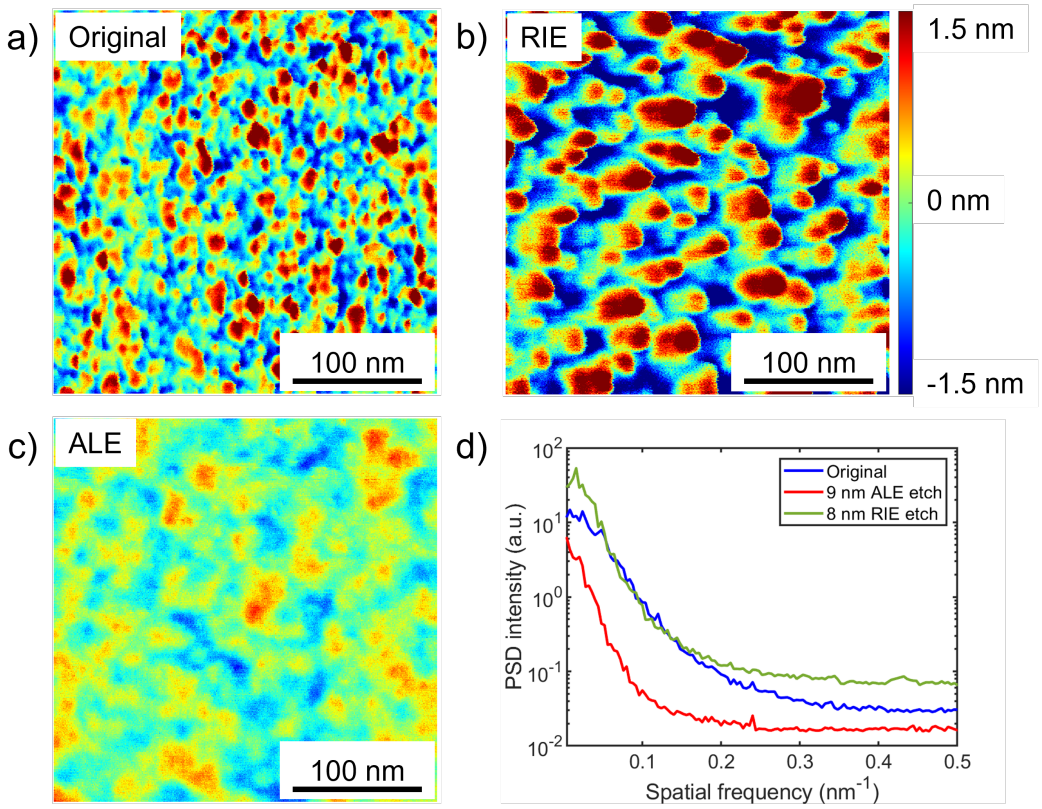

Figure 3.5: AFM scan showing height-maps of (a) original sputtered sample, (b) after 8 nm etching with RIE, and (c) after 50 cycles ALE etching of the original sample, corresponding to 9 nm of etching. (d) PSD of samples (a)-(c) showing the roughening after RIE and smoothing after ALE.

spectra, where we observe peaks corresponding to N-Nb (397.6 eV) and N-O (399.6 eV) bonds [31, 82, 112]. Figure 3.6c shows the F 1s spectra, where we observe a single peak attributed to Nb-F (684.7 eV) bonding [154]. In Figure 3.6d, we report the O 1s spectra with two subpeaks, corresponding to O-Nb (531.1 eV) and O-N (532.4 eV) bonding [31, 112, 191].

After ALE, we observe a decrease in the magnitude of O-Nb and Nb_2O_5 components compared to the original spectra. This decrease in oxygen content after ALE has been observed in ALE of other materials [68, 74, 128, 185]. A F-Nb peak appears in the F 1s spectra after ALE which was previously absent. The increase in fluorine after ALE using a fluorine-containing plasma has also been observed in ALE processes [19, 22, 44, 68, 185].

We quantified the elemental composition at the surface and bulk of the original and ALE-treated films using depth-profile XPS. Figure 3.7 shows the atomic percentages

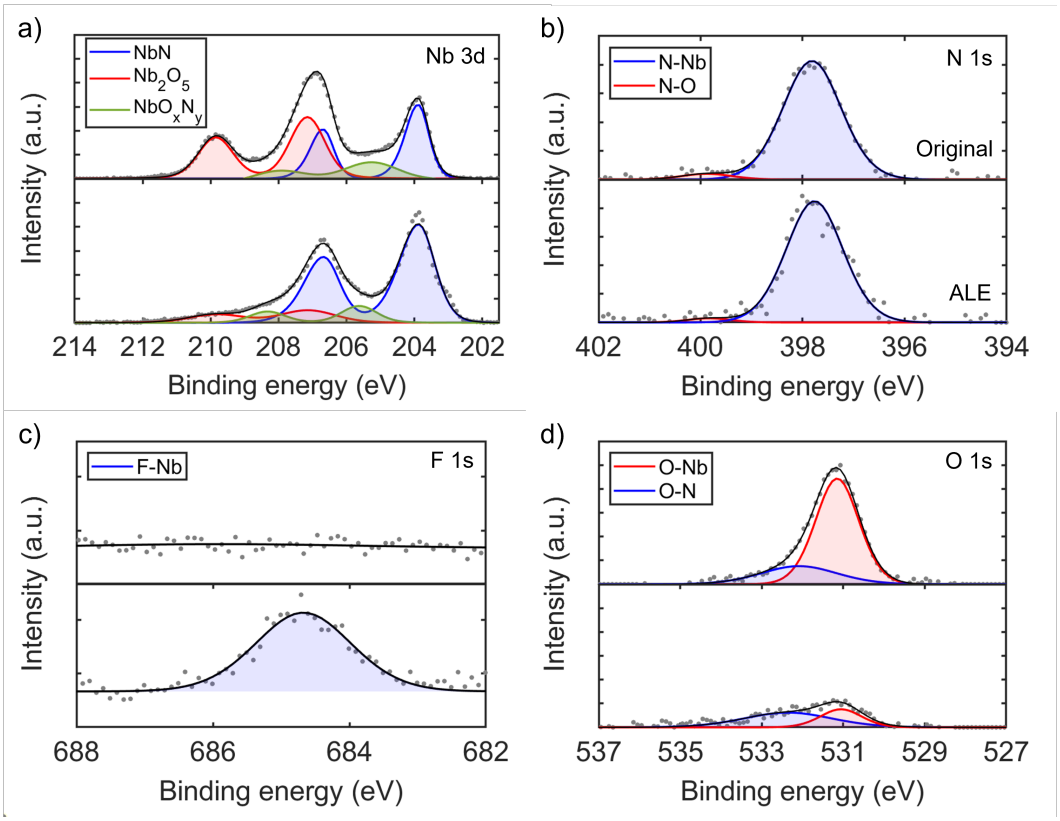

Figure 3.6: Surface XPS spectra showing (a) Nb 3d, (b) N 1s, (c) F 1s, and (d) O 1s spectra. The spectra is shown for (top) original and (bottom) ALE-treated NbN films. The measured (gray dots) and fit spectra (black lines) intensity are reported in arbitrary units (a.u.) against the binding energy on the x-axis. The y-axis ticks are at the same intensity value for the original and ALE spectra within each element.

of Nb, N, F, O, and C elements versus Ar milling time and estimated depth for the original sample and after 50 cycles of ALE. In Figure 3.7a, we report the surface composition of the original sample as 38.4% Nb, 26.8% N, 27.9% O, 6.9% C, and 0% F. The composition of the original sample tends toward bulk values after 75 s of milling. The bulk atomic fractions are ~ 56.2% Nb, 37.6% N, 6.2% O, 0% C, and 0% F.

The atomic percentages of Nb, N, and O follow qualitatively similar trends to those reported in other XPS studies of NbN. Specifically, the O concentration is observed to decrease from the surface value to the bulk value for a sufficiently long milling time, while the Nb/N ratio increases from the surface values to a value below unity in the bulk [24, 31, 82, 112, 191]. The surface spectra from carbon indicates the presence of C-O and C-H bonds, typical of adventitious carbon originating from

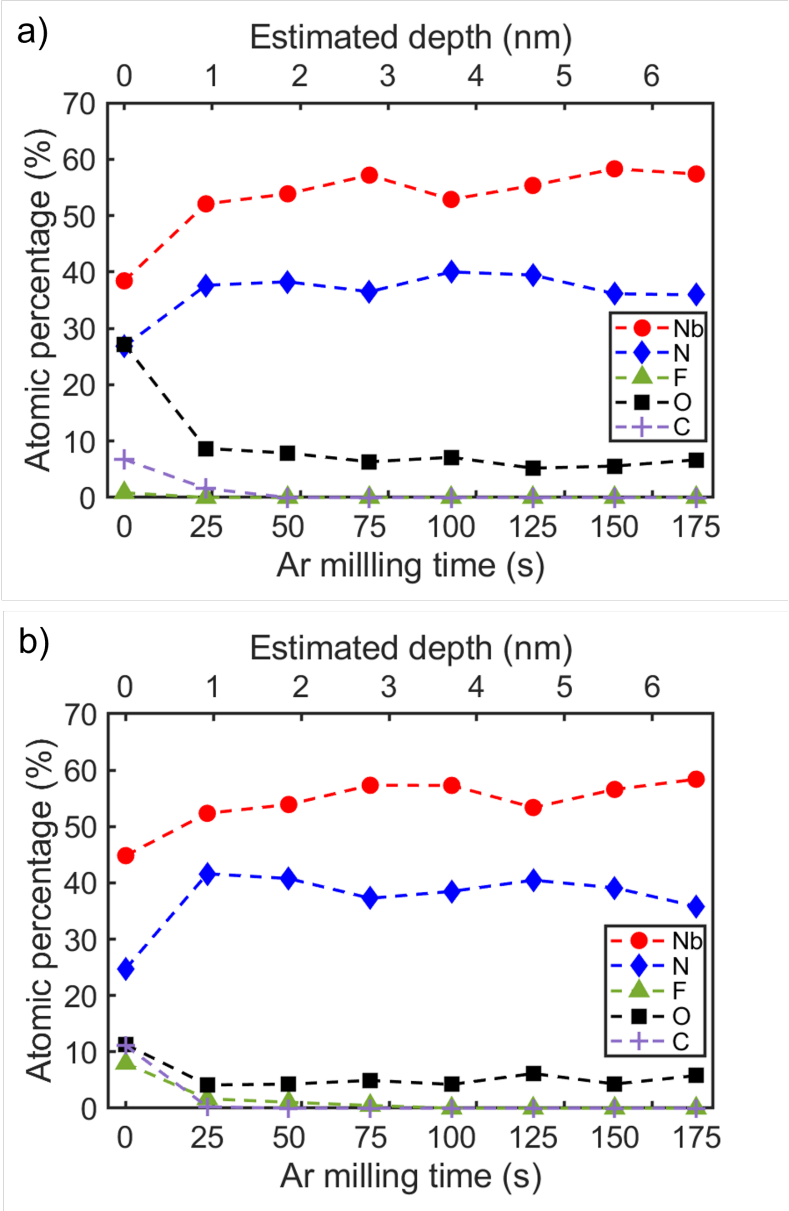

Figure 3.7: Atomic concentrations of Nb, N, F, O, and C versus Ar milling time and estimated depth for (a) original and (b) ALE-treated NbN thin films. The uncertainty for the data points is smaller than the size of the markers.

exposure to ambient air [191]. Oxygen contamination in bulk is often seen in sputtered polycrystalline Nb thin films [118, 120].

In Figure 3.7b, we report the surface composition of the ALE-treated sample as 44.8% Nb, 26.7% N, 11.3% O, 10.1% C, and 7.1% F. The composition of the ALE sample tends toward bulk values after 75 s of milling. The bulk atomic fractions are ~ 56.3% Nb, 37.9% N, 5.8% O, 0% C, and 0% F after 75 s milling or ~ 3 nm. After ALE, the surface oxygen concentration decreases by 59%. The surface fluorine is observed to increase after ALE which is consistent with prior work [19, 22, 44, 68, 185]. The fluorine contamination is observed to drop to below detection limits (< 0.1%) after 50 s of Ar milling (< 2 nm). The bulk atomic concentrations before and after ALE are found to vary by < 6%. Thus, we conclude that the effect of ALE is confined to the first few nanometers of the film and negligibly affects the bulk chemical composition.

Cryogenic electrical properties

We investigated the effect of ALE and RIE on the electrical and superconducting properties of the NbN films by measuring their resistivity from 5 to 20 K. A 30 nm NbN film served as a reference. Another 30 nm film was etched using 50 cycles of ALE to 21 nm. Finally, a 30 nm NbN film was etched to 22 nm using RIE. Figure 3.8 shows the measured resistivity versus temperature for the three films. The resistivity at 20 K and T_c of the original 30 nm film were found to be 259 ± 10 $\mu\Omega$cm and 11.21 ± 0.07 K, respectively. The resistivity at 20 K for the ALE-treated film was 249 ± 9 $\mu\Omega$cm while for the RIE-treated film it was 257 ± 10 $\mu\Omega$cm. We also measured $T_c^{\mathrm{ALE}} = 10.95 \pm 0.07$ K and $T_c^{\mathrm{RIE}} = 10.51 \pm 0.08$ K.

While a decrease in T_c with decreasing thickness is expected, we note that $T_c^{\mathrm{ALE}} > T_c^{\mathrm{RIE}}$ by 4.1% even though the RIE-treated film is thicker than the ALE-treated film. We may estimate the T_c of the ALE film if it were the same thickness as the RIE sample (22.1 nm) using a scaling law relating film thickness and T_c (see Eq. 1 in Ref. [77]). We calculate $T_{c,2}^{\mathrm{ALE}} = 11.05$ K, corresponding to a 5.0% higher T_c compared to the RIE sample of the same thickness. We attribute this difference to the low-damage nature of ALE compared to RIE. This experiment goes a step further than prior work [74] by directly comparing the electrical and superconducting properties of samples treated by ALE and RIE, the latter being the state-of-the-art etching technology for superconducting devices at present.

We now discuss the characteristics of our NbN ALE process in comparison to the

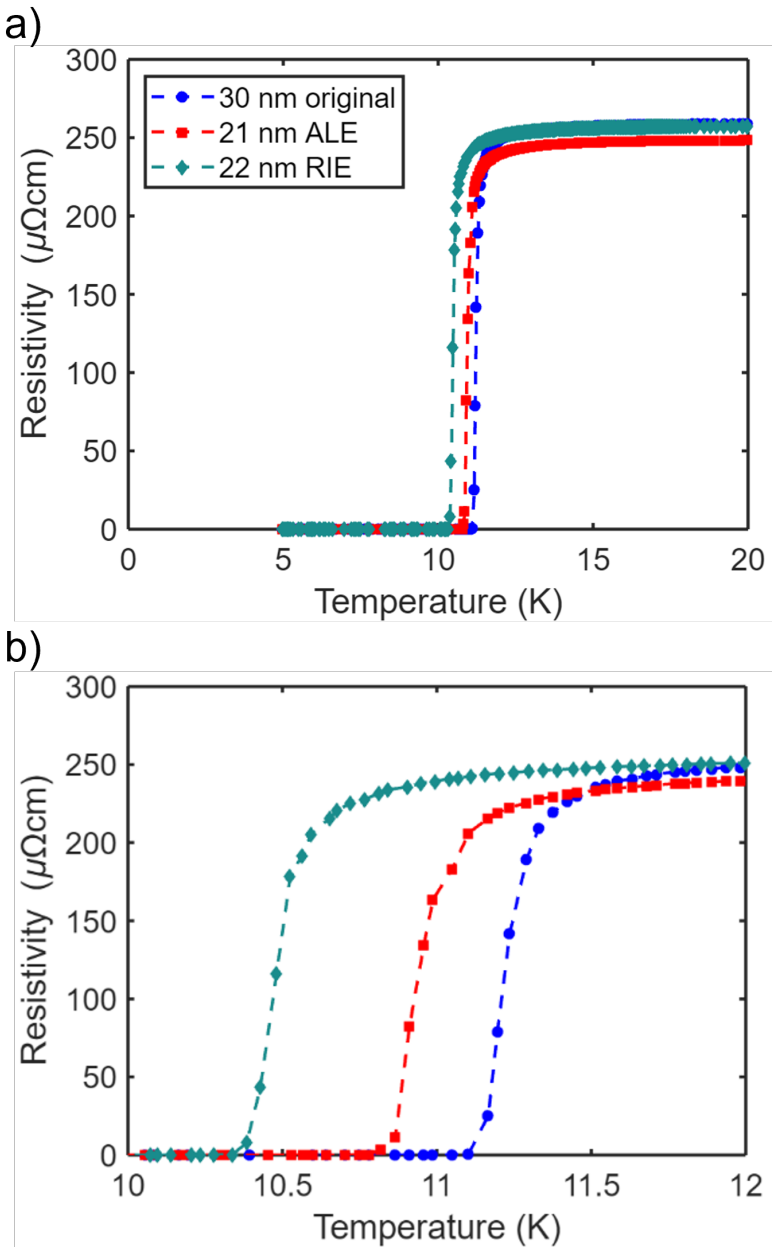

Figure 3.8: a) Resistivity versus temperature for original 30 nm NbN film (blue circles), 21 nm thick ALE-treated film (red squares), and a 22 nm RIE-treated NbN film (green diamonds). b) Resistivity versus temperature plot with a truncated x-axis to highlight the superconducting transitions. The dashed lines are guides to the eye.

closest analogous processes, ALE of TiN. ALE of TiN has been reported using two primary approaches: oxidation followed by fluorination to etch using volatile fluorides at the same temperature [74, 106], and fluorination or chlorination followed by thermal cycling to volatilize Ti-halides [130, 171]. The first approach achieves atomic-scale control with EPCs between 0.20 Å/cycle [106] and 2.4 Å/cycle [74] at 200 °C. However, Ref. [106] uses HF vapor, which requires long purge times and is not routinely available in conventional processing tools. The second approach yields EPCs exceeding 17 Å/cycle, which decreases processing times but lacks the etch depth precision desired for surface processing. Further, the use of thermal cycling can lead to impractical process times on conventional tools.

The present NbN process achieves an EPC of 1.77 Å/cycle at 125 °C and is most comparable to the TiN EPC of 2.4 Å/cycle at 200 °C obtained in Ref. [74], which also used an H_2/SF_6 plasma instead of HF. However, the present recipe uses O_2 plasma compared to the O_2 gas used in Ref. [74]. The use of O_2 plasma was necessitated by the complex chemistry of Nb and the need to maximize the proportion of the +5 oxidation state oxide. Our results indicate that O_2 plasma increased the Nb_2O_5 ratio by $\sim$ 250% compared to O_2 gas. The increase in Nb_2O_5 content led to a reproducible etch per cycle over 50 cycles, which was not achievable using O_2 gas. The temperature dependence of the EPC for the reported NbN ALE recipe has not been studied and is an interesting topic for future work.

Our plasma-thermal ALE process may find potential applications in the etching of NbN-based superconducting quantum devices such as microwave kinetic inductance detectors, where the native oxide leads to cryogenic microwave loss that presently limits device performance. On the basis of our XPS and resistivity measurements, ALE-treated films have a reduced oxygen concentration while maintaining unaltered bulk chemistry and electrical properties. These properties make ALE promising for reducing the cryogenic microwave loss arising from the metal-air interface and thereby improving the quality factor of superconducting microresonators. The present process could be used as a post-treatment process by removing the few-nanometer-thick lossy surface region present after the primary etch process. However, we also note that the process leaves a $\sim$ 2 nm fluoride layer which has an unknown effect on the cryogenic microwave loss. The smoothing effect and Angstrom-scale EPC of the present process is also potentially relevant for fabricating NbN-based single nanowire single photon detectors where the sidewall roughness and other inhomogeneities negatively impact device metrics.

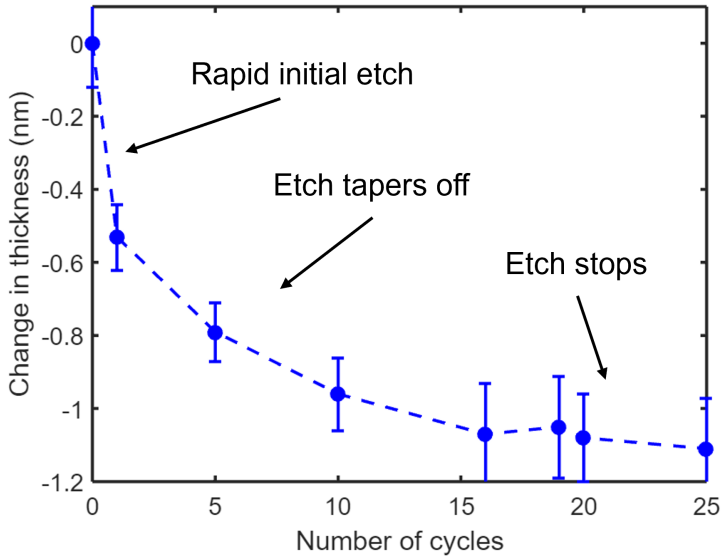

Figure 3.9: NbN thickness change versus number with exposure to oxygen gas and SF_6/H_2 plasma.

Other attempted methods for ALE of NbN

The recipe reported in Section 3.2 was not the first iteration of an NbN ALE recipe. Multiple other schemes were attempted to varying levels of success. They are discussed chronologically.

At first, the exact TiN ALE recipe from Section 2.3 was used to etch NbN. The etch characteristics of using the TiN recipe are shown in a thickness change versus number of cycles plot in Figure 3.9. In the first few cycles, an etch was measured, which then tapered off until $\sim$ 1 nm was etched, after which the etch came to a stop. Further XPS analysis indicated that the native oxide etched quickly, but the O_2 gas in the oxidation step was unable to produce enough +5 oxide to keep the etch going, ultimately leading to no more etching. Continuing with this recipe past 25 cycles (not shown in Figure 3.9) eventually lead to a 0.3–0.4 nm increase in the thickness, which is predicted to be the growth of fluorides.

Due to the challenge of growing a +5 oxide at elevated temperatures [187], the next attempt used a thermal cycling method. The native oxide was found to be etched successfully in prior attempts, so we tried to replicate the native oxide growth. The idea is illustrated in Figure 3.10. The NbN sample was first etched in the in-situ HF plasma at 300 °C, after which the sample was transferred to the loadlock where it was exposed to ambient air at room temperature for 1 minute. The sample was then loaded into the chamber to etch again and restart the cycle. Overall, this process

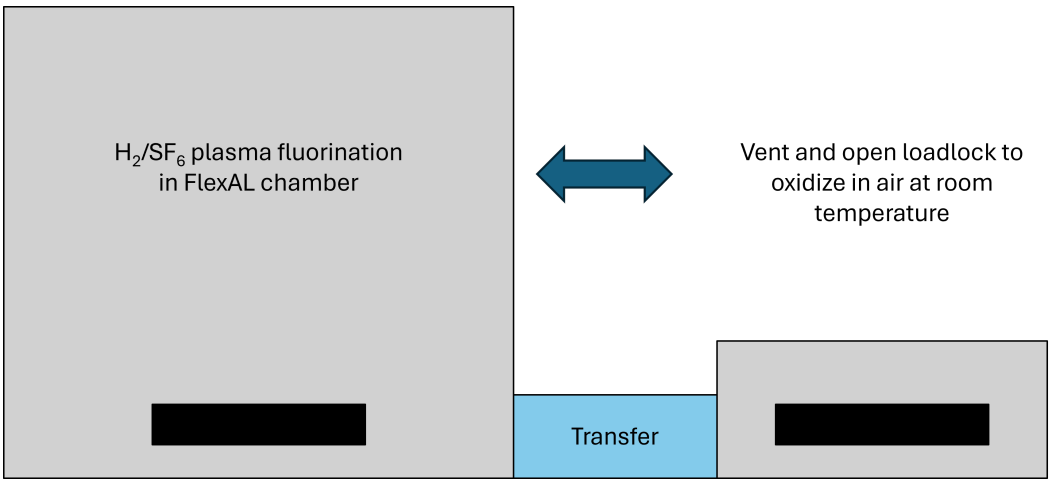

Figure 3.10: Schematic showing the method used to etch NbN by oxidizing at room temperature and fluorination in the plasma chamber.

created an etch rate of 1.1 Å/cycle. However, the time per cycle was prohibitive at ~ 10 minutes/cycle. Etching a nanometer would take almost 90 minutes, and since the process cannot be automated on the FlexAL, someone would have to stay there the entire time.

Finally, one other method was attempted by adding a bias to the fluorination step, keeping the oxidation step as molecular oxygen. The idea was that the increased energy in the fluorination step would allow for etching of the lower oxidation state oxides along with the Nb_2O_5. In addition to the 300 W plasma power, a 5 W (3–7 V) DC bias was applied to the *in situ* HF plasma. This process resulted in a linear etch rate of 1.25 Å/cycle over 40 cycles at 125 °C. However, the process had a synergy of 77%, and further study was stopped to focus on the recipe in Section 3.2.

3.3 NbN ALD using TBTDEN and H_2 plasma

NbN ALD has been reported using $NbCl_5$, (tert-butylimido)-tris (diethylamino)-niobium (TBTDEN), and Tert-butylimido tris(methylethylamino)niobium (TBTMEN) [88]. The first plasma-enhanced ALD (PEALD) of NbN was reported using TBTMEN and an N_2/H_2 plasma for use as metal gate electrodes in CMOS devices [71]. Ref. [71] reported their lowest normal resistivity at ~ 1000 $\mu\Omega$cm for a 20 nm thick NbN film. The first superconducting ALD NbN was reported in Ref. [202] with a maximum T_c of 10.2 K. Since then, the highest T_c ever reported in NbN PEALD literature was 13.7 K for a 37 nm thick film with a normal resistivity of 173 $\mu\Omega$cm, achieved using TBTDEN and an H_2/N_2 plasma [174]. TBTDEN pro-

vides both niobium and nitrogen atoms, while the hydrogen plasma reacts with the organic compounds (functional groups) of the precursor remaining on the substrate surface.

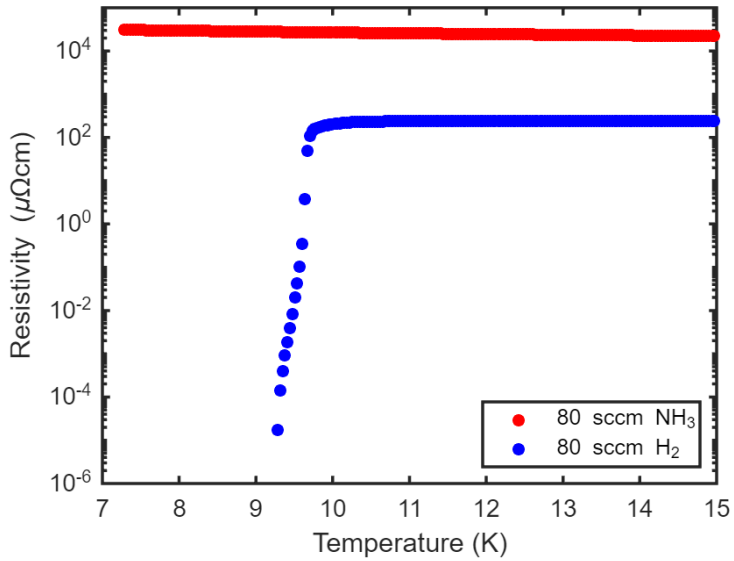

Figure 3.11: Resistivity versus temperature for 26 nm NbN ALD films grown with different gas mixtures: 80 sccm H_2 and 20 sccm N_2 (red) and 80 sccm H_2 only (blue). The y-axis is on a log-scale to accommodate the film without a transition.

The FlexAL in the KNI is fitted with TBTDEN, so that is the precursor used in this thesis. The recommended tool recipe for PEALD NbN used a 1 s TBTDEN dose time and a 10 s NH_3 plasma time at 200 °C. Films were grown on Si using this method and exhibited a resistivity of 45 Ωcm and did not display a superconducting transition above 2 K. Based on the PEALD NbN literature at the time [174], many changes were made to the default recipe. Due to the lattice mismatch between Si and NbN, a buffer layer on Si was used. At first a 100 nm sputtered SiO_2 buffer layer was used, but its cryogenic electrical properties showed no difference from the NbN on Si chip. Then, a 1.1 µm thermally grown SiO_2 buffer layer was used. This, along with a change in the plasma chemistry from NH_3 to H_2 was implemented. In Figure 3.11 the resistivity versus temperature curves for two 30 nm NbN films are shown. Both films were grown on a 1.1 µm thermally grown SiO_2 buffer layer with a 3 s TBTDEN dose time and 15 s plasma time. The plasma was struck with 400 W ICP and a 30 W DC bias. The film grown with NH_3 plasma (red) was not superconducting, with a normal resistivity of 31.6 mΩcm. The film grown with H_2 plasma only resulted in the first superconducting NbN ALD film in this study with

a T_c of 9.78 K and a normal resistivity of 295 $\mu\Omega$cm at 15 K. This film is referred to as NbN 1 in Figure 3.12.

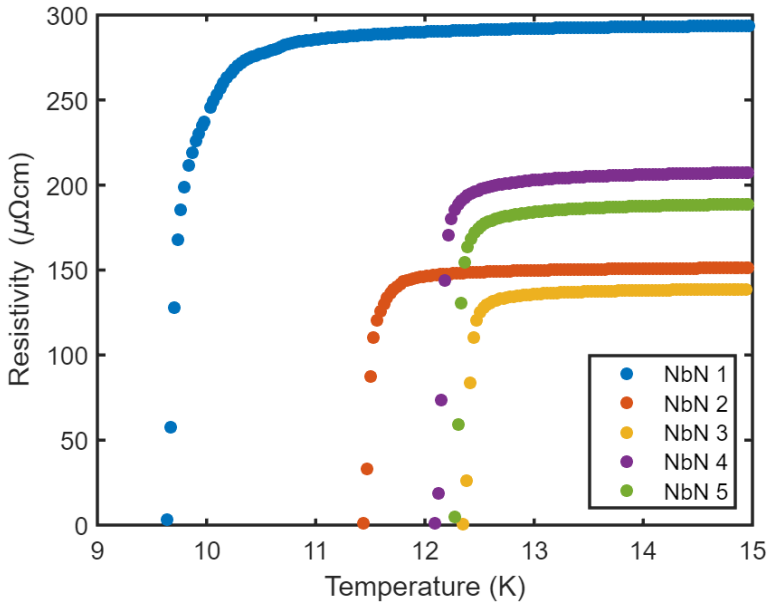

Figure 3.12: Resistivity versus temperature for selected PEALD NbN films grown under various conditions. Note that the x-axis goes from 9 – 15 K.

Figure 3.12 shows the resistivity versus temperature curves for various PEALD NbN films grown under different conditions. All films in Figure 3.12 are $\sim$ 60 nm except for NbN 1 which is 30 nm. Multiple changes were made between NbN 1 and NbN 2: the plasma time was increased from 15 s to 30 s, and the temperature was increased from 200 °C to 300 °C. The plasma time increase was used to make sure that the ALD process was in saturation and ensure that all the precursor had been reacted with [174, 202]. The temperature increase has also been shown to reduce resistivity and increase T_c by increasing the size of the crystal grains [174, 202]. These changes resulted in a T_c of 11.48 K and a normal resistivity of 155 $\mu\Omega$cm in NbN 2. NbN 3 followed the same recipe as NbN 2, except it was deposited at 400 °C NbN 3 had the highest T_c in this study of 12.42 K, and the beat the lowest resistivity ever reported in PEALD NbN literature (173 $\mu\Omega$cm) with a normal resistivity of 140 $\mu\Omega$cm. NbN 4 and 5 followed the same recipe as NbN 2 and NbN 3, but it was deposited at 500 °C. NbN 5 was deposited on SSP sapphire instead of SiO_2. NbN 4 had a T_c of 12.18 K and a normal resistivity of 284 $\mu\Omega$cm. NbN 5 had a T_c of 12.33 K and a normal resistivity of 224 $\mu\Omega$cm. The degradation in T_c and resistivity at 500 °C is thought to be due to the decomposition of the organometallic precursor at

such high temperatures, along with the increased diffusion of oxygen into the film from the vacuum background. Both issues would cause an increase in the carbon and oxygen contamination leading to poorer film quality. Depth profile XPS would have been ideal to justify these assumptions. However the MMRC Ar milling was unavailable at the time of this study.

Figure 3.13 shows an 500×500 nm^2 AFM scan of the NbN 5 film. The 62 nm film was deposited over 1000 cycles resulting in a growth rate of 0.62 ± 0.01 Å/cycle. The ALD NbN 3 had a surface roughness, R_q, of 0.26 ± 0.04 nm, demonstrating the low surface roughness of ALD NbN films.

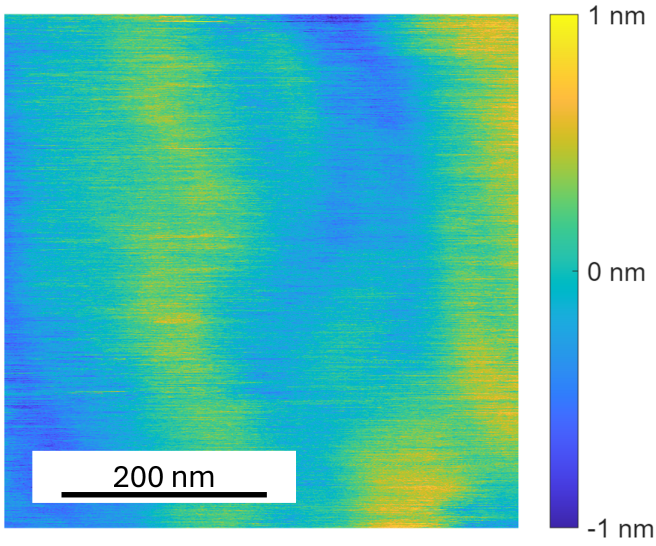

Figure 3.13: 500 nm × 500 nm AFM scan of 62 nm ALD NbN 5.

3.4 Fabrication of NbN/AlN/NbN junctions

Using the lessons learned from the junction fabrication in Section 4.4, we fabricated all ALD SIS junctions. ALD provides two unique advantages over traditional deposition methods by being able to deposit smooth thin films with minimal pinholes. The work in this section was motivated by promising results shown in Ref. [184], where they used ALD to deposit all the layers in NbN/AlN/NbN junctions with no vacuum break. To summarize some key results, Ref. [184] obtained a subgap ratio of $Q_R \sim 47$, $V_{gap} = 4.2$ mV, and $J_c = 12$ A/cm^2 for a junction with a 2 µm diameter. While this paper used the junctions in qubits, we were interested in the fabrication of ALD junctions for use as SIS mixers. To this end all ALD NbN/AlN/NbN junctions were fabricated in the KNI using the same final design as Figure 4.14. A summary

is provided in this section and further fabrication process details are covered in Section 4.4.

The fabrication started with building the NbN/AlN/NbN trilayer. Due to the poor superconducting properties of NbN on Si films grown using ALD, as shown in Section 3.3, films were grown on thermally oxidized Si quarter wafers. High resistivity Si wafers (100) were thermally oxidized to grow ~ 800 nm SiO_2. Due to previously observed overetching into Si, which led to many open devices in Section 4.4, a 30 nm AlN layer was deposited on the SiO_2 to act as an etch stop. The SiO_2/Si wafers were cleaned by sonicating in acetone for 10 minutes and then rinsing in IPA and water. After cleaning, the wafer was loaded into the ALD chamber. Without any vacuum break, four layers are sequentially deposited on the SiO_2. First 30 nm of AlN is deposited as the etch stop, followed by 50 nm NbN for the bottom electrode, followed by 1–2 nm AlN for the junction barrier, and finally 50 nm NbN for the top electrode. The uncertainty in the thickness of the AlN barrier comes from the fact that the growth rate of AlN on top of NbN had not been characterized. Based on the growth rate of AlN on SiO_2, a 2 nm thick barrier was predicted, but ellipsometry measured a 1.1 nm thick barrier. Due to the thick metals in the stack ellipsometry is not reliable for this measurement and some sort of cross-section imaging would be necessary to measure the true thickness of the barrier. However, such a measurement was not in the scope of the project. After trilayer deposition, the wafer is ready for patterning.

Before any of the devices can be defined, alignment markers have to be deposited. Liftoff with S1805 photoresist was used to pattern a stack of 10 nm Ti/100 nm Au for both photo- and e-beam lithography alignment markers. Alignment markers are followed by the mesa etch. The mesa etch was used to define the ground plane (bottom electrode NbN) and remove metal from all unnecessary areas. AZ10XT photoresist was used to define the etch areas, and an SF_6/Ar RIE is used to etch away the NbN and AlN layers. The plasma parameters are 50 sccm SF_6 and 50 sccm Ar at 10 mTorr and 30 °C, with plasma power of 600 W ICP and 60 W RF for 8 minutes. The RIE recipe was found to etch NbN at a rate of 25 nm/min and AlN at 1 nm/min. After the mesa etch, a 3 minute oxygen ash was done to remove the burnt photoresist. The first set of devices failed due to improper removal of the burnt photoresist. Hardened resist around the edges led to fencing around the bonding pads and eventually caused the wiring trace to break from the contact pads upon thermal stress from cooling and heating the chips in a He dewar. The thermal stress

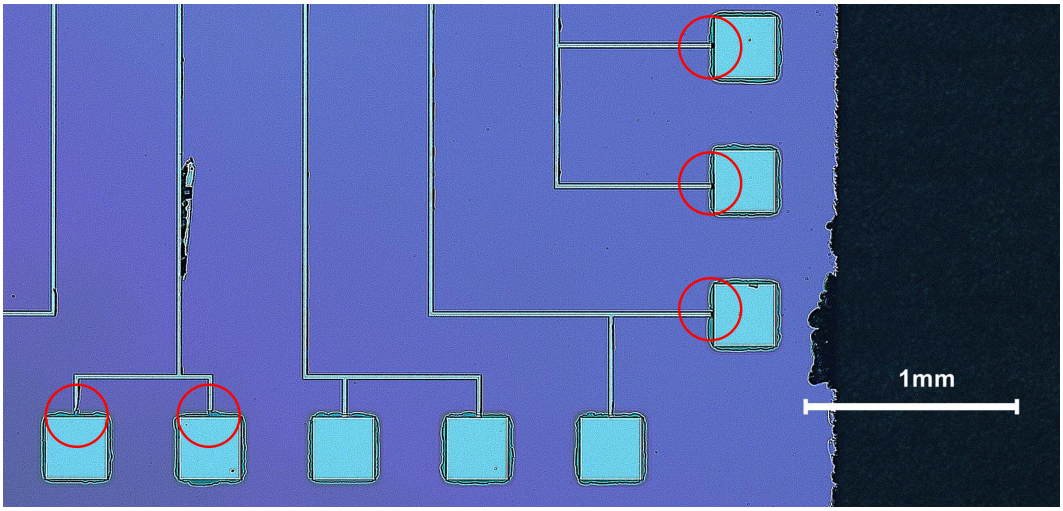

Figure 3.14: Optical microscope image of the first ALD SIS junction run showing the broken wiring trace which led to open connections to the bonding pads. The red circles are used to highlight the open connections.

was caused accidentally when the chips were wirebonded improperly and needed to be taken out of the dewar to re-wirebond. In the second run a 10 minute isotropic ashing was done to remove the burnt photoresist prior to stripping in heated Remover PG. The mesa etch was followed by junction definition.

For the junction definition step, the junction areas were patterned by e-beam pattern generation (EBPG) using ma-N 2405 negative tone e-beam resist. The top electrode was etched using the same SF_6/Ar RIE from the mesa etch, but with a 3 minute etch time. After etching away the top electrode, an interlayer dielectric (ILD) of 200 nm SiO_2 was evaporated. The ILD was patterned using the same resist from the junction etch and finally lifted off in heated Remover PG. The self-aligned liftoff was used to minimize the number of steps that require EBPG and improve alignment accuracy.

Finally, the wiring trace is deposited to connect the bonding pads to the junctions. The wiring was initially patterned by liftoff using S1813 photoresist. To account for trenching, overetching and fencing caused by prior fabrication steps, a 400 nm Nb wiring layer was used. However, the sputtering of such thick metal led to liftoff issues in the first run. In the second run a bilayer resist using LOR5A and S1813 was used for the liftoff with no issues.

The first set of devices had broken connections due to fencing around the contact pads. 9 out of 12 junctions were open when measured, 1 was shorted and 2 showed washed out IVs with a very high series resistance of $\sim 60\ \Omega$. An image from the

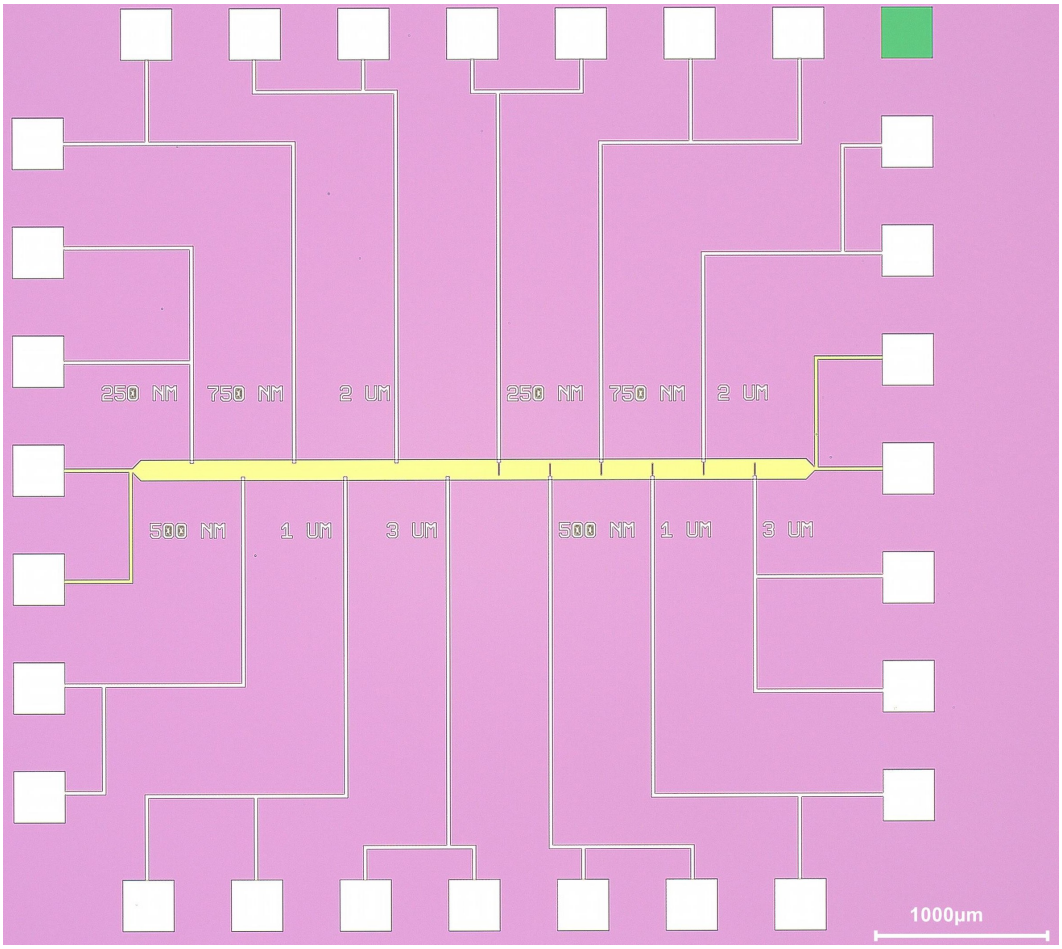

Figure 3.15: Optical microscope image showing a fully fabricated chip with 12 SIS junction.

first ALD SIS run is shown in Figure 3.14 with red circles highlighting the broken connections. The source of the high series resistance is still unknown. Due to these issues, a second set of devices were fabricated as shown in Figure 3.15. The yellow is the ground plane, white is the Nb wiring layer, and pink is SiO_2. The colors are what is naturally seen under the microscope. A zoomed image is shown in Figure 3.16, where the 3, 2, and 1 µm square junctions are visible underneath the Nb wiring trace.

The second set of junctions were measured very close to the day of the defense, so the data was included in the thesis after the defense. Out of the 12 junctions measured 4 were shorted, 6 junctions showed regular SIS behavior and 2 junctions showed strange behavior with Josephson tunneling at zero bias but shorting at higher voltages. Before moving on to the analysis, the lack of open junctions in the latest

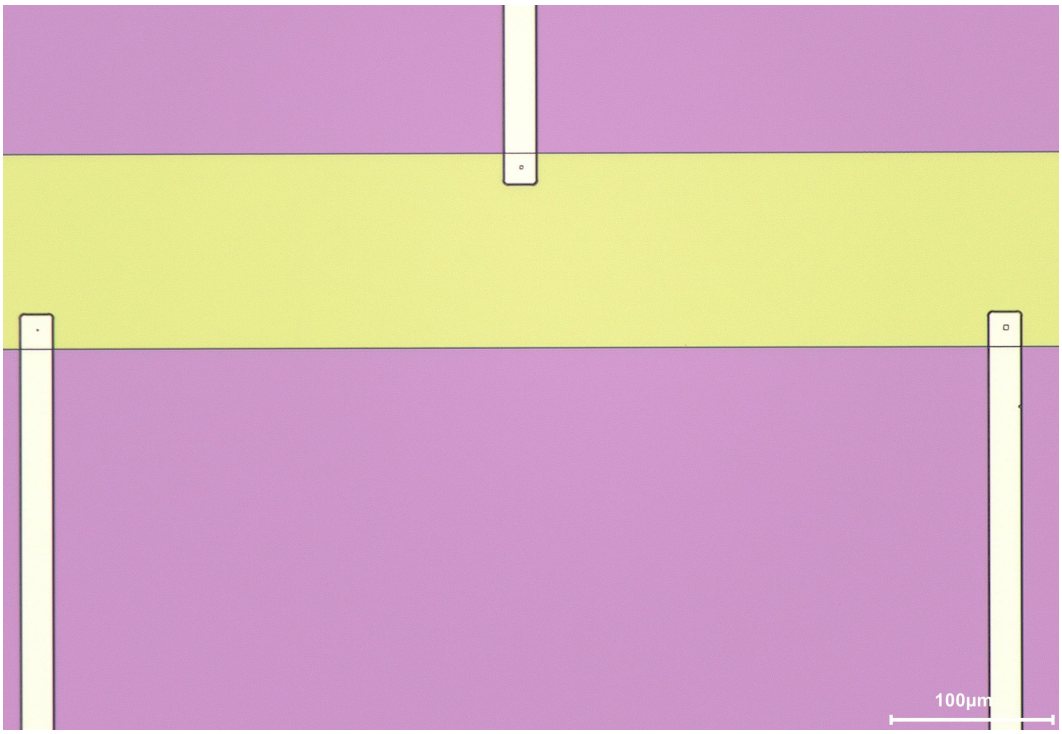

Figure 3.16: Optical microscope image showing the ground plane (yellow), junctions and the wiring to access the junctions on a fabricated chip.

set is exciting as it signifies that the final fabrication process is more robust with no breaks in the wiring. Both 500 and 250 nm junctions were shorted and both 750 nm junctions showed shorting at non-zero voltage. This would suggest that the barrier is too thin or transparent and unable to insulate the high current density for the sub-micron junctions. The 3, 2, and 1 µm junctions had SIS IV curves, with the 2 and 1 µm junctions exhibiting the best quality. The 3 µm junctions had a subgap ratio $\sim$ 1. The 2 µm junctions had subgap ratios of 9 and 10, and a $V_{gap} \sim 2.3$ mV. The 1 µm junctions had subgap ratios of 8 and 12, and a $V_{gap} \sim 2.0$ mV. The IV curves for one 2 µm and one 1 µm junction are shown in Figure 3.17. The IV curves show promising SIS behavior under zero magnetic field. However, the Josephson critical current is quite high compared to Ref. [184] and does not scale inversely with junction area as expected. Further, the critical current could not be fully suppressed in a magnetic field (measured upto 20 mT). The Josephson critical current was found to oscillate without being fully suppressed. Figure 3.18 shows the same junctions from Figure 3.17 with the external magnetic field set to minimize the Josephson critical current. Suppressing the Josephson current is necessary to obtain quantum-limited QP noise in SIS mixers, so the inability to suppress the Josephson

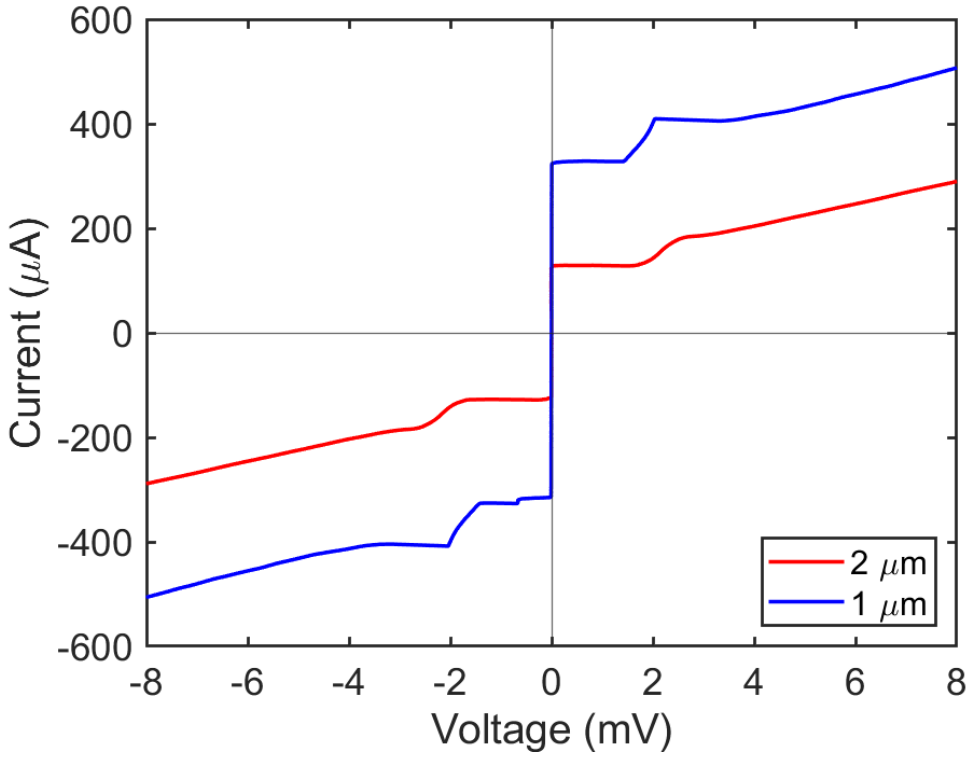

Figure 3.17: Current-voltage plot of 2 and 1 µm junctions from the second ALD NbN/AlN/NbN fabrication under no magnetic field.

current is a significant concern in these junctions. The strong Cooper-pair tunneling here would suggest that the barrier is in a parallel connection with either a short or some conductive regions. Such an effect may arise from pinholes or barrier thickness non-uniformity. We hypothesize this issue likely stems from the use of a thin AlN barrier (< 2 nm thick) in the junctions. To remedy this issue, a thicker (4 – 5 nm) and more insulating barrier like Al_2O_3 should be investigated in future work. The growth rate values for this run were calibrated on Si, but it is now understood that more accurate growth rate values are needed for such thin barriers. Therefore, the growth rate and film quality of the barrier on NbN needs to be studied between 10 – 50 cycles.

3.5 Conclusion

We have reported a plasma-thermal atomic layer etching process using sequential exposures of O_2 plasma and H_2/SF_6 plasma. O_2 plasma exposure yields a higher fraction of Nb_2O_5 compared to O_2 gas exposure, enabling subsequent volatilization by H_2/SF_6 plasma. The H_2/SF_6 plasma selectively etched Nb_2O_5 over NbN for

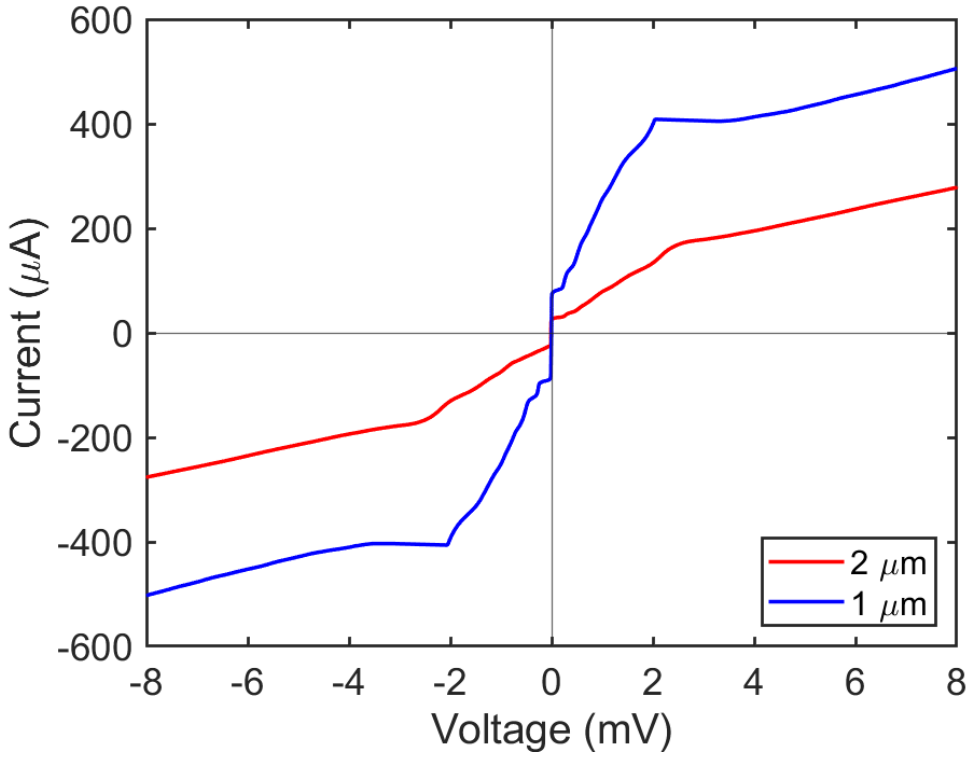

Figure 3.18: Current-voltage plot of the 2 and 1 µm junctions from Figure 3.17 with the magnetic field turned on and tuned to minimize the critical Josephson current at zero voltage.

suitable flow rate ratios. The etch rate was measured to be 1.77 Å/cycle at 125 °C. We observed a smoothing effect from ALE, corresponding to a 55% reduction in RMS roughness after 50 cycles, along with a 59% reduction in surface oxygen concentration. We also find that the T_c of an ALE-treated sample is higher than that of an RIE-treated sample of a similar thickness, highlighting the low-damage nature of the process.

We also report a plasma enhanced atomic layer deposition process using TBTDEN and H_2 plasma for growing superconducting NbN. We optimized the substrate temperature for growth and the plasma chemistry for maximizing T_c and minimizing resistivity. The best films were deposited at 400 °C with a H_2 plasma at a growth rate of 0.62 Å/cycle. The optimized films exhibited a T_c of 12.42 K, normal resistivity of 140$\mu\Omega$cm, and R_q = 0.26 nm. There is further room for optimization by varying precursor dose times, plasma times, and plasma power. The NbN ALD recipe was then used to fabricate SIS junctions with subgap ratio $\sim$ 10. Other important

characterizations that are planned for the future, are measuring the growth rate and dielectric constant of thin (1–4 nm) dielectrics such as AlN and Al_2O_3 on NbN.

We anticipate that the ability to engineer the surface of NbN films on the Angstrom-scale will facilitate applications of NbN in not just SIS mixers, but also for other superconducting quantum applications such as SNSPDs and MKIDs.

Chapter 4

NOVEL ETCHING CHEMISTRY FOR BORON AND MAGNESIUM DIBORIDE

4.1 Introduction

Magnesium diboride (MgB_2) is a metallic compound first identified in the 1950s. Its crystal structure is shown in Figure 4.1, which consists of hexagonal boron planes separated by magnesium atoms atop the center of each hexagon. However, superconductivity in MgB_2 is a more recent discovery. In 2001, bulk MgB_2 crystals were found to have a T_c of 39 K [137], the highest T_c of all phonon-mediated conventional (BCS) superconductors at atmospheric pressure. However, its T_c is quite close to the McMillan limit for BCS superconductors [124], which led some early papers to consider MgB_2 as an unconventional superconductor [16].

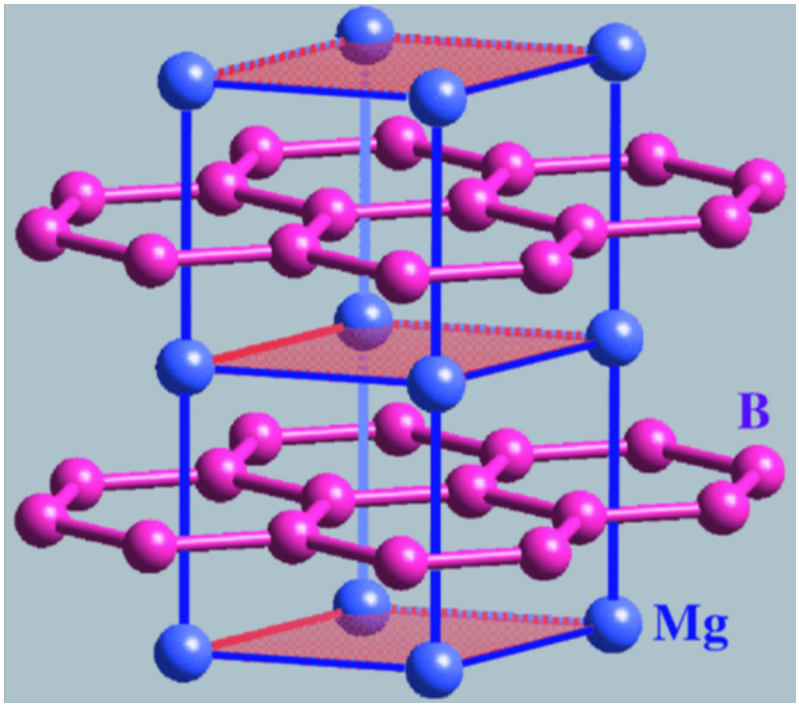

Figure 4.1: Crystal structure of MgB_2 showing hexagonal B layers in between Mg layers. The Mg atoms are located in the middle of the B planes. (Figure from Ref. [192]. Copyright Elsevier 2002)

MgB_2 was the first observation of multi-gap superconductivity, with a π-gap of

$\sim$ 2 meV and a σ-gap of $\sim$ 7 meV [16]. Afterward, it was shown that the π-band exhibited Type-I behavior and the σ-band exhibited Type-II behavior, which has led to MgB_2 being called a "Type-1.5" superconductor [133]. The presence of the two bands implied that the superconducting properties would fall somewhere between the BCS predictions for the individual bands. However, subsequent experiments indicated that the contribution of the two bands to the superconducting properties is dependent on the crystal structure of the film [158]. There is a "clean" limit where both gaps are distinct and the superconducting properties are dependent on the axis of excitation. At the other end there is a "dirty" limit where the superconducting properties are independent of the excitation direction, exhibiting properties that are the average of the two gaps. While the upper limit of the T_c is suppressed in the "dirty" limit, it allows for simpler device architectures where the film can be biased in any direction to access the superconducting properties.

The use of high T_c superconductors in superconducting electronics has many advantages such as higher operational temperature and lower cooling costs, higher frequency operation, and operation at higher magnetic fields ($H_c(0) \propto \Delta_0 \propto T_c$ from BCS). These effects should enable devices made from MgB_2 to be more resilient to external factors like thermal noise and stray radiation. Even though MgB_2 thin film thermodynamics and deposition methods have been studied extensively [16, 138], practical applications have yet to be mainstream due to the lack of wafer-scale films, poor reproducibility of films, and difficulty in film patterning. One of these issues has been successfully tackled by Microdevices Lab (MDL) at the Jet Propulsion Laboratory (JPL) [93], where they reported reproducible wafer-scale sputtering of MgB_2 with $T_c \sim 32$ K and low surface roughness of $R_q = 0.48$ nm. They also fabricated MgB_2 coplanar waveguides with internal quality factors $Q_i \sim 3 \cdot 10^4$ at 4.2 K [62]. These results show new promise for the use of MgB_2 in superconducting electronics.

The MgB_2 wafers from JPL warrant further discussion as they are used to test the etching chemistry and fabricate devices in Sections 4.2 and 4.4. The deposition is detailed in Ref. [93], and a brief overview is described here. The process starts with a 100 mm Si wafer with 30 nm low-stress PECVD SiN_x. Mg and B are then co-sputtered on top of the SiN_x to form 40 nm of MgB_2. After which, a 30 nm thick B cap is deposited to passivate the film when exposed to air. The B cap also acts as a crack-free, viscous capping layer when the sputtered film is annealed afterward in a nitrogen environment at ~400 °C. The completed stack is shown in Figure 4.2.

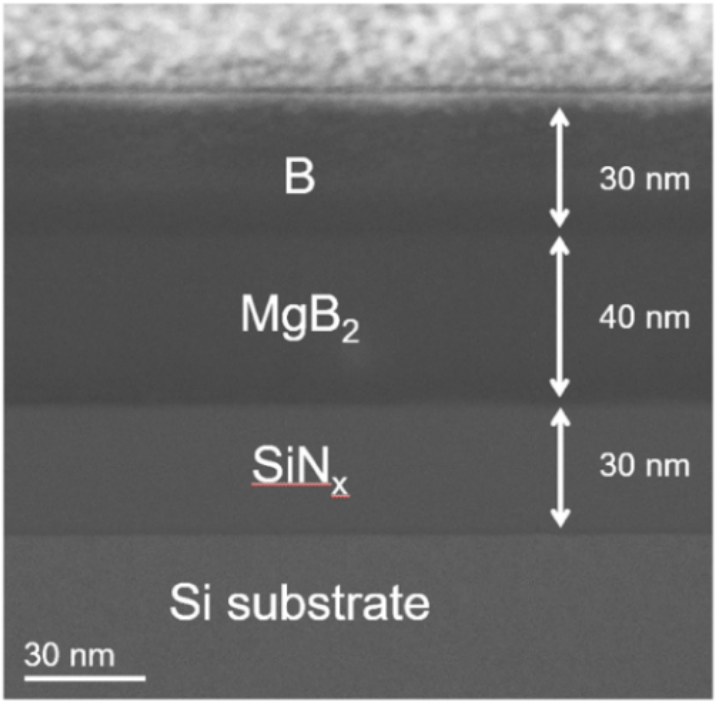

Figure 4.2: High-angle annular dark-field scanning tunneling electron microscope (HAADF-STEM) image of 40 nm thick superconducting MgB2 thin film with a 30 nm boron cap layer on a high-resistivity silicon wafer with a 30 nm silicon nitride buffer layer, showing sharp interfaces. (Reprinted from Ref. [93], Copyright American Chemical Society.)

Due to the nature of the film stack, device fabrication requires an extra etch step to remove the B cap to access the MgB_2 underneath. It is important that the etch to remove the B cap is chemical, with some selectivity to the MgB_2 underneath. A low-damage chemical etch is also important so that the MgB_2 surface is not damaged and surface roughness is not increased by the etch. An aggressive physical etch will result in degraded superconducting properties and increased surface roughness. This will in turn impact the performance of devices such as microresonators or SIS junctions, which are sensitive to interface and surface loss. The current etch method for removing the cap is either Ar milling which is entirely physical, or BCl_3 RIE which forms undesirable non-superconducting $MgCl_2$. To address these issues, a new etch chemistry is needed that can chemically etch off the B cap with low damage, maintain low surface roughness, and preserve the film T_c.

4.2 H_2 plasma etching of Boron and MgB_2

In this section we discuss a novel approach to etch the boron cap and the underlying MgB_2 using hydrogen plasma. First, we discuss current methods used in the etching of MgB_2. Magnesium salts such as oxides and fluorides have high stability and melting points, which is why oxygen and fluorine chemistry is avoided during MgB_2 etching. This means that common etching gases such as SF_6, NF_3, CF_4, and CF_2Cl_2 have to be avoided. Heavier halogens such as chlorine and bromine however, have been used to etch MgB_2 due to their increased magnesium halide ($Mg(Ha)_2$) vapor pressure compared to MgF_2 [169]. Figure 4.3 shows the vapor pressure versus temperature for different magnesium halides. It shows that the heavier halides still need temperatures around 400 °C to achieve etch rates, $R \sim 1$ Å/s. This value can be estimated using by calculating the maximum molecular flux (J) at 400 °C using the Hertz-Knudsen equation, and then plugging J into Equation (4.2) to obtain the theoretical maximum etch rate R. In Equations (4.1) and (4.2), M is the molar mass, N_A is avogadro's constant, P is pressure (Pa), R is the gas constant, ρ is the density of the film (kg/m^3), and T is temperature (K).

$$J = \frac{PN_A}{\sqrt{2\pi MRT}} \tag{4.1}$$

$$R = \frac{JM}{\rho N_A} 10^9 \ \text{(nm s}^{-1}\text{)} \tag{4.2}$$

However, etching is typically performed at lower temperatures (< 200 °C) using a plasma. Under these conditions most of the MgB_2 etching is dominated by physical etching, even though there may be a small chemical component. This explains why most of the MgB_2 etching in literature uses Ar or focused ion beam (FIB) milling to avoid the creation of magnesium halides that degrade superconducting performance [16, 138]. However, physical etching of MgB_2 also has its downsides, such as re-deposition of sputtered atoms which lead to increased sidewall and surface roughness. The use of high energy atoms in physical etching can cause micro-trenching near waveguides, and the embedding of other atoms such as Ar or Ga in the film structure can lead to local variations in superconducting properties [8, 170]. Cl_2 and BCl_3 plasma are routinely used at JPL to etch the B cap and underlying MgB_2 film [62]. However, post-processing has to be done to account for chlorine damage and diffusion into MgB_2. Etching is typically followed by quenching in a buffered oxide etch solution (HF-BOE). The quench is followed by milling to remove the surface $MgCl_2$ before a top electrode or some other layer can

be deposited on top of the MgB_2. To tackle these downsides, we investigated a new chemistry to etch the B cap and MgB_2 using hydrogen plasma.

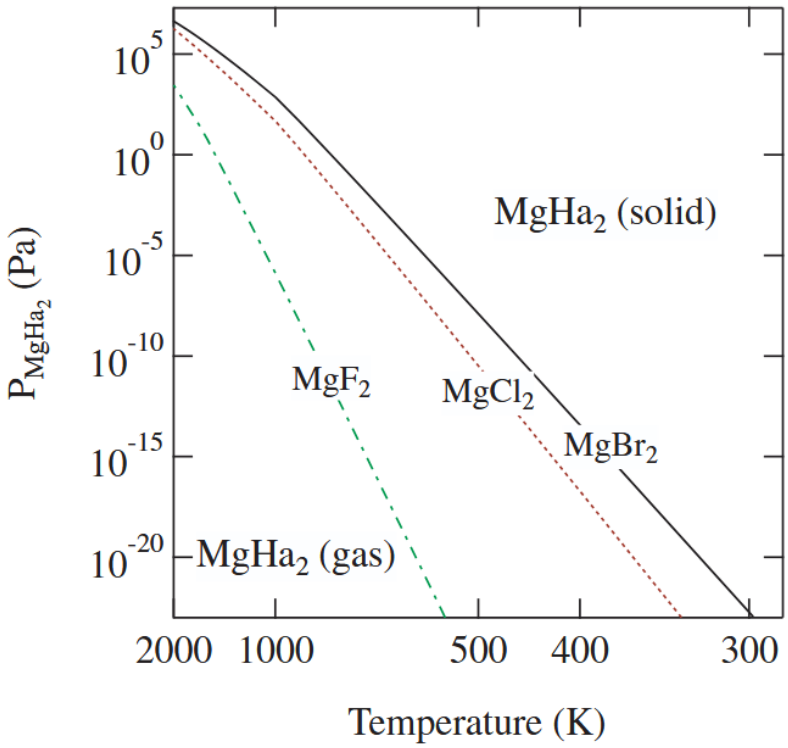

Figure 4.3: Calculated vapor pressure for magnesium halides, $Mg(Ha)_2$ versus temperature. Reprinted from Ref. [169], Copyright The Japan Society of Applied Physics

The motivation for etching MgB_2 using H_2 plasma is two-fold. The first motivation is that the etching could be entirely chemical as the reaction mechanism is predicted to follow Equation (4.3). The expected etch products are volatile BH_x compounds and MgH_2. MgH_2 is then known to decompose above 300 °C into H_2 gas and Mg. Mg is volatile at 300 °C with a partial pressure of 3 mPa [57, 164], which should result in a maximum etch rate of ~ 1 nms^{-1}.

$$MgB_2 + 4\,H_2 \rightarrow MgH_2 + B_2H_6 \tag{4.3}$$

The second motivation is the use of hydrogen plasma to chemically etch off the boron cap used. The boron cap is expected to etch rapidly by forming volatile BH_3 or B_2H_6, resulting in some etch selectivity with the underlying MgB_2. This would allow for a low-damage removal of the Boron cap to access the MgB_2 underneath,

as opposed to removal in a BCl_3 plasma which will result in the formation of non-volatile $MgCl_2$ [62].

Before moving on to the results, the methodology needs to be addressed. All measurements and experiments were carried out in the Kavli Nanoscience Institute (KNI), unless noted otherwise. Ellipsometry was performed *ex situ* on a J.A. Woolam M2000 ellipsometer. Evaporated films were deposited using an AJA International ATC Orion Series e-beam evaporator. Sputtered films were deposited using an AJA UHV Orion dielectric sputter system, named the dielectric sputter in the KNI. Dry etching was done on an Oxford Instruments Plasma Technology Plasmalab System 100 ICP-RIE 380 system, named the III-V etcher in the KNI. Surface morphology and step heights were characterized on a Bruker Dimension Icon atomic force microscope (AFM) using PeakForce Tapping mode. The raw height maps collected on the AFM were processed by removing tilt using the Bruker Analysis linear flatten function. Surface roughness and power spectral density (PSD) were calculated from plane-fit height maps using procedures outlined in the previous literature [19, 54]. Film composition was characterized using X-ray photoelectron spectroscopy (XPS) performed on a Kratos Axis Ultra X-ray photoelectron spectrometer using a monochro-matic Al Kα source at the Molecular Materials Resource Center (MMRC). Cryogenic electrical measurements were performed on a Quantum Design DynaCool Physical Property Measurement System (PPMS) at the Rosenbaum lab, and at JPL by Jonathan Greenfield, Daniel Cunnane, and Jacob Kooi. Oxygen ashing was performed on a Tergeo Plus Plasma Cleaner under the direct mode. Photolithography was carried out using a Suss Contact Mask Aligner MA6 using h-line (405 nm) exposures. E-beam lithography was carried out on a Raith EBPG 5000+.

Due to the lack of an ellipsometry model for MgB_2, thickness measurements have to be made physically by measuring the height of the stack to some standard. To accomplish this, the MgB_2 chips are hardmasked with Ti. The chips were dehydrated using an oxygen ash and then spun with S1813 photoresist. After exposure and development, the resist was coated with 25 nm of Ti. Liftoff was carried out in Remover PG to establish the hardmask. A blank Si chip was also put into the evaporator as the same time as the patterned chip to create a blank sister sample. This sister sample is inserted into the etcher together with the patterned MgB_2 chip. The change in thickness of the sister sample is measured using ellipsometry by fitting to a Lorentz model for Ti. This measurement allows for calibrations to the

change in thickness of the Ti hard mask. While Ti is etch resistant to hydrogen plasma, some physical etching is possible. Over all the etch runs, the Ti hard mask was found to etch between 0.5 – 1 nm over 30 minutes of plasma exposure. Before etching, the patterned sample was taken to the AFM to measure the step height. Step heights are measured over five random steps on the chip to generate standard deviation values. After etching, the same five steps are measured to calculate the etched thickness. This cycle of measurements is repeated across different etching parameters and chips.

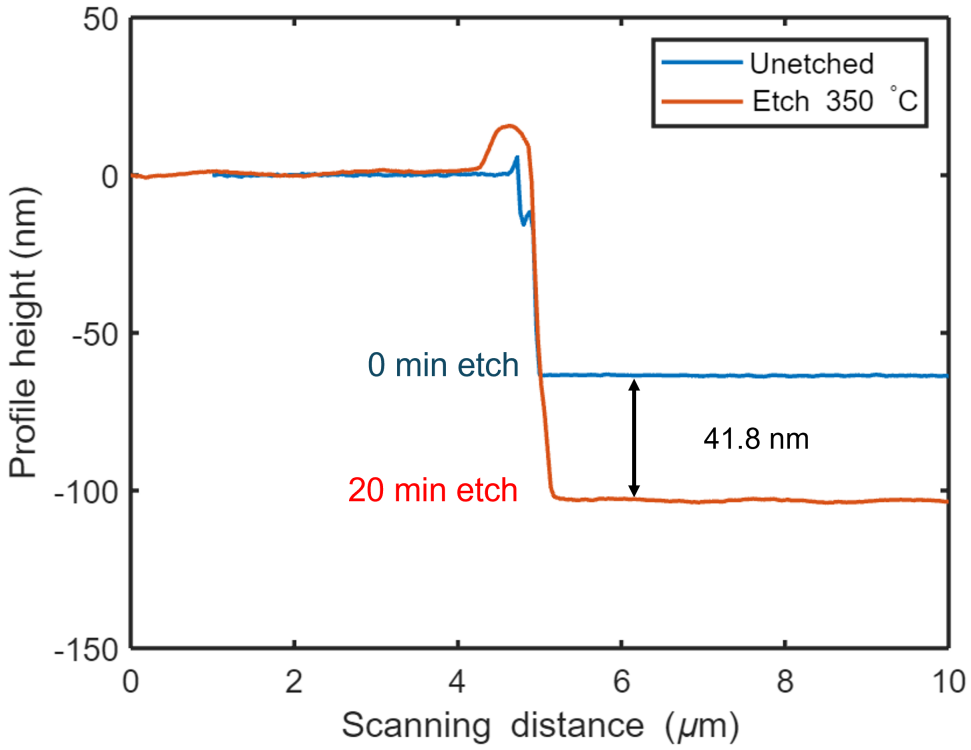

Figure 4.4: AFM scan showing the side profile of a step height before and after a 20 minute H_2 plasma etch at 350 °C.

H_2 plasma etching was first tested at 350 °C. A 50 sccm flow of H_2 was used to strike a plasma at 20 mTorr pressure with power settings of 1000 W ICP and 100 W bias. After 10 minutes of plasma exposure, a 25.64 ± 0.11 nm decrease in the step height was measured, corresponding to an etch rate of ~ 2.6 nm/min. After 10 more minutes of etching, a total step height change of 41.8 ± 0.59 nm was measured, as shown in Figure 4.4. The final step height now corresponds to etching 30 nm of B and 11.8 nm of MgB_2. These etched thicknesses would imply an MgB_2 etch rate of

$\sim$ 1.39 nm/min, and a B:MgB_2 selectivity of 1.85. This result is our first evidence of a successful new etch chemistry for MgB_2. However, there were concerns of etching at 350 °C, as the thermal budget of the standard MgB_2 device fabrication was 150 °C. This brings us to an important caveat of processing MgB_2, the degradation of its superconducting properties.

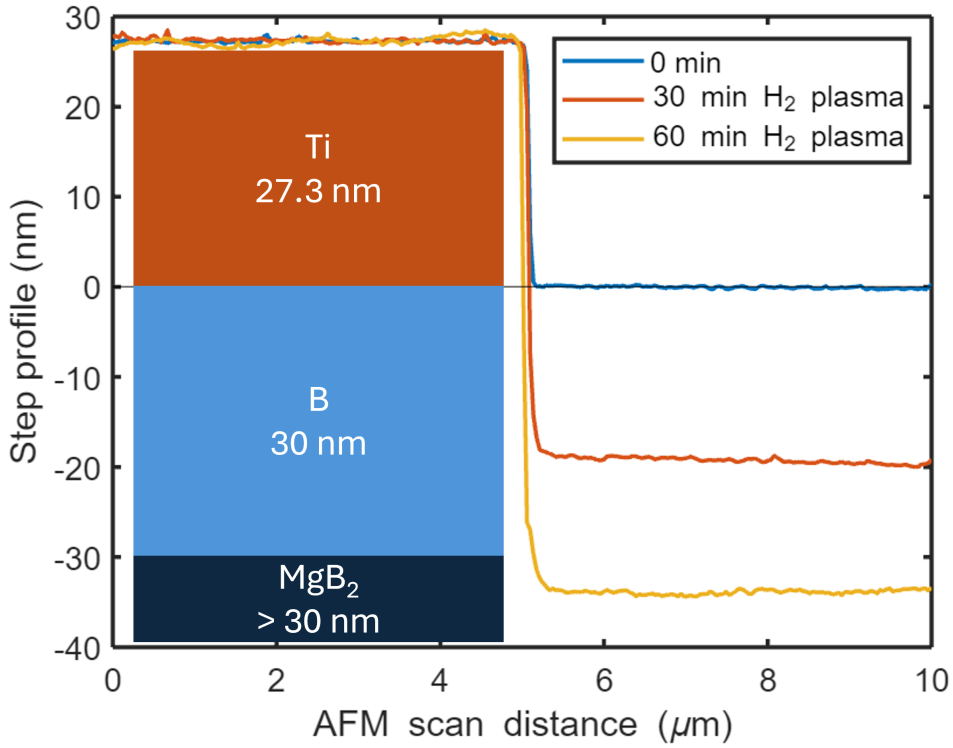

Figure 4.5: AFM scan showing the side profile of a step height before and after a 30 minutes and 60 minutes of H_2 plasma etching at 125 °C.

Multiple studies have demonstrated an increase in resistivity and change in the magnetic properties of unpassivated MgB_2 films upon prolonged exposure to water and ambient air [165, 195]. This is thought to be due to the unstable oxide/hydroxide formed by MgB_2 in air, which may not be self-limiting [92]. To understand the effect of the hydrogen plasma at 350 °C we also did XPS analysis of the 350 °C etched films. The results showed oxygen contamination at least 9 nm into the film and $\sim$ 40% oxygen concentration at the surface. The high oxygen contamination depth is thought to result from the increased diffusion length of oxygen at higher temperatures and from the base oxygen contamination in the etching chamber. To address these concerns two major changes were made before further testing was

done. First, the etching temperature was dropped to 125 °C. Second, before running the H_2 etch, an oxygen scrub pre-treatment was run in the chamber. The treatment consisted of three main steps.

1. H_2 plasma for 5 minutes at 100 mTorr, 125 °C using 80 sccm flow, 2000 W ICP and a 50 W bias. The hydrogen radicals are expected to react with oxygen and fluorine in the chamber.
2. 100 sccm Ar flow for 5 minutes at 100 mTorr. Similar to a kinetic bakeout, the atoms in the high energy tail of the boltzmann distribution are expected to knock off water from the chamber walls formed by the hydrogen plasma in the previous step, and help reduce the base pressure of the chamber.
3. Pump for 2 minutes
4. The process is repeated three times.

Under these new conditions, the etch was repeated at 125 °C at 20 mTorr with 80 sccm H_2 and plasma parameters of 1000 W ICP and 40 W bias. The bias was decreased to reduce physical sputtering and reduce surface roughening. The results are shown in Figure 4.5. Step height was measured after 30 minutes of etching, etched again for another 30 minutes and then measured once more. Based on the etch depth of 19.1 ± 0.62 nm after 30 minutes and 34.1 ± 0.55 nm after 60 minutes, the estimated etch rates are 0.64 nm/min and 0.31 nm/min for B and MgB_2 respectively. This would imply an etch selectivity of 2.1 between B and MgB_2. Etch rates at other plasma powers were also measured. The results are shown in Table 4.1, where the etch rate for B is listed, and the B:MgB_2 selectivity to MgB_2 is written wherever it was measured. The etch recipe using 1000 W ICP and 15 mTorr pressure was selected for more detailed study as it exhibited the highest selectivity at a reasonable etch rate. Surface morphology and chemistry results in the rest of the chapter are based on the recipe in bold in Table 4.1.

Surface roughness of H_2 etched MgB_2 films

Figure 4.6 shows AFM scans for the same MgB_2 before etching, after 30 minutes of etching (almost through the B cap), and after 50 minutes of etching (through the B cap and slightly etched into the MgB_2). The AFM scans shown are 500 nm × 500 nm. The original film had R_q ~0.34 nm. After 30 minutes of etching most of the B cap is removed and the top surface is expected to be near the B–Mgb_2 interface.

Table 4.1: Measured etch rate of the B cap under various H_2 plasma parameters.

Temperature (°C)	ICP power (W)	Pressure (mTorr)	B etch rate (nm/min)	B:MgB_2 selectivity
350	1000	20	2.6	1.85
125	1000	20	.64	2.06
125	2000	10	1.50	–
125	1000	10	1.20	–
125	**1000**	**15**	**0.95**	**2.15**
125	800	15	0.67	–

At this interface the RMS roughness increased to 0.39 nm from the etching. After another 20 minutes of etching, the MgB_2 had been exposed and we had etched ~ 8 nm into the MgB_2. At this point the surface roughness was measured to be 0.38 nm. Larger scans over a 2 µm × 2 µm area measured higher R_q values of 0.41 and 0.45 nm after 30 and 50 minutes of etching respectively. These measurements show an increase in the surface roughness after etching, however, the roughness is still low ~ 0.5 nm, which is suitable for junction fabrication.

Passivation effect of magnesium hydride

We then measured the cryogenic resistivity of the etched samples as a function of temperature, to investigate how the H_2 plasma etching would affect the T_c of the underlying film. The results are shown in Figure 4.7. The original film has a sheet resistance of $R_s^{50\,\mathrm{K}} = 39.4\ \Omega/\square$ and $T_c = 28.6 \pm 0.2$ K. After etching 8 nm into MgB_2, the sheet resistance increased to $R_s^{50\,\mathrm{K}} = 49.1\ \Omega/\square$, which is consistent with a 20% decrease in the MgB_2 thickness. The T_c of the etched film was found to be 28.3 ± 0.6 K, which is a $< 2\%$ decrease from the original film. However, the transition width increased threefold. The etched sample was then stored in ambient conditions for 2 months (63 days), after which it was measured again. The sheet resistance was found to be slightly higher at $R_s^{50\,\mathrm{K}} = 49.7\ \Omega/\square$, and T_c was found to be 28.3 ± 0.6 K. These results indicate that the change in T_c and sheet resistance upon etching with H_2 plasma is consistent with the change in thickness. However, the large increase in the transition width is yet to be understood. Surprisingly, we also found that the H_2 etching left the film with some hydride barrier capable of preserving T_c and R_s for at least 2 months.

To understand the source of the passivation, depth-profile XPS was performed. Since hydrogen cannot be measured on XPS, a proxy was used. We looked at the change in

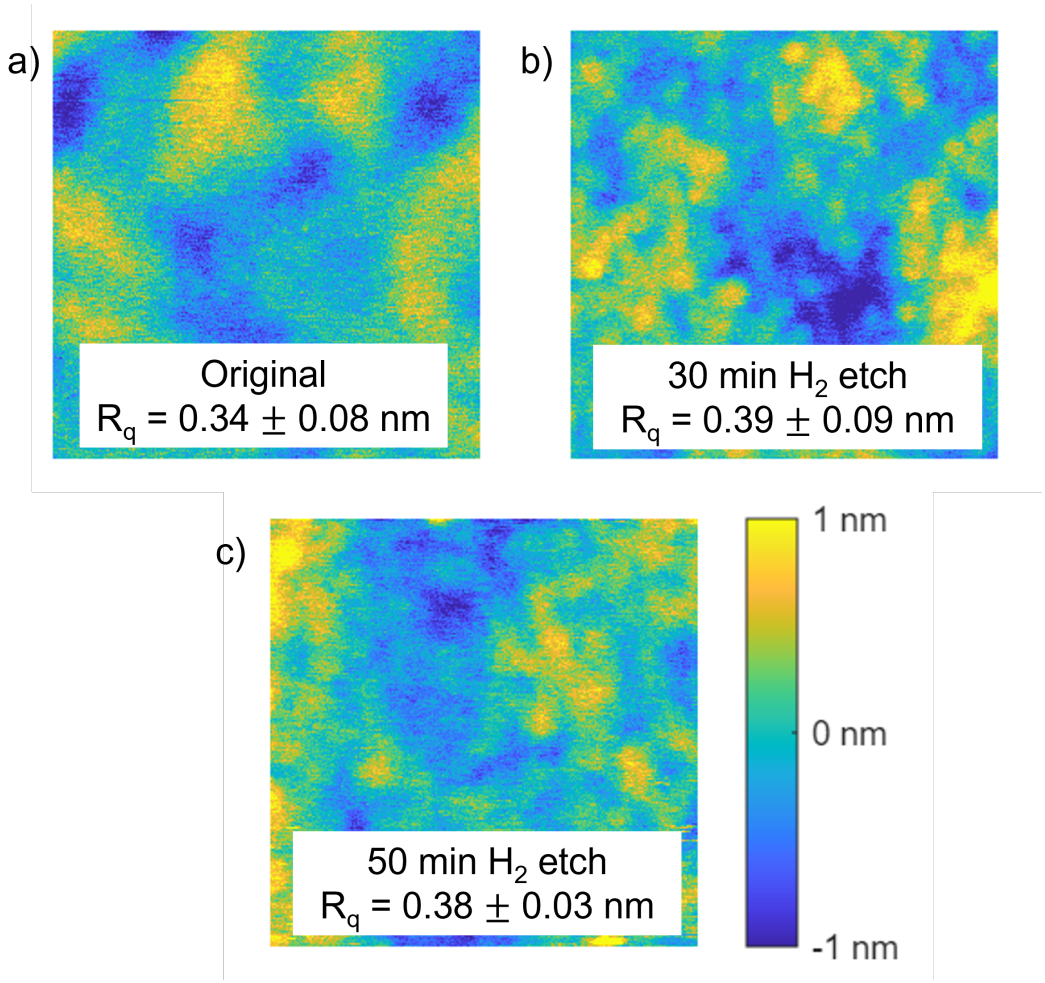

Figure 4.6: AFM scans showing height-maps of (a) original MgB_2 sample, (b) after 30 minutes of H_2 etching, and (c) after 60 minutes of H_2 etching.

B:Mg ratio versus milling depth to examine how thick of an interface was left behind by the H_2 plasma. The results are shown in Figure 4.8. The B:Mg ratio was found to increase above 2 between 5 – 7 nm. These results indicate that the hydrogen plasma left behind a ~ 6 nm thick hydride interface. The high oxygen concentration (22%) at the surface implies that the surface is not just a hydride but likely a hydroxide. We hypothesized that the hydroxide is created upon exposure to air and water vapor, and is not an inherent quality of the hydrogen plasma etching. Based on the passivation effect of the magnesium hydride, we were interested infabricating an SIS junction using the hydride as the tunneling barrier. The results of using a hydride barrier are discussed in Section 4.4.

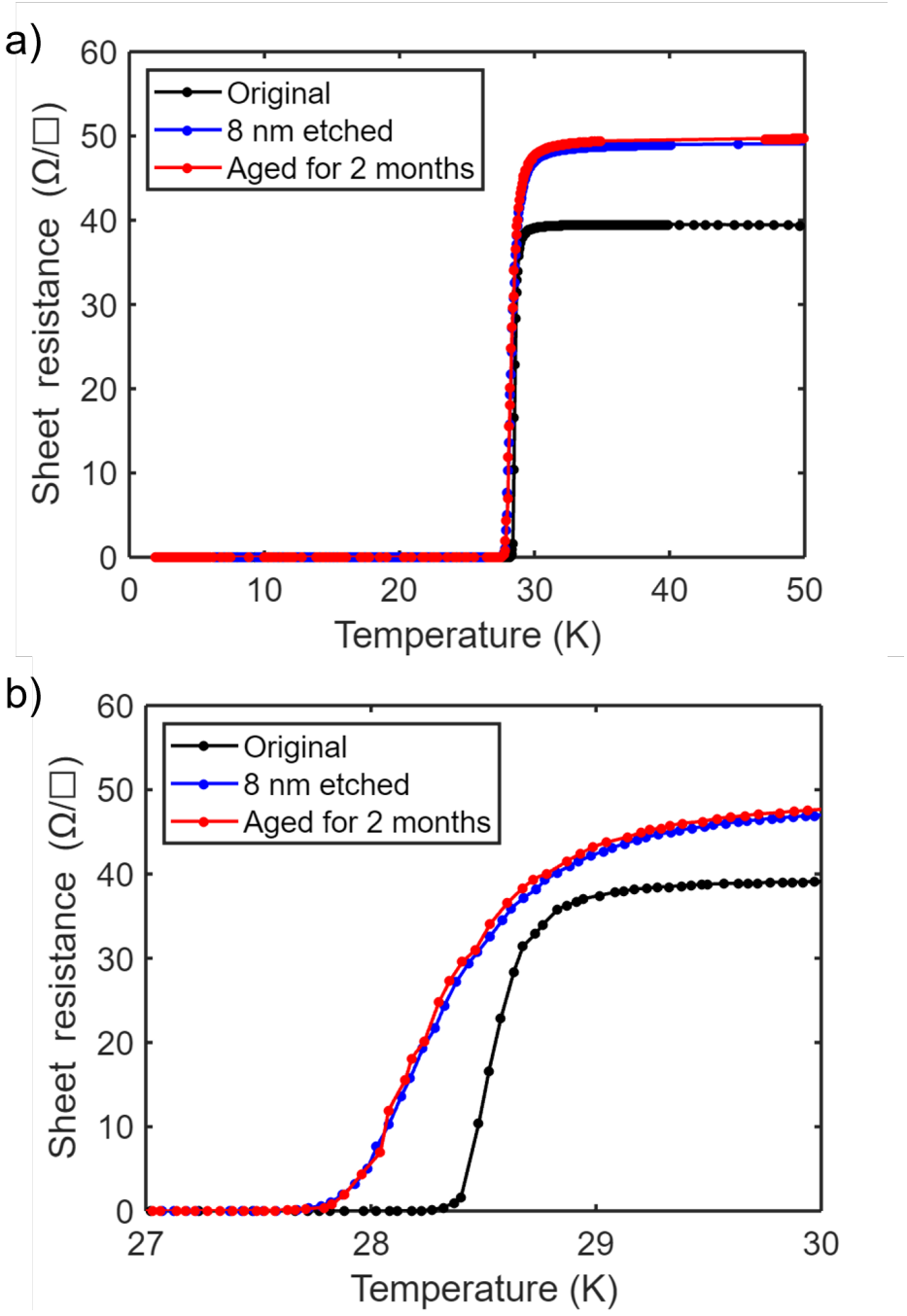

Figure 4.7: a) Sheet resistance versus temperature curves for an unetched MgB_2 film, an etched MgB_2 film measured the same day, same etched film measured after 2 months. b) Same plot as a) but with a truncated x-axis to better show the superconducting transition.

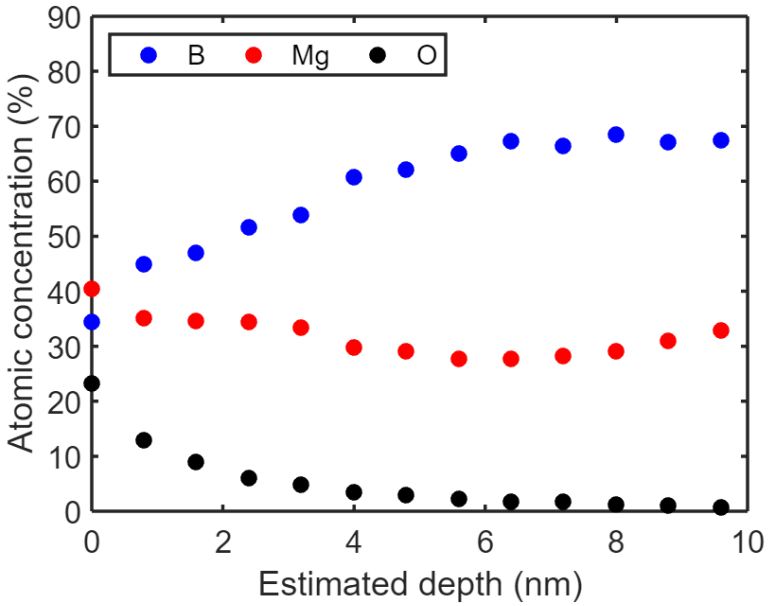

Figure 4.8: Atomic concentration versus estimated milled depth showing the concentration of boron (blue), magnesium (red), and oxygen (black) species.

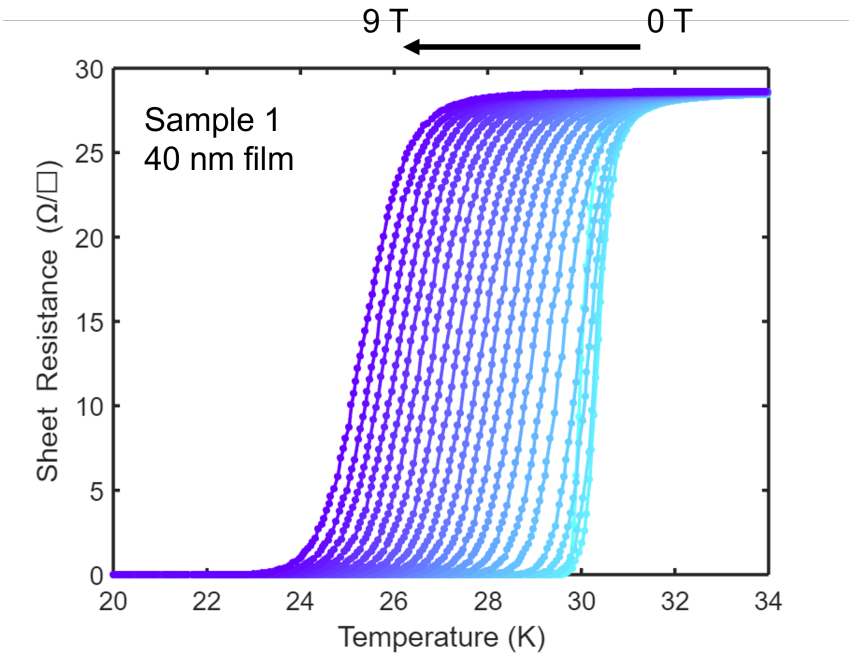

Figure 4.9: Sheet resistance versus temperature data for sample 1, which is the standard 40 nm film used in device fabrication, taken at varying magnetic fields from 0 to 9 T. The lines are guides to the eye.

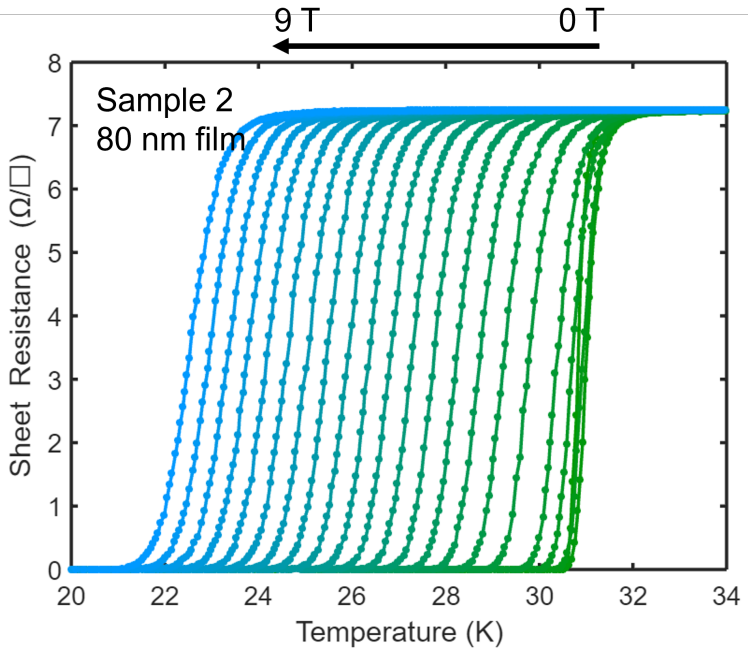

Figure 4.10: Sheet resistance versus temperature data taken at varying magnetic fields from 0 to 9 T for sample 2 which is 80 nm thick. The lines are guides to the eye.

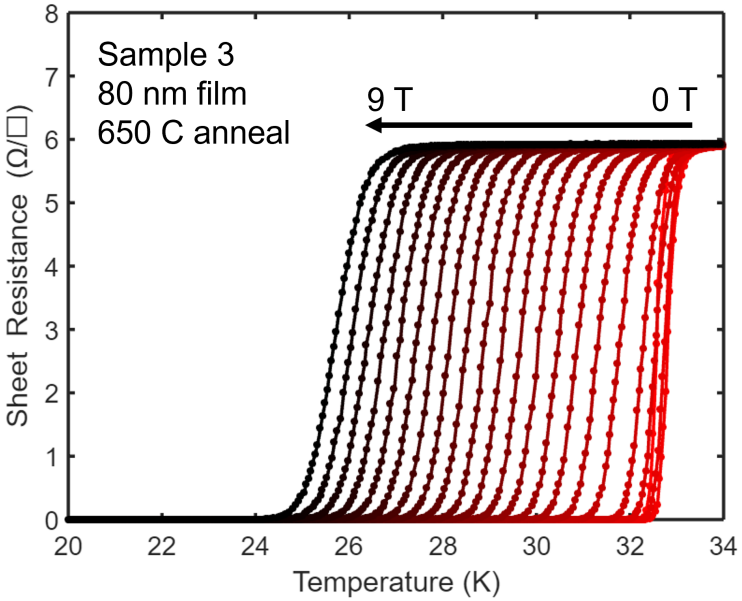

Figure 4.11: Sheet resistance versus temperature data taken at varying magnetic fields from 0 to 9 T for sample 3 which is 80 nm thick and annealed at 650 °C. The lines are guides to the eye.

4.3 Measuring the coherence length of MgB_2

The coherence length of the JPL MgB_2 wafers are characterized in this section. A crucial parameter for designing SIS junctions is the coherence length (ξ) of the superconductor used. The coherence length sets the length-scale across which the superconducting wavefunction extends outside the material. Since an SIS junction is based on the tunneling of QPs from one electrode to the other, there has to be some overlap of the two superconducting wavefunctions. This would imply that the junction barrier thickness should be at most the coherence length of the superconductor, otherwise the tunneling current will be suppressed. One way to measure the coherence length of a superconductor is measuring its critical field. Since MgB_2 has type-II characteristics, it has both an upper and lower critical field. The coherence length is related to the upper critical field (H_{c2}) by GL theory. The expression is shown in Equation (4.4), where the coherence length and upper critical field are measured at 0 K.

$$\xi_0 = \sqrt{\frac{\hbar}{2e}\frac{1}{\mu_0 H_{c2,0}}} \tag{4.4}$$

While Equation (4.4) is relevant, it is impossible to measure the upper critical field at 0 K. Here we turn to temperature dependent models which describe the behavior of the field-temperature phase transition curve at finite temperature. Unlike Type-I superconductors, there is no universal model for the temperature-dependent upper critical field $H_{c2}(T)$. One promising model is the Werthamer–Helfand–Hohenberg (WHH) model for dirty-limit type-II superconductors, commonly used for high T_c superconductors [90, 188]. The relevant equation from WHH model is given in Equation (4.5), where we use $B_{c2} = \mu_0 H_{c2}$.

$$B_{c2,0} = 0.69\, T_c \cdot \left(\frac{dB_{c2}}{dT}\right)_{T_c} \tag{4.5}$$

However, the modeling for MgB_2 is further complicated by the fact that it is not a type-I superconductor. It mostly exhibits type-II behavior, but it is also not a typical type-II superconductor, and a modified two-band theory is required for accurate modeling of the field-temperature phase diagram [65, 141]. In this work we will use Equation (4.5) which has been shown to lead to an underestimate of $B_{c2,0}$ for MgB_2 [65]. An underestimate of the upper critical field will then result in an upper bound for the coherence length.

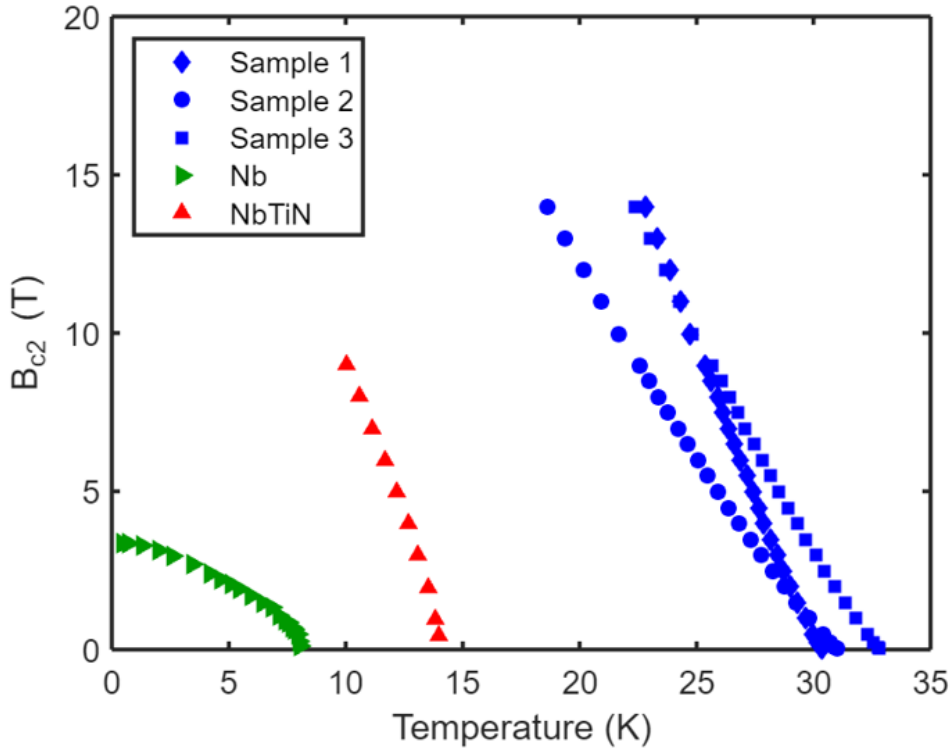

Figure 4.12: B_{c2} versus temperature shown for MgB_2 Samples 1, 2 and 3 (blue squares, diamonds and circles), Nb[194] (red triangles) and NbTiN[104] (green triangles).

The field versus temperature curves for three different MgB_2 samples are shown in Figures 4.9 to 4.11. The different samples were made by Jonathan Greenfield (JPL). Sample 1 is the standard film used in device fabrication in Section 4.4. Sample 2 is 80 nm thick and annealed at the same temperature as sample 1, and sample 3 is 80 nm thick and annealed at 650 °C. T_c was measured at varying magnetic fields from 0 to 14 T, to calculate $B_{c2,0}$. Different films were measured to investigate the ability to tune the coherence length by varying deposition parameters. The axes for all three figures are kept constant to make comparisons easier. Before looking at the field-T_c plot, it can be observed that samples 2 and 3 experience a larger drop in T_c than sample 1 when magnetic field is increased. Qualitatively it is also visible that the transition width increases with increasing magnetic field.

The data from the sheet resistance versus temperature curves has been summarized in Figure 4.12, showing the upper critical magnetic field versus the critical transition temperature. The upper critical field B_{c2} values were calculated by fixing the magnetic field and measuring the temperature at which the superconducting transition

Table 4.2: Superconducting parameters of MgB_2 samples 1–3, Nb and NbTiN

	T_c (K)	$B_{c2,0}$ (T)	ξ_0 (nm)
Sample 1	30.4 ± 0.19	39.2	2.9
Sample 2	31.1 ± 0.15	24.4	3.7
Sample 3	32.8 ± 0.12	30.1	3.3
Nb[194]	7.6	2.64	11.2
NbTiN[104]	13.8	22.0	3.9

occurred. Figure 4.12 also shows the field-temperature phase boundary for Nb and NbTiN thin films. The figure shows the existence of a new region of phase-space accessible to devices based on MgB_2, which can access temperatures between 15 and 30 K, while simultaneously operating in fields up to 14 T (depending on the temperature). The blue curves in Figure 4.12 were used to calculate $B_{c2,0}$ using Equation (4.5), and finally ξ using Equation (4.4). The calculated quantities are listed in Section 4.3 along with the T_c, $B_{c2,0}$ and ξ_0 for Nb and NbTiN. The table shows that the standard sample has the highest upper critical temperature of almost 40 T at zero temperature, and the lowest coherence length of 2.9 nm. The 400 °C annealed 80 nm sample has the lowest upper critical field of ~ 24 T and the highest zero temperature coherence length of 3.7 nm. This data would suggest that thicker MgB_2 annealed at lower temperatures would be ideal for enhancing the coherence length, which is optimal for fabricating SIS junctions.

4.4 MgB_2 SIS junction fabrication

The Minnich lab from Caltech worked with Daniel Cunnane, Jacob Kooi and Clifford Frez from JPL as part of a collaborative effort to make SIS junctions for THz mixers using MgB_2 as the ground plane (bottom electrode). C. Frez fabricated the junction devices, which were characterized by D. Cunnane and J. Kooi. Both groups fabricated MgB_2/Nb hybrid junctions with different barriers. JPL fabricated and tested multiple devices with three different barriers: MgB_2 native oxide $MgBO_x$, aluminum nitride, and aluminum oxide barriers. At Caltech, we made junctions using the hydride barrier left behind by the removal of the B cap using H_2 plasma, as discussed Section 4.2. The main difference between the two efforts was that JPL used a Cl_2/BCl_3 plasma or Ar milling to remove the B cap and sputtered Al based barriers, whereas we used H_2 plasma to remove the B cap and used the hydride passivation left behind by the H_2 plasma as the junction barrier.

A summary of the results of the JPL work is provided here to contextualize the H_2 plasma etching. In their fabrication process, the B cap is removed with physical etching, either Cl_2/BCl_3 RIE or Ar milling. The wafer is then walked from the etcher to the sputtering tool which (takes a few minutes) and results in growth of a native oxide. The oxide is then sputtered off *in situ* prior to depositing the Al-based barrier and subsequently the top electrode. Only about 8% of 225 measured junctions fabricated at JPL over multiple runs were measured to have SIS characteristics. Most of the measured junctions turned out to be superconductor-insulator-normal metal (SIN) junctions, where we assume that the MgB_2 is exhibiting metallic properties instead. An example of the measured SIN curves are shown in Figure 4.13. The hypothesized root cause is difficulty depositing a good barrier on the MgB_2 interface, either due to damage caused to MgB_2 during B cap removal, *in situ* ion milling prior to Nb deposition, or due to pinholes in the barrier caused by Nb deposition. These potential issues are thought to be too damaging to the MgB_2 underneath, resulting in washed out SIS junctions or SIN junctions. These issues make the H_2 plasma for B cap removal even more appealing.

We will now focus on the Nb/MgB_2 hybrid junction fabrication process at Caltech. The full fabrication process can be broken into a few main steps. The first step is to build the trilayer. This involves removing the B cap with H_2 plasma, treating the hydride, and depositing Nb for the top electrode. The next key step is a mesa etch to remove metal from all parts of the wafer except regions of interest, to prevent shorting or stray fields. The next step is to define the junction areas and insulate the junctions from each other, as well as to insulate the wiring layer from the bottom electrode with an interlayer dielectric (ILD) or interconnect insulator. The final step is to deposit the wiring Nb to connect the top of the junction to the bonding pads. The final expected trace is shown in Figure 4.14. The red areas are connected to the bottom electrode and the blue areas are connected to the top electrode.

Trilayer definition

The first step started with MgB_2 on low-stress SiN_x wafers prepared similar to Ref. [62]. The wafers were then scribed into quarters, and all the masks and process parameters are optimized for dealing with quarter wafers. To quickly recall, the wafers are coated with a B cap for the annealing step. This brings us to the first step of the trilayer fabrication: etching the boron cap. The B cap was etched following the results in Section 4.2, with a 1000 W ICP and 30 W RF bias H_2 plasma at 15 mTorr and 125 °C. The 35 minute etch is expected to etch 30 nm of B with 1–2 nm

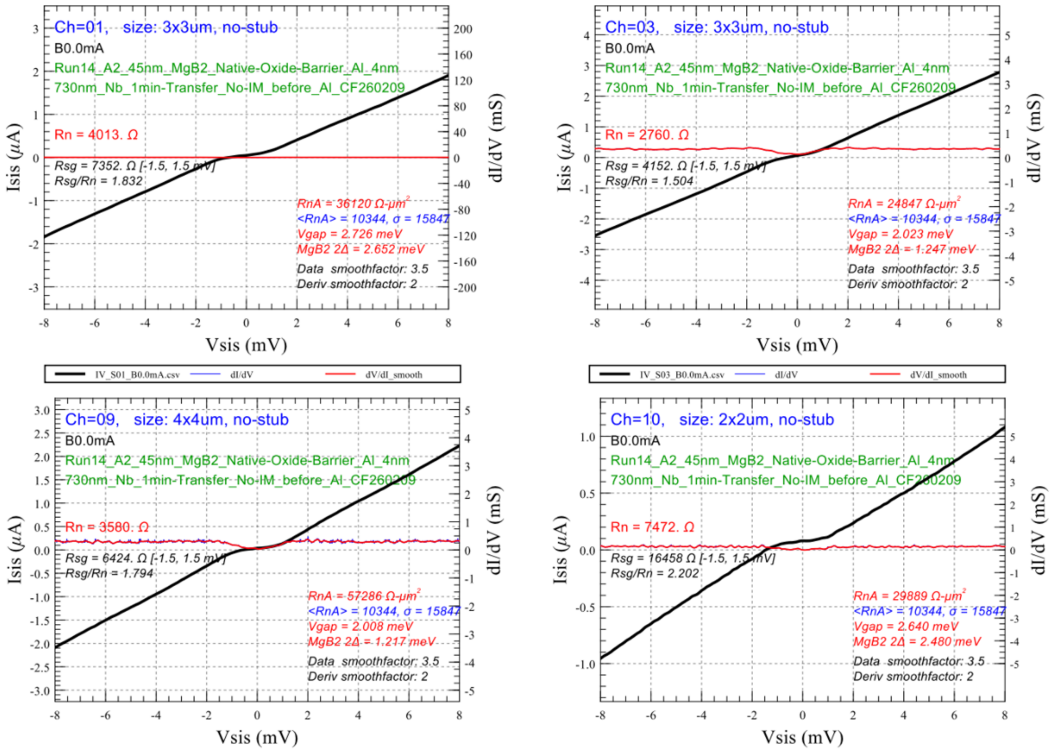

Figure 4.13: Current-voltage data for multiple junctions fabricated at JPL, showing superconductor-insulator-metal behavior. No Josephson current is measured at 0 voltage, and the non-linearity is suppressed. The black curves show the current-voltage data and the red lines show the differential conductance.

of overetch into MgB_2. The overetch is intentional to ensure the B cap is removed over the entire wafer. After the etch, the MgB_2 is left with a protective hydride barrier, the exact stoichiometry of this barrier is unknown, but expected to be of the form $MgBH_x$ (where x = 2 or 3) or $Mg(BH_4)_2$ [29, 157]. In reality the stoichiometry is likely some combination of these possibilities. This protective layer will be used as the barrier for the junction.

The next step is depositing niobium for the top electrode. An initial test run showed that directly depositing Nb on the hydrogen treated MgB_2 would result in delamination of the Nb as shown in Figure 4.15, likely due to water vapor trapped in the hydrogenated barrier.

To solve this issue, a heating step was implemented where the hydrogenated MgB_2 was heated to 120 °C in the sputter tool along with two minutes of Ar milling. The milling was done at 3 mTorr using a 40 W bias, which was found to etch at $\sim$ 1 nm/min. The heating was intended to drive off the trapped water, and the milling was used to thin the barrier which was 6 – 7 nm, as shown in Section 4.2. After

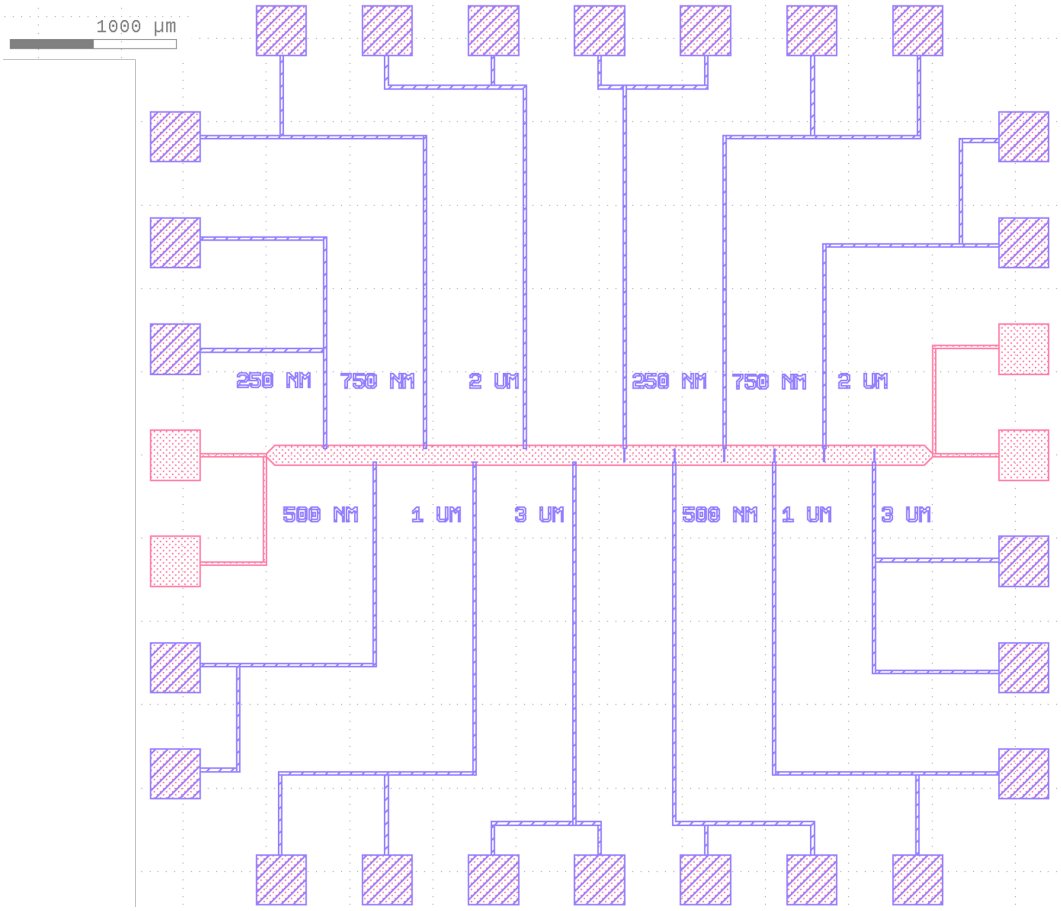

Figure 4.14: Schematic showing the expected top-down view of the final chip. The labeling is used to identify the size of the junction the wiring is connected to.

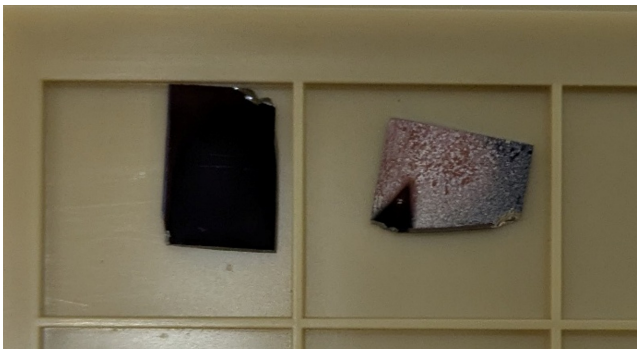

Figure 4.15: Image showing an MgB_2 chip before Nb deposition (left) and after Nb deposition (right) on a test run without any treatment before Nb sputtering.

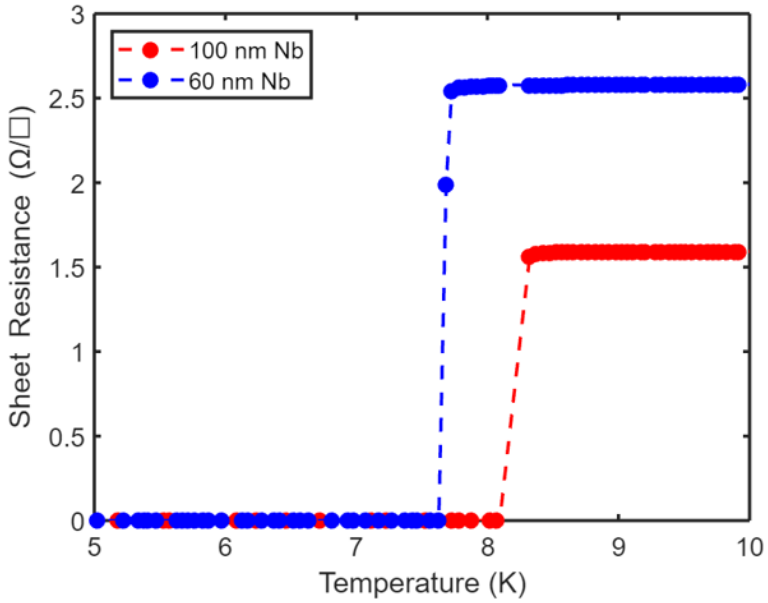

Figure 4.16: Sheet resistance versus temperature data for a 60 nm thick Nb film and a 100 nm Nb film. Lines are guides to the eye.

milling, the Nb was sputtered at 3 mTorr, 130 W DC power and 30 W bias. This deposition recipe was found to grow Nb at a rate of ~ 0.6 Ås^{-1} using AFM. A 17 minute deposition is expected to deposit a $\sim$ 60 nm thick film. Sheet resistance versus temperature data for a 60 nm and 100 nm Nb film grown on SiO_2 on Si samples using the parameters listed above is shown in Figure 4.16. The 60 nm thick Nb film exhibited a T_c of 7.67 ± 0.04 K with a sheet resistance of 4.72 Ω/□ at 300 K and a residual resistivity ratio (RRR) of 1.83. The 100 nm thick Nb film exhibited a T_c of 8.21 ± 0.09 K with a sheet resistance of 3.95 Ω/□ at 300 K and a residual resistivity ratio (RRR) of 2.48. The 100 nm film was deposited to examine the behavior of the wiring layer which at the time was expected to be 150 nm or thicker. The 60 nm Nb deposition concluded the trilayer building. The trilayer fabrication steps are summarized in Figure 4.17.

Mesa Etch

The mesa etch is important to etch away metal from all parts of the wafer that are unnecessary for the final device. In this step the bonding pads are defined, and the bottom electrode ground plane is defined. The MgB_2 ground plane is defined such that it only connects to four bonding pads, and the rest are to connect to the Nb top electrode. Prior to the mesa etch, alignment markers need to be deposited to align all the subsequent layers to each other. Different alignment marker geometries

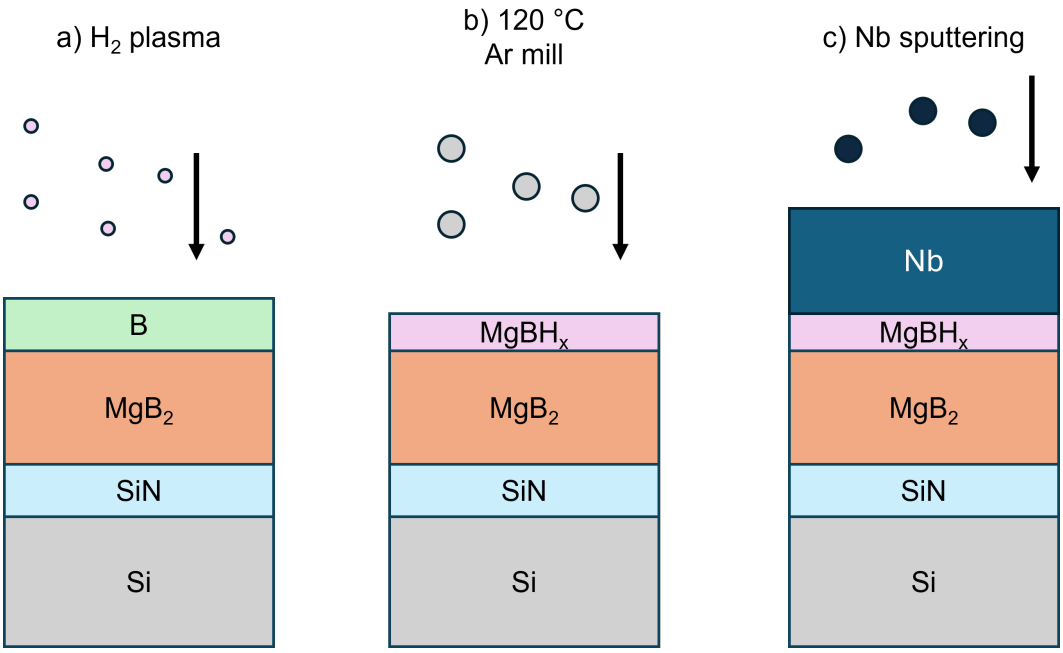

Figure 4.17: Schematic showing the trilayer fabrication steps. a) H_2 etching of the B cap. b) Ar milling and heating to treat the hydride barrier. c) Depositing Nb for the top electrode.

also need to be deposited in this step as photolithography and e-beam lithography use different shaped markers. The alignment layer definition started with spinning S1805 photoresist, followed by a softbake. The resist is then exposed in the Suss 2 in the KNI and developed in MF-319. The wafer is then taken to the e-beam evaporater to deposit 10 nm Ti at a rate of 0.5 Å/s, followed by 100 nm Au at a rate of 1 Å/s. The pattern is then defined by the liftoff in Remover PG at 80 °C. Higher temperatures were found to result in faster and easier liftoff. Following liftoff, the wafer is cleaned in an oxygen ash for 1 minute before moving on to the mesa etch.

In the mesa etch, the Nb was first etched using a 4 minute SF_6 RIE. The MgB_2 etching chemistry had to be worked out over time. Initial attempts used a Cl_2/Ar plasma. However, this resulted in delamination of smaller features due to lateral etching from the use of chlorine. These features and the delamination are shown in Figure 4.18. Chlorine is known to react with water vapor and form HCl, leading to lateral metal etching. The features were not immediately noticed under the microscope, but they likely became larger a day later when they were noticed. The lateral etching features are sometimes called 'mouse bites'. H_2 plasma etching was not used as it would be incompatible with standard photoresists. While certain e-beam resists have been shown to resist etching in H_2 plasma [22], e-beam was not a viable option in this

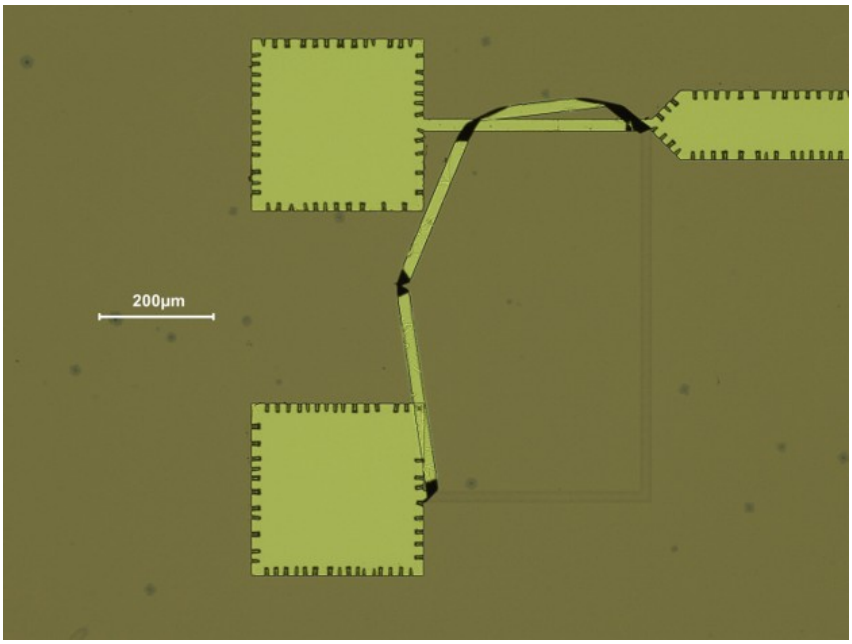

Figure 4.18: Optical microscope image showing the "mouse bites" caused by lateral etching from the use of a Cl_2/Ar plasma.

step due to practical constraints. Ar milling was finally chosen as it would be the fastest way to etch away 40 nm of MgB_2, while being compatible with standard photoresists.

However, photoresists like S1813 were still milled away and burnt by Ar milling and a thicker resist designed for dry etching like AZ-10XT was used. AZ10XT was spun at 5000 rpm and developed in 1:4 AZ400K:DI water, which resulted in a 8 µm thick resist. An important note for using AZ10XT is that it requires a 30 minute – 1 hour hydrating period after the softbake. Skipping this step can result in cracking or inconsistent development times. The final ICP Ar milling parameters were 100 W ICP and 150 W bias power at 10 mTorr and 10 °C. The parameters were chosen to maximize etch rate while minimizing resist burn. However, resist burn was soon found to be unavoidable. In order to reduce resist burn to a point where the resist could still be stripped afterwards, three additional changes were made.

1. A BN thermal paste was used to allow for better heat transfer from the chip to the carrier wafer. The paste can also be removed in IPA allowing for easier cleaning

2. The ICP Ar mill step was broken into cycles of 5 minutes each, stopping the plasma for 30 seconds in between to allow for the resist to cool

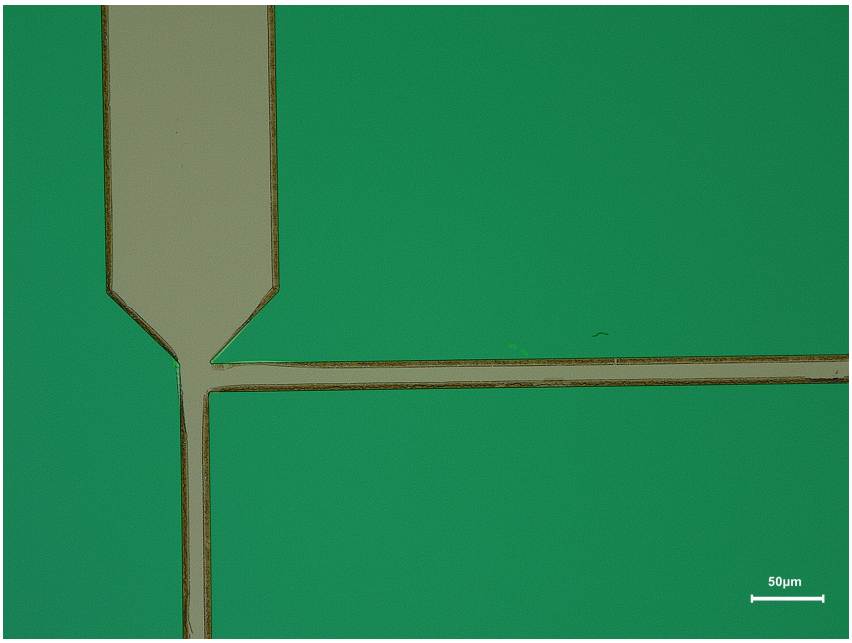

Figure 4.19: Optical microscope image showing the resist burn along the edge of features.

3. An aggressive oxygen ash was performed at 2000 W ICP and 30 W bias power, at 30 mTorr and 30 °C after the mill. The ash was done in the III-V for 5–10 minutes depending on the level of resist burn.

The ashing parameters were chosen to increase the isotropy of the ash in order to more effectively remove the burnt resist along the edges and corners where the plasma is strongest. It was also found that ashing to remove the burnt resist prior to stripping in Remover PG was essential as the burnt resist would harden in the solvent and became essentially impossible to remove. Figure 4.19 shows an image of leftover hardened resist along the edge of features. The burnt resist was not fully ashed off with a 3 minute oxygen plasma prior to stripping in solvent, causing the resist to harden and remain. After increasing the ashing time to 10 minutes, no such hardened resist features were observed.

Junction definition and interlayer dielectric

After defining the bottom electrode ground plane and contact pads, we move on to etch away the top electrode from everywhere except the junctions. The junctions were designed to be squares of lateral sizes µm, 2 µm, 1 µm, 750 nm, 500 nm, and 250 nm. Smaller junctions are more desirable when pinholes could be present, as the stochastic nature of pinholes would imply an inverse relation with area. This

is true for our case as we do not know the pinhole density of the hydride barrier. Due to the small size of some of these junctions they could not be defined by standard photolithography. This step was therefore defined using electron-beam pattern generation (EBPG). Due to practical constraints and ease of fabrication, the EBPG defined resist pattern was used twice without removal, for a self-aligned liftoff in the interlayer dielectric deposition step.

After EBPG exposure on ma-N 2405 negative tone e-beam resist, the resist was developed in ma-D 525 developer. The wafer was then exposed to 4 minutes of SF_6 plasma to etch away the exposed Nb top electrode. However, at the time of fabrication it was not realized that this plasma exposure resulted in very low yield of the junction devices. There is no etch stop below the MgB_2, so once the SiN or Si underneath was exposed during the mesa etch, further exposure to SF_6 plasma in the junction definition step resulted in rapid etching of the Si-exposed areas. This resulted in micron deep trenches near the ground plane. However, this drawback was not realized at the time and fabrication proceeded.

After etching away Nb and defining the junction tops, the interlayer dielectric (ILD) or interconnect insulator was deposited. The purpose of the ILD is to prevent shorting by insulating the wiring layer from the bottom electrode, so that the wiring layer only contacts the top of the junctions. Due to the self-aligned liftoff process, evaporated dielectrics are preferred due to the ease of liftoff. For this reason SiO_2 is selected as the ILD material. Regardless of our processing reasons, SiO_2 has been used as the ILD material in many reported junctions as well due to its low dielectric constant and ease of deposition [127]. We evaporated 250 nm of SiO_2 at a rate of 1.5 Å/s. After ILD deposition, the liftoff is completed in Remover PG. The wafer is oxygen ashed for 1 minute before moving to the wiring layer.

Minor detail: when evaporated, SiO_2 will deposit as SiO unless excess oxygen is bled into the system during deposition. We do not flow excess oxygen, so the ILD is technically expected to be SiO. This difference is expected to have no effect on the function of the ILD.

Wiring Layer

Finally, we define the wiring layer to connect the junction top electrode with bonding pads through liftoff. S1813 was used as the photoresist to define the wiring layer. Different Nb deposition parameters were used, where the power was increased to 250 W, which resulted in a deposition rate of $\sim$ 1.5 Å/s. 200 nm of Nb was deposited

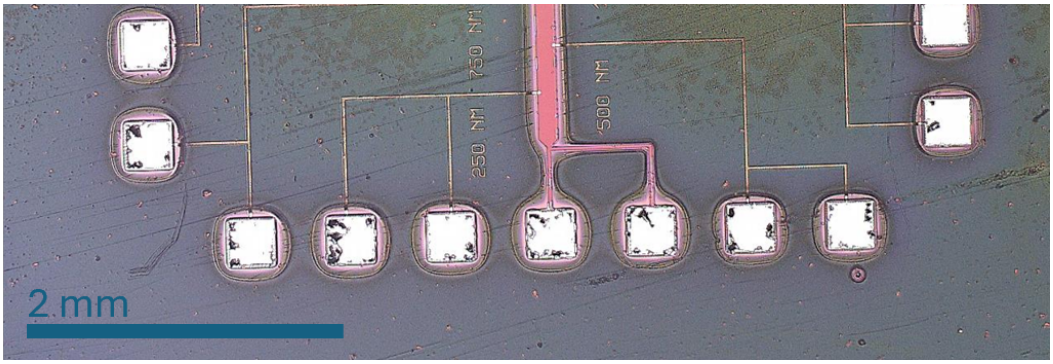

Figure 4.20: Optical microscope image showing wiring layer liftoff issues, with some delamination on the pads, and line edge roughness on the wiring trace.

as the wiring layer. Lifting off sputtered metal is more challenging than evaporated metal due to the more conformal nature of sputtering. This resulted in liftoff issues with the 200 nm thick metal as seen in Figure 4.20. To overcome these issues in later junction fabrication, a bilayer resist was implemented with LOR 5A and S1813. The LOR 5A creates an undercut to allow the solvent to access to the resist easily, even when there is conformal deposition.

The overall junction fabrication is summarized in Figure 4.21. The first completed SIS junction's current-voltage characteristics are discussed in Section 4.5.

4.5 Current-voltage characteristics of MgB_2 SIS junction

The current-voltage (IV) characteristics of the MgB_2 SIS junctions fabricated according to Section 4.4 are discussed in this section. One chip had 12 junctions, as shown in Figure 4.14. Out of the 12 junctions, 11 were measured to be open or unusable. This result unfortunately is expected due to the lack of an etch stop underneath the MgB_2. In an attempt to remove all the MgB_2 in the mesa etch to prevent shorts, the etch was extended into the SiN buffer layer underneath the MgB_2. When the wafer was then exposed to SF_6 plasma in the junction definition step, the exposed SiN and Si was rapidly etched, resulting in a step height > 1 µm. This was oversight of the fabrication process, and an etch stop of alumina or aluminum nitride would have helped to prevent this issue. At the time of fabrication however, the large step height was not realized. So when the 200 nm Nb wiring layer was deposited, there was a break between the Nb on the ground plane and the Nb on the wiring trace. This can also be seen in Figure 4.20, where the wiring trace looks out of focus from the pads along the edge and bottom electrode plane in the middle. The wiring trace being out of focus implies there being some height gap between

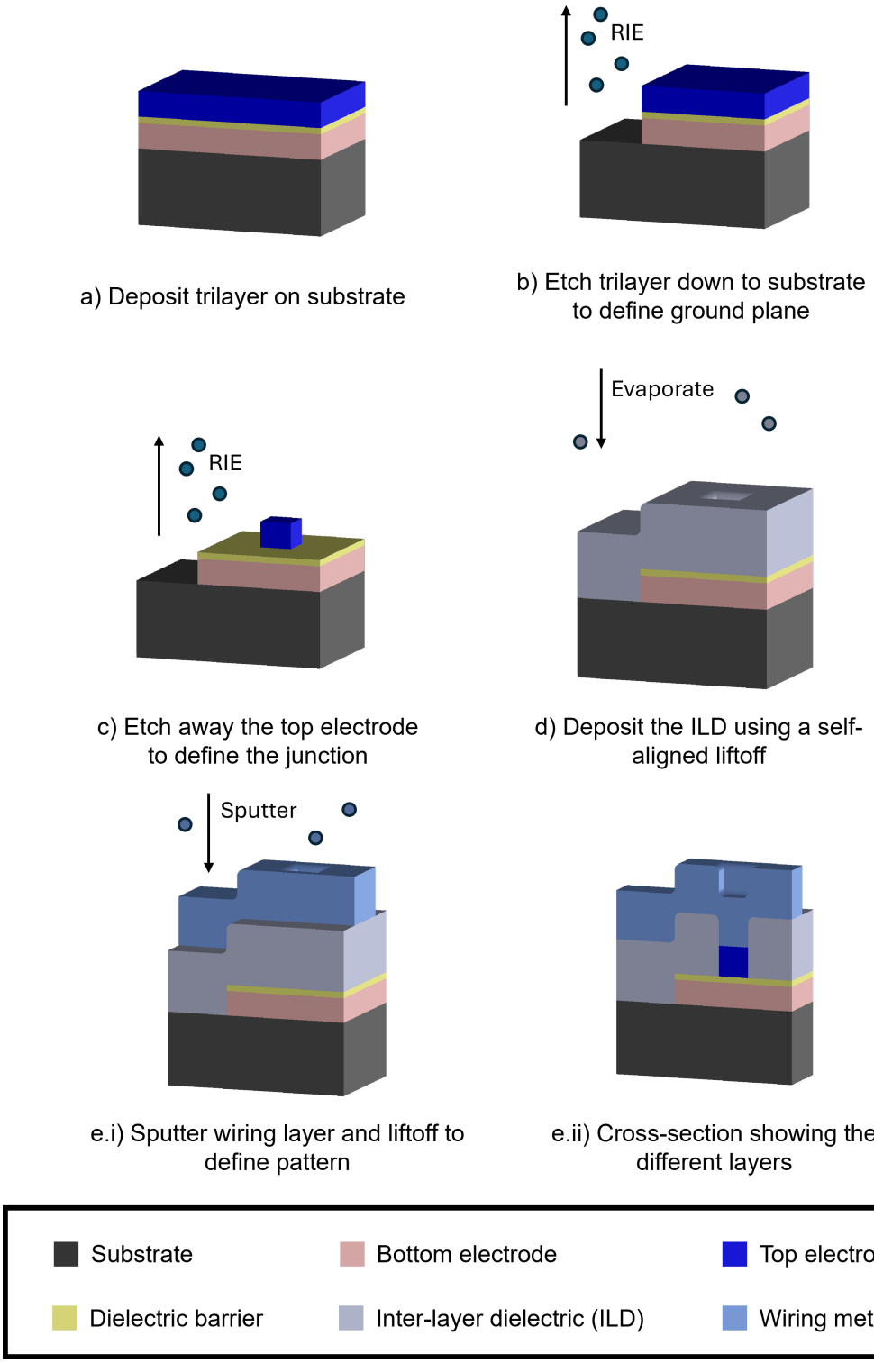

Figure 4.21: Schematic summarizing the SIS junction fabrication process.

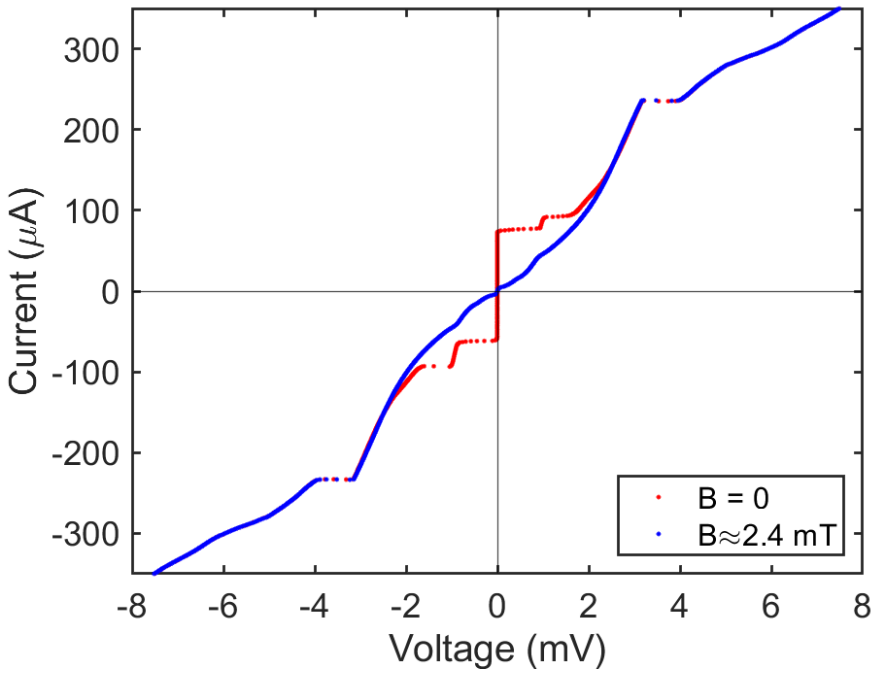

Figure 4.22: Current versus voltage for the measurable 1×1 μm^2 junction at no applied magnetic field (red) and at ≈ 2.4 mT (blue).

the features in focus. AFM confirmed a gap of 2.4 μm between the wiring trace and the top of the ground plane where the junction is. However, in the case of one junction there was enough Nb sputtered conformally along the sidewalls to result in measurable current-voltage data.

Figure 4.22 shows the IV curve for a 1×1 μm^2 that was measurable. We note that there is anomalous behavior in the region for which $3.2\,\text{mV} < |V| < 4$ mV that washes out the IV curve at higher voltages. We hypothesize that this effect is caused by the thin Nb wiring connection on the sidewall which adds significant series resistance to the curve upon becoming a normal metal. To simplify the data analysis, we will look at the region $|V| \in [-3.2, 3.2]$ mV. To focus on the QP tunneling effect we will also look at the curve under a magnetic field to reduce the Josephson noise. However, for those interested, the curve at zero magnetic field exhibits an $I_c = 66 \pm 7$ μA or $J_c = 6.6 \pm 0.7$ kA/cm^2. The reported value is the average of the measured I_c at positive and negative voltages, and the uncertainty accounts shows the difference between the positive and negative I_c.

Figure 4.23 shows the truncated data for the IV curve under a magnetic field, as well as the normalized differential conductance $R_N \cdot \frac{dI}{dV}$ for the same curve. There are

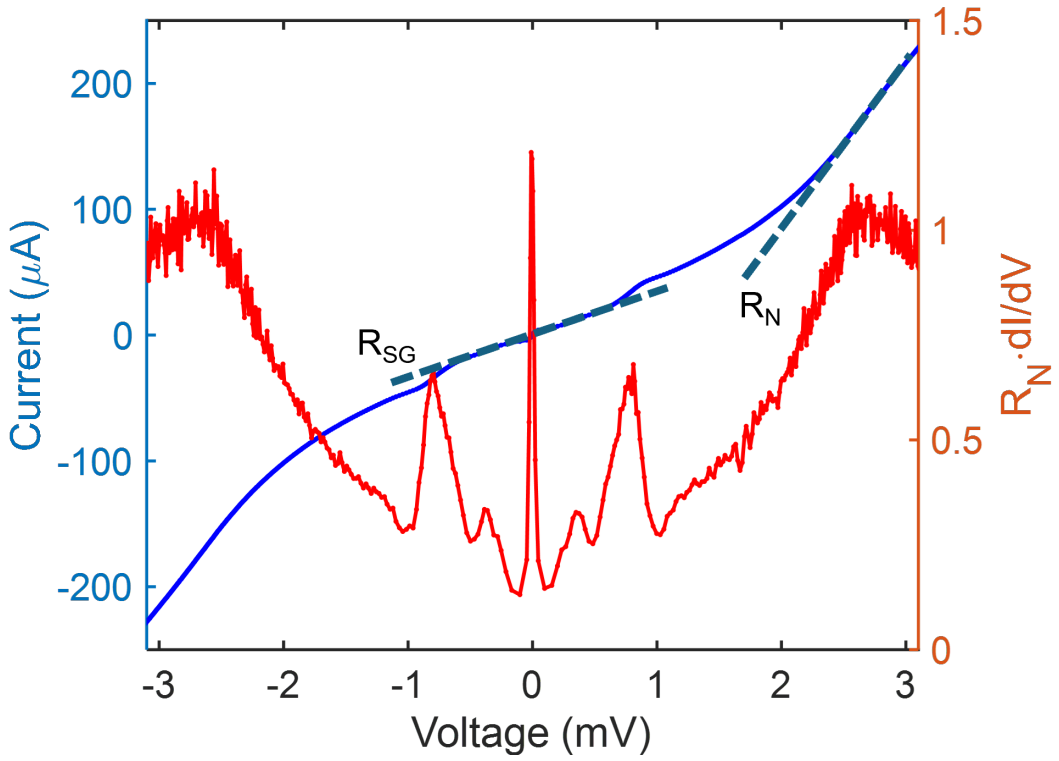

Figure 4.23: Current versus voltage data for the junction under a magnetic field from Figure 4.22, with a truncated x-axis from -3 to +3 mV (blue). Normalized differential conductance versus voltage (red) with the y-axis on the right side. Dashed lines showing the regions used to calculate the subgap and normal resistance.

multiple interesting features of the data. The Josephson current at $V = 0$ has been suppressed by the applied magnetic field, showing that we do indeed have a tunneling limited barrier from the $MgBH_x$ barrier. Moreover, $2.4\ \text{mT} \cdot 1\mu\text{m}^2 \approx 1.2\Phi_0$, where $\Phi_0 = \frac{h}{2e}$ is the magnetic flux quantum. This would also imply that the current is not dominated by pinholes. Otherwise a much a much larger field would be required to compensate for the smaller effective junction area. We use the region for which $|V| < 0.5$ mV to estimate the subgap resistance, and obtain a value of $R_{SG} = 28.7\ \Omega$. Similarly, we use the region for which $2.4 < |V| < 3$ to estimate the normal resistance, and obtain a value of $R_N = 7.93\ \Omega$. These values would suggest a subgap ratio of $Q_R \sim 3.6$. While the subgap ratio is not high enough to use as a mixer right away, it is a promising start to fabricating MgB_2 based SIS junctions using the novel hydride barrier.

Due to the switching artifact seen above 3 mV it is difficult to estimate the V_{gap} for the junction. However, in the subgap region of the conductance curve we notice some

structures that are symmetric about 0 voltage. Since no radiation has been applied these structures cannot be Shapiro steps [166]. Instead, we attribute these features to multiple Andreev reflections (MAR). MAR in SIS junctions arise when electrons and holes undergo successive Andreev reflections at the two superconducting interfaces while traversing the insulating barrier. In an SIS junction biased below V_{gap}, a single QP does not have enough energy to cross the energy gap directly. Instead, it repeatedly reflects as an electron or hole at each superconductor–insulator boundary, gaining an energy eV, where V is the applied voltage [15]. After n such reflections, the QP accumulates enough energy to tunnel into the superconductor, enabling transport across the junction. This process produces a series of subharmonic features at voltages V_n, given by Equation (4.6).

$$eV_n = \frac{V_{gap}}{n} \tag{4.6}$$

MAR is a characteristic of superconducting junctions where the barrier is not fully insulating. This could be because either the barrier is not thick enough or has some conductance [23]. Using MAR theory, we can use the values for the subgap features to estimate a V_{gap}. By fitting the subgap features to a 1/n curve we predict a V_{gap} of 4.1 meV. However, this value should be taken with some caution as it lies outside the switching artifact. However, if we do take 4.1 meV to be the V_{gap}, this would imply that:

$$eV_{gap} = \Delta_{Nb} + \Delta_{MgB_2} = 7.67 \cdot 1.76 k_B T_c + \Delta_{MgB_2}$$

Which would predict $\Delta_{MgB_2} \approx 2.9$ meV.

Additionally, if we look at the conductance-voltage data after the switching in Figure 4.24, we can see some potential features at 4.3 meV and 6.4 meV. The feature at 4.3 meV could potentially correspond to the V_{gap} feature. Additionally, the difference between these two features is 2.1 meV, which could be a feature either associated with the low π-gap of MgB_2 or some additional scattering from the Nb gap. The meaning behind these features is speculative at this point due to the lack of more data and ambiguity created by the switching effect. Further experimentation is required to meaningfully explain the MAR features and the features above 3 mV. To this end, the MgB_2 SIS project members will attempt to fabricate more SIS junctions based on hydrogen-treated MgB_2, while correcting for the overetch into Si.

4.6 Conclusion

We have reported a H_2 plasma reactive ion etching process for magnesium diboride and boron. The H_2 plasma etched the B cap used to passivate MgB_2 at a rate of

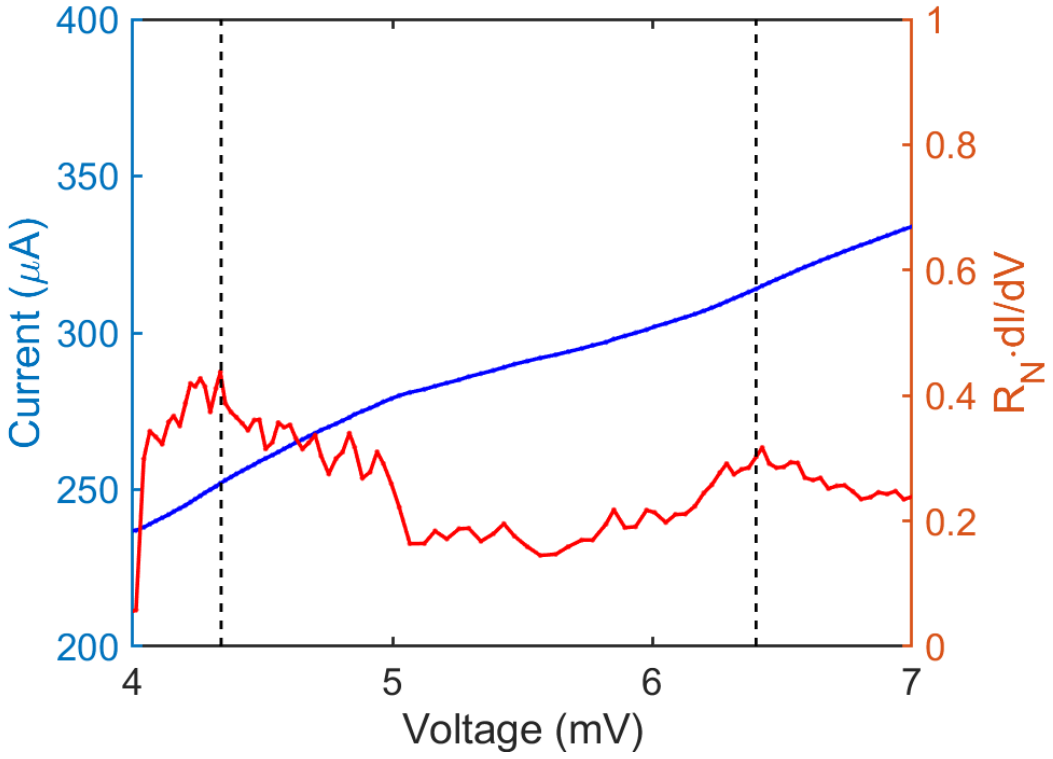

Figure 4.24: Current versus voltage (blue) and normalized conductance versus voltage (red) data for the junction under a magnetic field from Figure 4.22, with a truncated x-axis from 4 to 7 mV. Dashed lines showing features at 4.3 and 6.4 meV.

0.95 nm/min as well as the underlying MgB_2 at a rate of 0.44 nm/min, resulting in an etch rate ratio of 2.15:1 for B:MgB_2. We observe some roughening after the H_2 plasma etch from 0.34 nm R_q on an unetched film to upto 0.51 nm R_q on a film etched for 50 minutes. We also find that the H_2 etched films have a hydride barrier that prevents degradation of the superconducting properties of MgB_2 in ambient air better than unpassivated MgB_2.

We also report a fabrication process to use the hydride barrier as the junction insulator in a hybrid Nb/MgB_2 superconductor-insulator-superconductor junction. The measured device showed a subgap ratio of 3.6. The measured junction also showed features arising from multiple Andreev reflections that can be helpful in analyzing the gaps relevant for tunneling across the junction. While the fabricated set of device had a low yield, further improvements to the fabrication process can help uncover more of the tunneling physics in MgB_2 based junctions.

We anticipate that the ability to selectively etch off the B cap of MgB_2 wafers will facilitate the fabrication of devices with improved superconducting properties due to

the reduced loss from ion bombardment and halide formation. We are also excited for the use of the novel hydride barrier as the junciton insulator to make MgB_2 based SIS junctions for single-photon detection.

Chapter 5

OUTLOOK AND FUTURE WORK

In this thesis, we developed and investigated atomic layer processing techniques for titanium and niobium nitride through atomic layer deposition and atomic layer etching. We also developed a novel hydrogen plasma etching chemistry for magnesium diboride and boron. We then proceeded to use some these techniques to fabricate superconducting-insulator-superconducting junctions for use as heterodyne mixers. The techniques however are not limited to use in SIS mixers, but have a wide range of applications in superconducting electronics such as microresonators, where the loss from interfaces and surfaces have a significant impact on device performance.

In Chapter 2 we reported an plasma-enhanced atomic layer deposition and an isotropic plasma-thermal atomic layer etching process for TiN. TiN ALD was performed using TDMAT and H_2 plasma achieving growth rates of $\sim$ 0.86 Å/cycle, consistent with work reported in [41, 135]. Multiple optimizations were required to arrive at the reported ALD recipe, such as plasma power control, plasma time and the inclusion of a DC bias during plasma exposure. Our final films had a T_c of 3.22 K and resistivity of 222 $\mu\Omega$cm at 6 K. The deposited films also had an RMS surface roughness of $\sim$ 0.42 nm. ALE was achieved using sequential exposures of molecular oxygen and SF_6/H_2 plasma. The SF_6/H_2 plasma selectively etches TiO_2 over TiN for SF_6:H_2 flow rate ratios between 0.1 and 0.2. The etch rate varied from 1.1 Å/cycle at 150 °C to 3.2 Å/cycle at 350 °C. We observed a smoothing effect from ALE, corresponding to a $\sim$ 43% reduction in RMS roughness after 100 cycles. The surface oxygen concentration was reduced by $\sim$ 49% after 100 cycles of ALE, indicating a decrease in the volume of surface oxide. We also find that ALE does not induce any change in T_c beyond that expected from the decrease in film thickness, highlighting the low-damage nature of the process. We then took this process and applied it to a superconductor that had no pre-existing reported ALE chemistry.

In Chapter 3 we have reported a plasma-thermal atomic layer etching process using sequential exposures of O_2 plasma and H_2/SF_6 plasma. O_2 plasma exposure yields a higher fraction of Nb_2O_5 compared to O_2 gas exposure, enabling subsequent volatilization by H_2/SF_6 plasma. The H_2/SF_6 plasma selectively etched Nb_2O_5 over NbN for suitable flow rate ratios. The etch rate is measured to be 1.77 Å/cycle at 125

°C. We observe a smoothing effect from ALE, corresponding to a 55% reduction in RMS roughness after 50 cycles, along with a 59% reduction in surface oxygen concentration. We also find that the T_c of an ALE-treated sample is higher than that of an RIE-treated sample of a similar thickness, highlighting the low-damage nature of the process. However, this was not our first attempt at NbN ALE. Other attempts using thermal cycling and biased *in situ* HF plasma are described in the chapter. We also report a plasma enhanced atomic layer deposition process using TBTDEN and H_2 plasma for growing superconducting NbN. We optimized the substrate temperature for growth and the plasma chemistry for maximizing T_c and minimizing resistivity. The best films were deposited at 400 °C with a H_2 plasma at a growth rate of 0.62 Å/cycle. The optimized films exhibited a T_c of 12.42 K, normal resistivity of 140$\mu\Omega$cm, and R_q = 0.26 nm. There is further room for optimization by varying precursor dose times, plasma times, and plasma power. The NbN ALD recipe was then used to fabricate SIS junctions whose current-voltage characteristics are yet to be measured. Other important characterizations that are planned for the future, are measuring the growth rate and dielectric constant of thin (1–4 nm) dielectrics such as AlN and Al_2O_3 on NbN instead of Si or SiO_2. We anticipate that the ability to engineer the surface of NbN films on the Angstrom-scale will facilitate applications of NbN in not just SIS mixers, but also for other superconducting quantum applications such as SNSPDs and MKIDs.

In Chapter 4 we have reported a H_2 plasma reactive ion etching process for magnesium diboride and boron. The H_2 plasma etched the B cap (used to passivate MgB_2) at a rate of 0.95 nm/min as well as the underlying MgB_2 at a rate of 0.44 nm/min, resulting in an etch rate ratio of 2.15:1 for B:MgB_2. We also find that the H_2 etched films have a hydride or hydroxide barrier that prevents degradation of the MgB_2 T_c and R_s better than unpassivated MgB_2 in ambient conditions. We further use the hydrogen-treated MgB_2 hydride as the barrier in a hybrid Nb/MgB_2 superconductor-insulator-superconductor junction. The measured device showed a subgap ratio of 3.6 and exhibited subgap features originating from multiple Andreev reflections. We then use these features to estimate $V_{gap} \sim 4.1$ mV. However, there was significant overetch around the ground plane that led to many open circuits and a series resistance that washed out features above 4 mV. While the fabricated set of device had a low yield, the failure did not come from the hydrogen treatment but rather the mesa and junction etching steps. Further improvements to the fabrication process are underway by employing an etch stop of AlN or Al_2O_3 to prevent the overetch. The next generation of hydride barrier MgB_2/Nb junctions can hopefully

uncover more of the tunneling physics in MgB_2 based junctions. We anticipate that the ability to selectively etch off the B cap of MgB_2 wafers will facilitate the fabrication of devices with improved superconducting properties due to the reduced loss from ion bombardment and halide formation. We are also excited for the use of the novel hydride barrier as the junction insulator to make MgB_2 based SIS junctions for single-photon detection.

Bibliography

[1] A.A. Abrikosov. The magnetic properties of superconducting alloys. *J. Phys. Chem. Solids*, 2(3):199–208, 1957. doi: 10.1016/0022-3697(57)90083-5.

[2] M. Virginia P. Altoé, Archan Banerjee, Cassidy Berk, Ahmed Hajr, Adam Schwartzberg, Chengyu Song, Mohammed Alghadeer, Shaul Aloni, Michael J. Elowson, John Mark Kreikebaum, Ed K. Wong, Sinéad M. Griffin, Saleem Rao, Alexander Weber-Bargioni, Andrew M. Minor, David I. Santiago, Stefano Cabrini, Irfan Siddiqi, and D. Frank Ogletree. Localization and Mitigation of Loss in Niobium Superconducting Circuits. *PRX Quantum*, 3 (2):020312, 2022. ISSN 2691-3399. doi: 10.1103/PRXQuantum.3.020312.

[3] Vikas Anant, Andrew J. Kerman, Eric A. Dauler, Joel K. W. Yang, Kristine M. Rosfjord, and Karl K. Berggren. Optical properties of superconducting nanowire single-photon detectors. *Opt. Express*, 16(14):10750–10761, July 2008. doi: 10.1364/OE.16.010750.

[4] Alexander Anferov, Aziza Suleymanzade, Andrew Oriani, Jonathan Simon, and David I. Schuster. Millimeter-Wave Four-Wave Mixing via Kinetic Inductance for Quantum Devices. *Phys. Rev. Appl.*, 13(2):024056, February 2020. doi: 10.1103/PhysRevApplied.13.024056.

[5] Anthony J. Annunziata, Daniel F. Santavicca, Luigi Frunzio, Gianluigi Catelani, Michael J. Rooks, Aviad Frydman, and Daniel E. Prober. Tunable superconducting nanoinductors. *Nanotechnology*, 21(44):445202, October 2010. doi: 10.1088/0957-4484/21/44/445202.

[6] Yoshinobu Aoyagi, Kohji Shinmura, Kiyoshi Kawasaki, Tomoko Tanaka, Kenji Gamo, Susumu Namba, and Ichirou Nakamoto. Molecular layer etching of GaAs. *Appl. Phys. Lett.*, 60(8):968–970, February 1992. doi: 10.1063/1.106477.

[7] Seiichiro Ariyoshi, Kensuke Nakajima, Atsushi Saito, Tohru Taino, Hiroyuki Tanoue, Kensuke Koga, Noboru Furukawa, Hironobu Yamada, Shigetoshi Ohshima, Chiko Otani, and Jongsuck Bae. NbN-Based Microwave Kinetic Inductance Detector with a Rewound Spiral Resonator for Broadband Terahertz Detection. *Appl. Phys. Express*, 6(6):064103, May 2013. doi: 10.7567/APEX.6.064103.

[8] Shahid Aslam, Thomas R. Stevenson, Wen-Ting Hsieh, Douglas E. Travers, Hollis H. Jones, and Brook Lakew. Etching of. *IEEE Trans. Appl. Supercond.*, 19(3):257–260, May 2009. doi: 10.1109/TASC.2009.2017855.

[9] Rassul Bairamkulov and Giovanni De Micheli. Superconductive Electronics: A 25-Year Review [Feature]. *IEEE Circuits Syst. Mag.*, 24(2):16–33, May 2024. doi: 10.1109/MCAS.2024.3376492.

[10] J. Bardeen, L. N. Cooper, and J. R. Schrieffer. Theory of Superconductivity. *Phys. Rev.*, 108(5):1175–1204, December 1957. doi: 10.1103/PhysRev.108.1175.

[11] R. Barends, H. L. Hortensius, T. Zijlstra, J. J. A. Baselmans, S. J. C. Yates, J. R. Gao, and T. M. Klapwijk. Contribution of dielectrics to frequency and noise of NbTiN superconducting resonators. *Appl. Phys. Lett.*, 92(22), 2008. ISSN 0003-6951. doi: 10.1063/1.2937837.

[12] J. J. A. Baselmans, F. Facchin, A. Pascual Laguna, J. Bueno, D. J. Thoen, V. Murugesan, N. Llombart, and P. J. de Visser. Ultra-sensitive THz microwave kinetic inductance detectors for future space telescopes. *Astron. Astrophys.*, 665:A17, September 2022. doi: 10.1051/0004-6361/202243840.

[13] G. Beamson and D. Briggs. High Resolution XPS of Organic Polymers: The Scienta ESCA300 Database, 1993. ISSN 0021-9584.

[14] Ekta Bhatia, Jack Lombardi, Tuan Vo, Michael Senatore, Alexander Madden, Soumen Kar, Hunter Frost, Stephen Olson, Jakub Nalaskowski, John Mucci, Brian Martinick, Ilyssa Wells, Thomas Murray, Kevin Musick, Corbet S. Johnson, Stephen McCoy, Daniel L. Campbell, Matthew D. LaHaye, and Satyavolu S. Papa Rao. Ta-based Josephson junctions using insulating ALD TaN tunnel barriers. *arXiv*, November 2025. doi: 10.48550/arXiv.2511.20266.

[15] G. E. Blonder, M. Tinkham, and T. M. Klapwijk. Transition from metallic to tunneling regimes in superconducting microconstrictions: Excess current, charge imbalance, and supercurrent conversion. *Phys. Rev. B*, 25(7):4515–4532, April 1982. doi: 10.1103/PhysRevB.25.4515.

[16] Cristina Buzea and Tsutomu Yamashita. Review of the superconducting properties of MgB2. *Supercond. Sci. Technol.*, 14(11):R115, November 2001. ISSN 0953-2048. doi: 10.1088/0953-2048/14/11/201.

[17] Faustin W. Carter, Trupti Khaire, Clarence Chang, and Valentyn Novosad. Low-loss single-photon NbN microwave resonators on Si. *Appl. Phys. Lett.*, 115(9):092602, August 2019. doi: 10.1063/1.5115276.

[18] Colin T. Carver, John J. Plombon, Patricio E. Romero, Satyarth Suri, Tristan A. Tronic, and Robert B. Turkot. Atomic Layer Etching: An Industry Perspective. *ECS J. Solid State Sci. Technol.*, 4(6):N5005, February 2015. ISSN 2162-8777. doi: 10.1149/2.0021506jss.

[19] David S. Catherall, Azmain A. Hossain, Anthony J. Ardizzi, and Austin J. Minnich. Atomic layer etching of SiO2 using sequential exposures of Al(CH3)3 and H2/SF6 plasma. *J. Vac. Sci. Technol., A*, 42(5):052605, September 2024. doi: 10.1116/6.0003793.

[20] Mu-Hsuan Chan and Fu-Hsing Lu. X-ray photoelectron spectroscopy analyses of titanium oxynitride films prepared by magnetron sputtering using air/Ar mixtures. *Thin Solid Films*, 517(17):5006–5009, 2009. ISSN 0040-6090. doi: 10.1016/j.tsf.2009.03.100.

[21] Josephine B. Chang, Michael R. Vissers, Antonio D. Córcoles, Martin Sandberg, Jiansong Gao, David W. Abraham, Jerry M. Chow, Jay M. Gambetta, Mary Beth Rothwell, George A. Keefe, Matthias Steffen, and David P. Pappas. Improved superconducting qubit coherence using titanium nitride. *Appl. Phys. Lett.*, 103(1), 2013. ISSN 0003-6951. doi: 10.1063/1.4813269.

[22] Ivy I. Chen, Jennifer Solgaard, Ryoto Sekine, Azmain A. Hossain, Anthony Ardizzi, David S. Catherall, Alireza Marandi, James R. Renzas, Frank Greer, and Austin J. Minnich. Isotropic atomic layer etching of MgO-doped lithium niobate using sequential exposures of H2 and SF6/Ar plasmas. *J. Vac. Sci. Technol., A*, 42(6):062603, October 2024. doi: 10.1116/6.0003962.

[23] Ke Chen, Daniel Cunnane, Yi Shen, X. X. Xi, Alan W. Kleinsasser, and John M. Rowell. Multiple Andreev reflection in MgB2/MgO/MgB2 Josephson junctions. *Appl. Phys. Lett.*, 100(12):122601, March 2012. ISSN 0003-6951. doi: 10.1063/1.3695159.

[24] Risheng Cheng, Sihao Wang, and Hong X. Tang. Superconducting nanowire single-photon detectors fabricated from atomic-layer-deposited NbN. *Appl. Phys. Lett.*, 115(24):241101, December 2019. doi: 10.1063/1.5131664.

[25] Nicholas J. Chittock, Martijn F. J. Vos, Tahsin Faraz, Wilhelmus M. M. (Erwin) Kessels, Harm C. M. Knoops, and Adriaan J. M. Mackus. Isotropic plasma atomic layer etching of Al2O3 using a fluorine containing plasma and Al(CH3)3. *Appl. Phys. Lett.*, 117(16), 2020. ISSN 0003-6951. doi: 10.1063/5.0022531.

[26] Nicholas J. Chittock, Yi Shu, Simon D. Elliott, Harm C. M. Knoops, W. M. M. (Erwin). Kessels, and Adriaan J. M. Mackus. Isotropic atomic layer etching of GaN using SF6 plasma and Al(CH3)3. *J. Appl. Phys.*, 134(7), August 2023. doi: 10.1063/5.0158129.

[27] Marco Colangelo, Alexander B. Walter, Boris A. Korzh, Ekkehart Schmidt, Bruce Bumble, Adriana E. Lita, Andrew D. Beyer, Jason P. Allmaras, Ryan M. Briggs, Alexander G. Kozorezov, Emma E. Wollman, Matthew D. Shaw, and Karl K. Berggren. Large-Area Superconducting Nanowire Single-Photon Detectors for Operation at Wavelengths up to 7.4 μm. *Nano Lett.*, 22(14): 5667–5673, July 2022. doi: 10.1021/acs.nanolett.1c05012.

[28] P. C. J. J. Coumou, M. R. Zuiddam, E. F. C. Driessen, P. J. de Visser, J. J. A. Baselmans, and T. M. Klapwijk. Microwave Properties of Superconducting Atomic-Layer Deposited TiN Films. *IEEE Trans. Appl. Supercond.*, 23(3):

7500404, December 2012. ISSN 1558-2515. doi: 10.1109/TASC.2012.2236603.

[29] J.-C. Crivello, B. Dam, R. V. Denys, M. Dornheim, D. M. Grant, J. Huot, T. R. Jensen, P. de Jongh, M. Latroche, C. Milanese, D. Milčius, G. S. Walker, C. J. Webb, C. Zlotea, and V. A. Yartys. Review of magnesium hydride-based materials: development and optimisation. *Appl. Phys. A*, 122(2):97, February 2016. ISSN 1432-0630. doi: 10.1007/s00339-016-9602-0.

[30] Andrew E. Dane, Adam N. McCaughan, Di Zhu, Qingyuan Zhao, Chung-Soo Kim, Niccolo Calandri, Akshay Agarwal, Francesco Bellei, and Karl K. Berggren. Bias sputtered NbN and superconducting nanowire devices. *Appl. Phys. Lett.*, 111(12), September 2017. doi: 10.1063/1.4990066.

[31] A. Darlinski and J. Halbritter. Angle-resolved XPS studies of oxides at NbN, NbC, and Nb surfaces. *Surf. Interface Anal.*, 10(5):223–237, June 1987. doi: 10.1002/sia.740100502.

[32] Peter K. Day, Henry G. LeDuc, Benjamin A. Mazin, Anastasios Vayonakis, and Jonas Zmuidzinas. A broadband superconducting detector suitable for use in large arrays. *Nature*, 425:817–821, 2003. ISSN 1476-4687. doi: 10.1038/nature02037.

[33] Tiago C. Dias, Chloé Fromentin, Luís L. Alves, Antonio Tejero-del Caz, Tiago Silva, and Vasco Guerra. A reaction mechanism for oxygen plasmas. *Plasma Sources Sci. Technol.*, 32(8):084003, August 2023. doi: 10.1088/1361-6595/aceaa4.

[34] Jaime W. DuMont, Amy E. Marquardt, Austin M. Cano, and Steven M. George. Thermal Atomic Layer Etching of SiO2 by a "Conversion-Etch" Mechanism Using Sequential Reactions of Trimethylaluminum and Hydrogen Fluoride. *ACS Appl. Mater. Interfaces*, 9(11):10296–10307, March 2017. doi: 10.1021/acsami.7b01259.

[35] Paul Ehrlich, Fritz Plöger, and Gerhard Pietzka. Über Niobtrifluorid. *Z. Anorg. Allg. Chem.*, 282(1-6):19–23, December 1955. doi: 10.1002/zaac.19552820105.

[36] J. W. Elam, M. Schuisky, J. D. Ferguson, and S. M. George. Surface chemistry and film growth during TiN atomic layer deposition using TDMAT and NH3. *Thin Solid Films*, 436(2):145–156, 2003. ISSN 0040-6090. doi: 10.1016/S0040-6090(03)00533-9.

[37] J. Merle Elson and Jean M. Bennett. Calculation of the power spectral density from surface profile data. *Appl. Opt.*, 34(1):201–208, 1995. ISSN 2155-3165. doi: 10.1364/AO.34.000201.

[38] Krishna Enni, K. Sreelakshmy, and Medha Lal R. Comparative study on the effects of dry and wet etching on surface characteristics of fused silica optics. *Opt. Mater.*, 162:116809, May 2025. ISSN 0925-3467. doi: 10.1016/j.optmat.2025.116809.

[39] Iman Esmaeil Zadeh, Johannes W. N. Los, Ronan B. M. Gourgues, Jin Chang, Ali W. Elshaari, Julien Romain Zichi, Yuri J. van Staaden, Jeroen P. E. Swens, Nima Kalhor, Antonio Guardiani, Yun Meng, Kai Zou, Sergiy Dobrovolskiy, Andreas W. Fognini, Dennis R. Schaart, Dan Dalacu, Philip J. Poole, Michael E. Reimer, Xiaolong Hu, Silvania F. Pereira, Val Zwiller, and Sander N. Dorenbos. Efficient Single-Photon Detection with 7.7 ps Time Resolution for Photon-Correlation Measurements. *ACS Photonics*, 7 (7):1780–1787, July 2020. doi: 10.1021/acsphotonics.0c00433.

[40] Fred Fairbrother and William C. Frith. 675. The halides of niobium (columbium) and tantalum. Part III. The vapour pressures of niobium (columbium) and tantalum pentafluorides. *J. Chem. Soc.*, pages 3051–3056, January 1951. doi: 10.1039/JR9510003051.

[41] Tahsin Faraz, Harm C. M. Knoops, Marcel A. Verheijen, Cristian A. A. van Helvoirt, Saurabh Karwal, Akhil Sharma, Vivek Beladiya, Adriana Szeghalmi, Dennis M. Hausmann, Jon Henri, Mariadriana Creatore, and Wilhelmus M. M. Kessels. Tuning Material Properties of Oxides and Nitrides by Substrate Biasing during Plasma-Enhanced Atomic Layer Deposition on Planar and 3D Substrate Topographies. *ACS Appl. Mater. Interfaces*, 10(15): 13158–13180, 2018. ISSN 1944-8244. doi: 10.1021/acsami.8b00183.

[42] John Femi-Oyetoro, Sasha Sypkens, Henry LeDuc, Matthew Dickie, Andrew Beyer, Peter Day, and Frank Greer. Plasma-enhanced atomic layer deposition of titanium nitride for superconducting devices. *Appl. Phys. Lett.*, 125(6), August 2024. ISSN 0003-6951. doi: 10.1063/5.0210190.

[43] F. Fillot, T. Morel, S. Minoret, I. Matko, S. Maîtrejean, B. Guillaumot, B. Chenevier, and T. Billon. Investigations of titanium nitride as metal gate material, elaborated by metal organic atomic layer deposition using TDMAT and NH3. *Microelectron. Eng.*, 82(3):248–253, 2005. ISSN 0167-9317. doi: 10.1016/j.mee.2005.07.083.

[44] Andreas Fischer, Richard Janek, John Boniface, Thorsten Lill, K. J. Kanarik, Yang Pan, Vahid Vahedi, and Richard A. Gottscho. Plasma-assisted thermal atomic layer etching of Al2O3. In *Proceedings Volume 10149, Advanced Etch Technology for Nanopatterning VI*, volume 10149, pages 20–24. SPIE, 2017. doi: 10.1117/12.2258129.

[45] Andreas Fischer, Aaron Routzahn, Steven M. George, and Thorsten Lill. Thermal atomic layer etching: A review. *J. Vac. Sci. Technol., A*, 39(3), 2021. ISSN 0734-2101. doi: 10.1116/6.0000894.

[46] S. Frasca, B. Korzh, M. Colangelo, D. Zhu, A. E. Lita, J. P. Allmaras, E. E. Wollman, V. B. Verma, A. E. Dane, E. Ramirez, A. D. Beyer, S. W. Nam, A. G. Kozorezov, M. D. Shaw, and K. K. Berggren. Determining the depairing current in superconducting nanowire single-photon detectors. *Phys. Rev. B*, 100(5):054520, August 2019. doi: 10.1103/PhysRevB.100.054520.

[47] S. Frasca, I. N. Arabadzhiev, S. Y. Bros de Puechredon, F. Oppliger, V. Jouanny, R. Musio, M. Scigliuzzo, F. Minganti, P. Scarlino, and E. Charbon. NbN films with high kinetic inductance for high-quality compact superconducting resonators. *Phys. Rev. Appl.*, 20(4):044021, October 2023. doi: 10.1103/PhysRevApplied.20.044021.

[48] Jiansong Gao, Jonas Zmuidzinas, Benjamin A. Mazin, Henry G. LeDuc, and Peter K. Day. Noise properties of superconducting coplanar waveguide microwave resonators. *Appl. Phys. Lett.*, 90(10), 2007. ISSN 0003-6951. doi: 10.1063/1.2711770.

[49] Jiansong Gao, Miguel Daal, Anastasios Vayonakis, Shwetank Kumar, Jonas Zmuidzinas, Bernard Sadoulet, Benjamin A. Mazin, Peter K. Day, and Henry G. Leduc. Experimental evidence for a surface distribution of two-level systems in superconducting lithographed microwave resonators. *Appl. Phys. Lett.*, 92(15), 2008. ISSN 0003-6951. doi: 10.1063/1.2906373.

[50] Ran Gao, Wenlong Yu, Hao Deng, Hsiang-Sheng Ku, Zhisheng Li, Minghua Wang, Xiaohe Miao, Yue Lin, and Chunqing Deng. Epitaxial titanium nitride microwave resonators: Structural, chemical, electrical, and microwave properties. *Phys. Rev. Mater.*, 6(3):036202, 2022. ISSN 2475-9953. doi: 10.1103/PhysRevMaterials.6.036202.

[51] Steven M. George. Atomic Layer Deposition: An Overview. *Chem. Rev.*, 110(1):111–131, January 2010. ISSN 0009-2665. doi: 10.1021/cr900056b.

[52] Steven M. George. Mechanisms of Thermal Atomic Layer Etching. *Acc. Chem. Res.*, 53(6):1151–1160, 2020. ISSN 0001-4842. doi: 10.1021/acs.accounts.0c00084.

[53] Steven M. George and Younghee Lee. Prospects for Thermal Atomic Layer Etching Using Sequential, Self-Limiting Fluorination and Ligand-Exchange Reactions. *ACS Nano*, 2016(10):,5, May 2016. doi: 10.1021/acsnano.6b02991.

[54] Sven H. Gerritsen, Nicholas J. Chittock, Vincent Vandalon, Marcel A. Verheijen, Harm C. M. Knoops, Wilhelmus M. M. Kessels, and Adriaan J. M. Mackus. Surface Smoothing by Atomic Layer Deposition and Etching for the Fabrication of Nanodevices. *ACS Appl. Nano Mater.*, 5(12):18116–18126, 2022. doi: 10.1021/acsanm.2c04025.

[55] Bianca Giaccone, Martina Martinello, and John Zasadzinski. *Study of the Niobium Oxide Structure and Microscopic Effect of Plasma Processing on the Niobium Surface*. JACOW Publishing, Geneva, Switzerland, October 2022. doi: 10.18429/JACoW-SRF2021-WEPCAV001.

[56] Hong Seong Gil, Doo San Kim, Yun Jong Jang, Dea Whan Kim, Hea In Kwon, Gyoung Chan Kim, Dong Woo Kim, and Geun Young Yeom. Selective isotropic etching of SiO2 over Si3N4 using NF3/H2 remote plasma and methanol vapor. *Sci. Rep.*, 13(11599):1–12, July 2023. doi: 10.1038/s41598-023-38359-4.

[57] W. P. Gilbreath. The Vapor Pressure of Magnesium Between 223 Deg and 385 Deg C. *NASA Technical Notes*, NASA-TM-X-54897, January 1964.

[58] V. L. Ginzburg and L. D. Landau. On the Theory of Superconductivity. In *On Superconductivity and Superfluidity*, pages 113–137. Springer, Berlin, Germany, 2009. ISBN 978-3-540-68008-6. doi: 10.1007/978-3-540-68008-6_4.

[59] G. N. Gol'tsman, O. Okunev, G. Chulkova, A. Lipatov, A. Semenov, K. Smirnov, B. Voronov, A. Dzardanov, C. Williams, and Roman Sobolewski. Picosecond superconducting single-photon optical detector. *Appl. Phys. Lett.*, 79(6):705–707, August 2001. doi: 10.1063/1.1388868.

[60] B. B. Goodman. Type II superconductors. *Rep. Prog. Phys.*, 29(2):445, July 1966. ISSN 0034-4885. doi: 10.1088/0034-4885/29/2/302.

[61] F. P. Gortsema and R. Didchenko. The Preparation and Properties of Niobium Tetrafluoride and Oxyfluorides. *Inorg. Chem.*, 4(2):182–186, February 1965. doi: 10.1021/ic50024a012.

[62] J. Greenfield, C. Bell, F. Faramarzi, C. Kim, R. Basu Thakur, A. Wandui, C. Frez, P. Mauskopf, and D. Cunnane. Kinetic inductance and non-linearity of MgB2 films at 4K. *Appl. Phys. Lett.*, 126(2):022602, January 2025. ISSN 0003-6951. doi: 10.1063/5.0245866.

[63] N. N. Greenwood and A. Earnshaw. *Chemistry of the Elements*. Butterworth-Heinemann, Oxford, England, UK, December 1997.

[64] Shuya Guo, Qi Chen, Danfeng Pan, Yaojun Wu, Xuecou Tu, Guanglong He, Hang Han, Feiyan Li, Xiaoqing Jia, Qingyuan Zhao, Hengbin Zhang, Xiaomin Bei, Jun Xie, Labao Zhang, Jian Chen, Lin Kang, and Peiheng Wu. Fabrication of superconducting niobium nitride nanowire with high aspect ratio for X-ray photon detection. *Sci. Rep.*, 10(9057):1–8, June 2020. doi: 10.1038/s41598-020-65901-5.

[65] A. Gurevich, S. Patnaik, V. Braccini, K. H. Kim, C. Mielke, X. Song, L. D. Cooley, S. D. Bu, D. M. Kim, J. H. Choi, L. J. Belenky, J. Giencke, M. K.

Lee, W. Tian, X. Q. Pan, A. Siri, E. E. Hellstrom, C. B. Eom, and D. C. Larbalestier. Very high upper critical fields inMgB2 produced by selective tuning of impurity scattering. *Supercond. Sci. Technol.*, 17(2):278, December 2003. ISSN 0953-2048. doi: 10.1088/0953-2048/17/2/008.

[66] Takeshi Harada, Kenji Gamo, and Susumu Namba. Dry Etching of Nb and Fabrication of Nb Variable-Thickness-Bridges. *Jpn. J. Appl. Phys.*, 20(1): 259, January 1981. doi: 10.1143/JJAP.20.259.

[67] T. M. Hazard, A. Gyenis, A. Di Paolo, A. T. Asfaw, S. A. Lyon, A. Blais, and A. A. Houck. Nanowire Superinductance Fluxonium Qubit. *Phys. Rev. Lett.*, 122(1):010504, 2019. ISSN 1079-7114. doi: 10.1103/PhysRevLett.122.010504.

[68] John Hennessy, Christopher S. Moore, Kunjithapatham Balasubramanian, April D. Jewell, Kevin France, and Shouleh Nikzad. Enhanced atomic layer etching of native aluminum oxide for ultraviolet optical applications. *J. Vac. Sci. Technol., A*, 35(4), 2017. ISSN 0734-2101. doi: 10.1116/1.4986945.

[69] J. J. Hinchen and C. M. Banas. cw HF ELECTRIC-DISCHARGE MIXING LASER. *Appl. Phys. Lett.*, 17(9):386–388, November 1970. doi: 10.1063/1.1653447.

[70] Johann H. Hinken. *Superconductor Electronics: Fundamentals and Microwave Applications*. Springer, December 1989. ISBN 978-3-64274744-1.

[71] J. Hinz, A. J. Bauer, and L. Frey. Analysis of NbN thin film deposition by plasma-enhanced ALD for gate electrode application. *Semicond. Sci. Technol.*, 25(7):075009, June 2010. ISSN 0268-1242. doi: 10.1088/0268-1242/25/7/075009.

[72] Byeong Ho Eom, Peter K. Day, Henry G. LeDuc, and Jonas Zmuidzinas. A wideband, low-noise superconducting amplifier with high dynamic range. *Nat. Phys.*, 8:623–627, 2012. ISSN 1745-2481. doi: 10.1038/nphys2356.

[73] Y. Horiike, T. Tanaka, M. Nakano, S. Iseda, H. Sakaue, A. Nagata, H. Shindo, S. Miyazaki, and M. Hirose. Digital chemical vapor deposition and etching technologies for semiconductor processing. *J. Vac. Sci. Technol., A*, 8(3): 1844–1850, 1990. ISSN 0734-2101. doi: 10.1116/1.576814.

[74] Azmain A. Hossain, Haozhe Wang, David S. Catherall, Martin Leung, Harm C. M. Knoops, James R. Renzas, and Austin J. Minnich. Isotropic plasma-thermal atomic layer etching of superconducting titanium nitride films using sequential exposures of molecular oxygen and SF6/H2 plasma. *J. Vac. Sci. Technol., A*, 41(6):062601, September 2023. doi: 10.1116/6.0002965.

[75] Z. P. Hu, Y. P. Li, M. R. Ji, and J. X. Wu. The interaction of oxygen with niobium studied by XPS and UPS. *Solid State Commun.*, 71(10):849–852, September 1989. doi: 10.1016/0038-1098(89)90210-X.

[76] N. N. Iosad, V. V. Roddatis, S. N. Polyakov, A. V. Varlashkin, B. D. Jackson, and P. N. Dmitriev. Superconducting transition metal nitride films for THz SIS mixers. *IEEE Trans. Appl. Supercond.*, 11(1):3832–3835, August 2002. doi: 10.1109/77.919900.

[77] Yachin Ivry, Chung-Soo Kim, Andrew E. Dane, Domenico De Fazio, Adam N. McCaughan, Kristen A. Sunter, Qingyuan Zhao, and Karl K. Berggren. Universal scaling of the critical temperature for thin films near the superconducting-to-insulating transition. *Phys. Rev. B*, 90(21):214515, December 2014. doi: 10.1103/PhysRevB.90.214515.

[78] Tevis D. B. Jacobs, Till Junge, and Lars Pastewka. Quantitative characterization of surface topography using spectral analysis. *Surf. Topogr. Metrol. Prop.*, 5(1):013001, 2017. ISSN 2051-672X. doi: 10.1088/2051-672X/aa51f8.

[79] Dominik Jaeger and Jörg Patscheider. A complete and self-consistent evaluation of XPS spectra of TiN. *J. Electron Spectrosc. Relat. Phenom.*, 185(11): 523–534, 2012. ISSN 0368-2048. doi: 10.1016/j.elspec.2012.10.011.

[80] Nicholas R. Johnson and Steven M. George. WO3 and W Thermal Atomic Layer Etching Using "Conversion-Fluorination" and "Oxidation-Conversion-Fluorination" Mechanisms. *ACS Appl. Mater. Interfaces*, 9(39):34435–34447, October 2017. doi: 10.1021/acsami.7b09161.

[81] B. D. Josephson. Possible new effects in superconductive tunnelling. *Physics Letters*, 1(17):251—253, 1962. doi: 10.1016/0031-9163(62)91369-0.

[82] G. Jouve, C. Séverac, and S. Cantacuzène. XPS study of NbN and (NbTi)N superconducting coatings. *Thin Solid Films*, 287(1):146–153, October 1996. doi: 10.1016/S0040-6090(96)08776-7.

[83] Ji-Eun Jung, Yuri Barsukov, Vladimir Volynets, Gonjun Kim, Sang Ki Nam, Kyuhee Han, Shuo Huang, and Mark J. Kushner. Highly selective Si3N4/SiO2 etching using an NF3/N2/O2/H2 remote plasma. II. Surface reaction mechanism. *J. Vac. Sci. Technol., A*, 38(2), 2020. ISSN 0734-2101. doi: 10.1116/1.5125569.

[84] Keren J. Kanarik, Thorsten Lill, Eric A. Hudson, Saravanapriyan Sriraman, Samantha Tan, Jeffrey Marks, Vahid Vahedi, and Richard A. Gottscho. Overview of atomic layer etching in the semiconductor industry. *J. Vac. Sci. Technol., A*, 33(2):020802, March 2015. ISSN 0734-2101. doi: 10.1116/1.4913379.

[85] Keren J. Kanarik, Samantha Tan, Wenbing Yang, Taeseung Kim, Thorsten Lill, Alexander Kabansky, Eric A. Hudson, Tomihito Ohba, Kazuo Nojiri, Jengyi Yu, Rich Wise, Ivan L. Berry, Yang Pan, Jeffrey Marks, and Richard A. Gottscho. Predicting synergy in atomic layer etching. *J. Vac. Sci. Technol., A*, 35(5), 2017. ISSN 0734-2101. doi: 10.1116/1.4979019.

[86] Keren J. Kanarik, Samantha Tan, and Richard A. Gottscho. Atomic Layer Etching: Rethinking the Art of Etch. *J. Phys. Chem. Lett.*, 9(16):4814–4821, August 2018. doi: 10.1021/acs.jpclett.8b00997.

[87] Andrew J. Kerman, Eric A. Dauler, Joel K. W. Yang, Kristine M. Rosfjord, Vikas Anant, Karl K. Berggren, Gregory N. Gol'tsman, and Boris M. Voronov. Constriction-limited detection efficiency of superconducting nanowire single-photon detectors. *Appl. Phys. Lett.*, 90(10):101110, March 2007. doi: 10.1063/1.2696926.

[88] Erwin Kessels. Atomic Limits ALD Database, 2025. doi: 10.6100/aldatabase.

[89] Erwin Kessels, Anjana Devi, Jin-Seong Park, Mikko Ritala, Angel Yanguas-Gil, and Claudia Wiemer. Atomic layer deposition. *Nat. Rev. Methods Primers*, 5(66):66, October 2025. ISSN 2662-8449. doi: 10.1038/s43586-025-00435-6.

[90] J. B. Ketterson and S. N. Song. *Superconductivity*. Cambridge University Press, Feb 1999. ISBN 0521562953.

[91] A. Kher, P. K. Day, B. H. Eom, J. Zmuidzinas, and H. G. Leduc. Kinetic Inductance Parametric Up-Converter. *J. Low Temp. Phys.*, 184(1):480–485, 2016. ISSN 1573-7357. doi: 10.1007/s10909-015-1364-0.

[92] Chang-Eun Kim, Keith G. Ray, David F. Bahr, and Vincenzo Lordi. Electronic structure and surface properties of MgB_2(0001) upon oxygen adsorption. *Phys. Rev. B*, 97(19):195416, May 2018. doi: 10.1103/PhysRevB.97.195416.

[93] Changsub Kim, Christina Bell, Jake M. Evans, Jonathan Greenfield, Emma Batson, Karl K. Berggren, Nathan S. Lewis, and Daniel P. Cunnane. Wafer-Scale MgB2 Superconducting Devices. *ACS Nano*, 18(40):27782–27792, October 2024. ISSN 1936-0851. doi: 10.1021/acsnano.4c11001.

[94] Eun Koo Kim, Jong Woo Hong, Woong Sun Lim, Ja Yeon Kim, Kyung Lim Kim, Jong Soon Park, Yun Jae Park, Chan Ho Kim, Hyeong Joon Eoh, Jun Won Jeong, Sung Hyun Kim, Young Woo Jeon, Dong Woo Kim, and Geun Young Yeom. Molecular dynamics simulation of atomic layer etching for sidewall damage recovery in GaN-based structures. *Sci. Rep.*, 16(7110): 7110, February 2026. ISSN 2045-2322. doi: 10.1038/s41598-026-38333-w.

[95] H. Kim. Atomic layer deposition of metal and nitride thin films: Current research efforts and applications for semiconductor device processing. *Journal of Vacuum Science & Technology B: Microelectronics and Nanometer Structures Processing, Measurement, and Phenomena*, 21(6):2231–2261, 2003. ISSN 1071-1023. doi: 10.1116/1.1622676.

[96] Sunmi Kim, Hirotaka Terai, Taro Yamashita, Wei Qiu, Tomoko Fuse, Fumiki Yoshihara, Sahel Ashhab, Kunihiro Inomata, and Kouichi Semba. Enhanced coherence of all-nitride superconducting qubits epitaxially grown on silicon substrate. *Commun. Mater.*, 2(98):1–7, September 2021. doi: 10.1038/s43246-021-00204-4.

[97] E. Knehr, A. Kuzmin, D. Yu Vodolazov, M. Ziegler, S. Doerner, K. Ilin, M. Siegel, R. Stolz, and H. Schmidt. Nanowire single-photon detectors made of atomic layer-deposited niobium nitride. *Supercond. Sci. Technol.*, 32(12): 125007, October 2019. doi: 10.1088/1361-6668/ab48d7.

[98] K. K. Ko and S. W. Pang. Controllable layer-by-layer etching of III–V compound semiconductors with an electron cyclotron resonance source. *J. Vac. Sci. Technol. B*, 11(6):2275–2279, November 1993. doi: 10.1116/1.586889.

[99] J. W. Kooi, J. J. A. Baselmans, M. Hajenius, J. R. Gao, T. M. Klapwijk, P. Dieleman, A. Baryshev, and G. de Lange. IF impedance and mixer gain of NbN hot electron bolometers. *J. Appl. Phys.*, 101(4):044511, February 2007. doi: 10.1063/1.2400086.

[100] Jacob W. Kooi, Darren J. Hayton, Bruce Bumble, Henry George LeDuc, Anders Skalare, and Maria Alonso-delPino. Quantum Limited SIS Receiver Technology for the Detection of Water Isotopologue Emission From Comets. *IEEE Trans. Terahertz Sci. Technol.*, 10(6):569–582, July 2020. doi: 10.1109/TTHZ.2020.3010123.

[101] M. V. Kuznetsov, Ju. F. Zhuravlev, V. A. Zhilyaev, and V. A. Gubanov. XPS study of the nitrides, oxides and oxynitrides of titanium. *J. Electron Spectrosc. Relat. Phenom.*, 58(1):1–9, 1992. ISSN 0368-2048. doi: 10.1016/0368-2048(92)80001-O.

[102] E. Langereis, S. B. S. Heil, M. C. M. van de Sanden, and W. M. M. Kessels. In situ spectroscopic ellipsometry study on the growth of ultrathin TiN films by plasma-assisted atomic layer deposition. *J. Appl. Phys.*, 100(2), 2006. ISSN 0021-8979. doi: 10.1063/1.2214438.

[103] Henry G. Leduc, Bruce Bumble, Peter K. Day, Byeong Ho Eom, Jiansong Gao, Sunil Golwala, Benjamin A. Mazin, Sean McHugh, Andrew Merrill, David C. Moore, Omid Noroozian, Anthony D. Turner, and Jonas Zmuidzinas. Titanium nitride films for ultrasensitive microresonator detectors. *Appl. Phys. Lett.*, 97(10), 2010. ISSN 0003-6951. doi: 10.1063/1.3480420.

[104] Yeonkyu Lee, Jinyoung Yun, Chanyoung Lee, M. Sirena, Jeehoon Kim, and N. Haberkorn. Penetration depth in dirty superconducting NbTiN thin films grown at room temperature. *Appl. Phys. A*, 130(7):504, July 2024. ISSN 1432-0630. doi: 10.1007/s00339-024-07650-0.

[105] Younghee Lee and Steven M. George. Atomic Layer Etching of Al2O3 Using Sequential, Self-Limiting Thermal Reactions with Sn(acac)2 and Hydrogen Fluoride. *ACS Nano*, 9(2):2061–2070, February 2015. doi: 10.1021/nn507277f.

[106] Younghee Lee and Steven M. George. Thermal Atomic Layer Etching of Titanium Nitride Using Sequential, Self-Limiting Reactions: Oxidation to TiO2 and Fluorination to Volatile TiF4. *Chem. Mater.*, 29(19):8202–8210, October 2017. ISSN 0897-4756. doi: 10.1021/acs.chemmater.7b02286.

[107] Younghee Lee, Jaime W. DuMont, and Steven M. George. Mechanism of Thermal Al2O3 Atomic Layer Etching Using Sequential Reactions with Sn(acac)2 and HF. *Chem. Mater.*, 27(10):3648–3657, 2015. ISSN 0897-4756. doi: 10.1021/acs.chemmater.5b00300.

[108] Younghee Lee, Craig Huffman, and Steven M. George. Selectivity in Thermal Atomic Layer Etching Using Sequential, Self-Limiting Fluorination and Ligand-Exchange Reactions. *Chem. Mater.*, 28(21):7657–7665, November 2016. ISSN 0897-4756. doi: 10.1021/acs.chemmater.6b02543.

[109] Thorsten Lill, Keren J. Kanarik, Samantha Tan, Meihua Shen, Eric Hudson, Yang Pan, Jeffrey Marks, Vahid Vahedi, and Richard A. Gottscho. Atomic Layer Etching: Directional. In *Encyclopedia of Plasma Technology*, pages 133–142. CRC Press, Boca Raton, FL, USA, December 2016. ISBN 978-1-35120495-8. doi: 10.1081/E-EPLT-120053939.

[110] Lucas P. B. Lima, Milena A. Moreira, José A. Diniz, and Ioshiaki Doi. Titanium nitride as promising gate electrode for MOS technology. *Phys. Status Solidi C*, 9(6):1427–1430, 2012. ISSN 1862-6351. doi: 10.1002/pssc.201100506.

[111] F. London and H. London. The electromagnetic equations of the supraconductor. *Proc. A.*, 149(866):71–88, March 1935. ISSN 0080-4630. doi: 10.1098/rspa.1935.0048.

[112] A. V. Lubenchenko, A. A. Batrakov, I. V. Shurkaeva, A. B. Pavolotsky, S. Krause, D. A. Ivanov, and O. I. Lubenchenko. XPS Study of Niobium and Niobium-Nitride Nanofilms. *J. Surf. Invest.*, 12(4):692–700, July 2018. doi: 10.1134/S1027451018040134.

[113] Peng Luo and Yihui Zhao. Niobium Nitride Preparation for Superconducting Single-Photon Detectors. *Molecules*, 28(17):6200, August 2023. doi: 10.3390/molecules28176200.

[114] J. Luthin and Ch. Linsmeier. Characterization of Electron Beam Evaporated Carbon Films and Compound Formation on Titanium and Silicon. *Physica Scripta*, 91(1):134–137, 2001. ISSN 0281-1847. doi: 10.1238/Physica.Topical.091a00134.

[115] Monzer Maarouf, Muhammad Baseer Haider, Qasem Ahmed Drmosh, and Mogtaba B. Mekki. X-Ray Photoelectron Spectroscopy Depth Profiling of As-Grown and Annealed Titanium Nitride Thin Films. *Crystals*, 11(3):239, 2021. ISSN 2073-4352. doi: 10.3390/cryst11030239.

[116] Bart Macco and W. M. M. (Erwin) Kessels. Atomic layer deposition of conductive and semiconductive oxides. *Appl. Phys. Rev.*, 9(4), December 2022. doi: 10.1063/5.0116732.

[117] P. A. Maki and D. J. Ehrlich. Laser bilayer etching of GaAs surfaces. *Appl. Phys. Lett.*, 55(2):91–93, July 1989. ISSN 0003-6951. doi: 10.1063/1.102097.

[118] M. D. Malev and D. C. Weisser. Oxygen desorption during niobium sputtering for superconducting RF accelerators. *Nucl. Instrum. Methods Phys. Res., Sect. A*, 364(3):409–415, October 1995. doi: 10.1016/0168-9002(95)00476-9.

[119] Anatolii A. Malygin, Victor E. Drozd, Anatolii A. Malkov, and Vladimir M. Smirnov. From V. B. Aleskovskii's "Framework" Hypothesis to the Method of Molecular Layering/Atomic Layer Deposition. *Chem. Vap. Deposition*, 21 (10-11-12):216–240, December 2015. ISSN 1521-3862. doi: 10.1002/cvde.201502013.

[120] Miguel Manzo-Perez, Moeid Jamalzadeh, Zhujun Huang, Xiao Tong, Kim Kisslinger, Dmytro Nykypanchuk, and Davood Shahrjerdi. Effects of residual oxygen on superconducting niobium films. *Appl. Phys. Lett.*, 125(11):112602, September 2024. doi: 10.1063/5.0225589.

[121] T. Matsukawa, K. Endo, H. Akasaka, Y. Kamiya, M. Ikeda, K. Tsunekawa, T. Nakagawa, Y. X. Liu, and M. Masahara. Variability suppression of FinFETs by smoothing sidewall roughness using ion beam etching technology. In *2015 Silicon Nanoelectronics Workshop (SNW)*, pages 1–2. IEEE, Japan, 2015. URL https://ieeexplore.ieee.org/abstract/document/7275280.

[122] Robert J. Mattauch. Optimization of SIS mixer elements. *NASA Contractor Report*, page 01298, December 1985. URL https://ui.adsabs.harvard.edu/abs/1985ntrs.rept01298M/abstract.

[123] Benjamin A. Mazin. Superconducting Materials for Microwave Kinetic Inductance Detectors. *arXiv*, April 2020. doi: 10.48550/arXiv.2004.14576.

[124] W. L. McMillan. Transition Temperature of Strong-Coupled Superconductors. *Phys. Rev.*, 167(2):331–344, March 1968. doi: 10.1103/PhysRev.167.331.

[125] Owen Medeiros, Marco Colangelo, Ilya Charaev, and Karl K. Berggren. Measuring thickness in thin NbN films for superconducting devices. *J. Vac. Sci. Technol., A*, 37(4), July 2019. doi: 10.1116/1.5088061.

[126] W. Meissner and R. Ochsenfeld. Ein neuer Effekt bei Eintritt der Supraleitfähigkeit. *Naturwissenschaften*, 21(44):787–788, November 1933. ISSN 1432-1904. doi: 10.1007/BF01504252.

[127] F. P. Mena, J. W. Kooi, A. M. Baryshev, C. F. J. Lodewijk, R. Hesper, W. Wild, and T. M. Klapwijk. An SIS-based sideband-separating heterodyne mixer optimized for the 600 to 720 GHz band. *J. Phys. Conf. Ser.*, 97(1):012331, February 2008. ISSN 1742-6596. doi: 10.1088/1742-6596/97/1/012331.

[128] Dominik Metzler, Chen Li, C. Steven Lai, Eric A. Hudson, and Gottlieb S. Oehrlein. Investigation of thin oxide layer removal from Si substrates using an SiO2 atomic layer etching approach: the importance of the reactivity of the substrate. *J. Phys. D: Appl. Phys.*, 50(25):254006, 2017. ISSN 0022-3727. doi: 10.1088/1361-6463/aa71f1.

[129] Nobuya Miyoshi, Hiroyuki Kobayashi, Kazunori Shinoda, Masaru Kurihara, Tomoyuki Watanabe, Yutaka Kouzuma, Kenetsu Yokogawa, Satoshi Sakai, and Masaru Izawa. Atomic layer etching of silicon nitride using infrared annealing for short desorption time of ammonium fluorosilicate. *Jpn. J. Appl. Phys.*, 56(6S2):06HB01, 2017. ISSN 1347-4065. doi: 10.7567/JJAP.56.06HB01.

[130] Nobuya Miyoshi, Nicholas McDowell, and Hiroyuki Kobayashi. Atomic layer etching of titanium nitride with surface modification by Cl radicals and rapid thermal annealing. *J. Vac. Sci. Technol., A*, 40(3):032601, April 2022. doi: 10.1116/6.0001827.

[131] Elham Mohimi, Xiaoqing I. Chu, Brian B. Trinh, Shaista Babar, Gregory S. Girolami, and John R. Abelson. Thermal Atomic Layer Etching of Copper by Sequential Steps Involving Oxidation and Exposure to Hexafluoroacetylacetone. *ECS J. Solid State Sci. Technol.*, 7(9):P491, August 2018. doi: 10.1149/2.0211809jss.

[132] G. Morello, M. Quaglio, G. Meneghini, C. Papuzza, and C. Kompocholis. Reactive ion etching induced damage evaluation for optoelectronic device fabrication. *J. Vac. Sci. Technol. B*, 24(2):756–761, March 2006. ISSN 1071-1023. doi: 10.1116/1.2181576.

[133] Victor Moshchalkov, Mariela Menghini, T. Nishio, Q. H. Chen, A. V. Silhanek, V. H. Dao, L. F. Chibotaru, N. D. Zhigadlo, and J. Karpinski. Type-1.5 Superconductivity. *Phys. Rev. Lett.*, 102(11):117001, March 2009. doi: 10.1103/PhysRevLett.102.117001.

[134] Christine Mousty-Desbuquoit, Joseph Riga, and Jacques J. Verbist. Electronic structure of titanium(III) and titanium(IV) halides studied by solid-phase x-ray photoelectron spectroscopy. *Inorg. Chem.*, 26(8):1212–1217, 1987. ISSN 0020-1669. doi: 10.1021/ic00255a008.

[135] J. Musschoot, Q. Xie, D. Deduytsche, S. Van den Berghe, R. L. Van Meirhaeghe, and C. Detavernier. Atomic layer deposition of titanium nitride from TDMAT precursor. *Microelectron. Eng.*, 86(1):72–77, 2009. ISSN 0167-9317. doi: 10.1016/j.mee.2008.09.036.

[136] Lars-Åke Näslund, Per O. Å. Persson, and Johanna Rosen. X-ray Photoelectron Spectroscopy of Ti3AlC2, Ti3C2Tz, and TiC Provides Evidence for the Electrostatic Interaction between Laminated Layers in MAX-Phase Materials. *J. Phys. Chem. C*, 124(50):27732–27742, 2020. ISSN 1932-7447. doi: 10.1021/acs.jpcc.0c07413.

[137] Jun Nagamatsu, Norimasa Nakagawa, Takahiro Muranaka, Yuji Zenitani, and Jun Akimitsu. Superconductivity at 39 K in magnesium diboride. *Nature*, 410:63–64, March 2001. ISSN 1476-4687. doi: 10.1038/35065039.

[138] Michio Naito and Kenji Ueda. MgB2 thin films for superconducting electronics. *Supercond. Sci. Technol.*, 17(7):R1, May 2004. ISSN 0953-2048. doi: 10.1088/0953-2048/17/7/R01.

[139] Varun Natu, Mohamed Benchakar, Christine Canaff, Aurélien Habrioux, Stéphane Célérier, and Michel W. Barsoum. A critical analysis of the X-ray photoelectron spectra of Ti3C2Tz MXenes. *Matter*, 4(4):1224–1251, 2021. ISSN 2590-2393. doi: 10.1016/j.matt.2021.01.015.

[140] D. M. Neumark, A. M. Wodtke, G. N. Robinson, C. C. Hayden, and Y. T. Lee. Molecular beam studies of the F+H2 reaction. *J. Chem. Phys.*, 82(7): 3045–3066, April 1985. doi: 10.1063/1.448254.

[141] Satoru Noguchi, Akihiro Kuribayashi, Tatsunori Oba, Hiroki Iriuda, Yoshitomo Harada, Masato Yoshizawa, Shigehito Miki, Hisashi Shimakage, Zhen Wang, Kazuo Satoh, Tsutomu Yotsuya, and Takekazu Ishida. Systematic characterization of upper critical fields forMgB2 thin films by means of the two-band superconducting theory. *Supercond. Sci. Technol.*, 22(5):055004, March 2009. ISSN 0953-2048. doi: 10.1088/0953-2048/22/5/055004.

[142] Minoru Obara and Tomoo Fujioka. Time-Resolved Spectroscopic Studies on the TE HF Chemical Lasers Using the Mixtures of SF6/H2 and SF6/CH4. *Jpn. J. Appl. Phys.*, 13(4):675, April 1974. doi: 10.1143/JJAP.13.675.

[143] G. S. Oehrlein, D. Metzler, and C. Li. Atomic Layer Etching at the Tipping Point: An Overview. *ECS J. Solid State Sci. Technol.*, 4(6):N5041, March 2015. ISSN 2162-8777. doi: 10.1149/2.0061506jss.

[144] Gottlieb S. Oehrlein, Stephan M. Brandstadter, Robert L. Bruce, Jane P. Chang, Jessica C. DeMott, Vincent M. Donnelly, Rémi Dussart, Andreas Fischer, Richard A. Gottscho, Satoshi Hamaguchi, Masanobu Honda, Masaru Hori, Kenji Ishikawa, Steven G. Jaloviar, Keren J. Kanarik, Kazuhiro Karahashi, Akiteru Ko, Hiten Kothari, Nobuyuki Kuboi, Mark J. Kushner,

Thorsten Lill, Pingshan Luan, Ali Mesbah, Eric Miller, Shoubhanik Nath, Yoshinobu Ohya, Mitsuhiro Omura, Chanhoon Park, John Poulose, Shahid Rauf, Makoto Sekine, Taylor G. Smith, Nathan Stafford, Theo Standaert, and Peter L. G. Ventzek. Future of plasma etching for microelectronics: Challenges and opportunities. *J. Vac. Sci. Technol., B*, 42(4), July 2024. ISSN 2166-2746. doi: 10.1116/6.0003579.

[145] Tomihito Ohba, Wenbing Yang, Samantha Tan, Keren J. Kanarik, and Kazuo Nojiri. Atomic layer etching of GaN and AlGaN using directional plasma-enhanced approach. *Jpn. J. Appl. Phys.*, 56(6S2):06HB06, 2017. ISSN 1347-4065. doi: 10.7567/JJAP.56.06HB06.

[146] Heike Kamerlingh Onnes. The resistance of pure mercury at helium temperatures. *Phys. Lab. Univ. Leiden*, 12:120, March 1911.

[147] P. A. Pankratiev, Yu V. Barsukov, A. A. Kobelev, A. Ya Vinogradov, I. V. Miroshnikov, and A. S. Smirnov. Etching of Si3N4 by SF6/H2 and SF6/D2 plasmas. *J. Phys. Conf. Ser.*, 1697(1):012222, December 2020. ISSN 1742-6596. doi: 10.1088/1742-6596/1697/1/012222.

[148] S. D. Park, C. K. Oh, J. W. Bae, G. Y. Yeom, T. W. Kim, J. I. Song, and J. H. Jang. Atomic layer etching of InP using a low angle forward reflected Ne neutral beam. *Appl. Phys. Lett.*, 89(4):043109, July 2006. doi: 10.1063/1.2221504.

[149] S. J. Pearton, A. Katz, and A. Feingold. Hybrid electron cyclotron resonance-RF plasma etching of TiNx thin films grown by low pressure rapid thermal metalorganic chemical vapour deposition. *Semicond. Sci. Technol.*, 6(8):830, 1991. ISSN 0268-1242. doi: 10.1088/0268-1242/6/8/022.

[150] Martin H. P. Pfeiffer, Junqiu Liu, Arslan S. Raja, Tiago Morais, Bahareh Ghadiani, and Tobias J. Kippenberg. Ultra-smooth silicon nitride waveguides based on the Damascene reflow process: fabrication and loss origins. *Optica*, 5(7):884–892, July 2018. ISSN 2334-2536. doi: 10.1364/OPTICA.5.000884.

[151] Marissa D. Piña, Matthew P. Whalen, John Q. Xiao, and Andrew V. Teplyakov. Thermal Atomic Layer Etching Process for 2D van der Waals Material CrPS4. *Chem. Mater.*, 36(16):8056–8065, August 2024. doi: 10.1021/acs.chemmater.4c01606.

[152] H. B. Profijt, S. E. Potts, M. C. M. van de Sanden, and W. M. M. Kessels. Plasma-Assisted Atomic Layer Deposition: Basics, Opportunities, and Challenges. *J. Vac. Sci. Technol., A*, 29(5):050801, August 2011. ISSN 0734-2101. doi: 10.1116/1.3609974.

[153] Thomas Proslier, J. Klug, Nicholas C. Becker, Jeffrey W. Elam, and Michael Pellin. (Invited) Atomic Layer Deposition of Superconductors. *ECS Trans.*, 41(2):237, 2011. ISSN 1938-5862. doi: 10.1149/1.3633673.

[154] A. Prudnikava, Y. Tamashevich, A. Makarova, D. Smirnov, and J. Knobloch. In-situ synchrotron x-ray photoelectron spectroscopy study of medium-temperature baking of niobium for SRF application. *Supercond. Sci. Technol.*, 37(7):075007, June 2024. doi: 10.1088/1361-6668/ad4825.

[155] Riikka L. Puurunen. Surface chemistry of atomic layer deposition: A case study for the trimethylaluminum/water process. *J. Appl. Phys.*, 97(12): 121301, June 2005. ISSN 0021-8979. doi: 10.1063/1.1940727.

[156] Riikka L. Puurunen. A Short History of Atomic Layer Deposition: Tuomo Suntola's Atomic Layer Epitaxy. *Chem. Vap. Deposition*, 20(10-11-12):332–344, October 2014. ISSN 1521-3862. doi: 10.1002/cvde.201402012.

[157] Keith G. Ray, Leonard E. Klebanoff, Vitalie Stavila, ShinYoung Kang, Liwen F. Wan, Sichi Li, Tae Wook Heo, Mark D. Allendorf, Jonathan R. I. Lee, Alexander A. Baker, and Brandon C. Wood. Understanding Hydrogenation Chemistry at MgB2 Reactive Edges from Ab Initio Molecular Dynamics. *ACS Appl. Mater. Interfaces*, 14(18):20430–20442, May 2022. ISSN 1944-8244. doi: 10.1021/acsami.1c23524.

[158] John M. Rowell. The widely variable resistivity of MgB2 samples. *Supercond. Sci. Technol.*, 16(6):R17, April 2003. ISSN 0953-2048. doi: 10.1088/0953-2048/16/6/201.

[159] Naresh C. Saha and Harland G. Tompkins. Titanium nitride oxidation chemistry: An x-ray photoelectron spectroscopy study. *J. Appl. Phys.*, 72(7): 3072–3079, 1992. ISSN 0021-8979. doi: 10.1063/1.351465.

[160] Hiroyuki Sakaue, Seiji Iseda, Kazushi Asami, Jirou Yamamoto, Masataka Hirose, and Yasuhiro Horiike. Atomic Layer Controlled Digital Etching of Silicon. *Jpn. J. Appl. Phys.*, 29(11R):2648, 1990. ISSN 1347-4065. doi: 10.1143/JJAP.29.2648.

[161] Martin Sandberg, Michael R. Vissers, Jeffrey S. Kline, Martin Weides, Jiansong Gao, David S. Wisbey, and David P. Pappas. Etch induced microwave losses in titanium nitride superconducting resonators. *Appl. Phys. Lett.*, 100 (26), 2012. ISSN 0003-6951. doi: 10.1063/1.4729623.

[162] Xia Sang, Yantao Xia, Philippe Sautet, and Jane P. Chang. Atomic layer etching of metals with anisotropy, specificity, and selectivity. *J. Vac. Sci. Technol., A*, 38(4):043005, June 2020. ISSN 0734-2101. doi: 10.1116/6.0000225.

[163] F. Santerre, M. A. El Khakani, M. Chaker, and J. P. Dodelet. Properties of TiC thin films grown by pulsed laser deposition. *Appl. Surf. Sci.*, 148(1): 24–33, 1999. ISSN 0169-4332. doi: 10.1016/S0169-4332(99)00139-7.

[164] Louis Schlapbach and Andreas Züttel. Hydrogen-storage materials for mobile applications. *Nature*, 414:353–358, November 2001. ISSN 1476-4687. doi: 10.1038/35104634.

[165] A. Serquis, Y. T. Zhu, D. E. Peterson, F. M. Mueller, R. K. Schulze, V. F. Nesterenko, and S. S. Indrakanti. Degradation of MgB2 under ambient environment. *Appl. Phys. Lett.*, 80(23):4401–4403, June 2002. ISSN 0003-6951. doi: 10.1063/1.1481548.

[166] Sidney Shapiro. Josephson Currents in Superconducting Tunneling: The Effect of Microwaves and Other Observations. *Phys. Rev. Lett.*, 11(2):80–82, July 1963. doi: 10.1103/PhysRevLett.11.80.

[167] Abigail Shearrow, Gerwin Koolstra, Samuel J. Whiteley, Nathan Earnest, Peter S. Barry, F. Joseph Heremans, David D. Awschalom, Erik Shirokoff, and David I. Schuster. Atomic layer deposition of titanium nitride for quantum circuits. *Appl. Phys. Lett.*, 113(21), November 2018. ISSN 0003-6951. doi: 10.1063/1.5053461.

[168] Ryan Sheil, J. Mark P. Martirez, Xia Sang, Emily A. Carter, and Jane P. Chang. Precise Control of Nanoscale Cu Etching via Gas-Phase Oxidation and Chemical Complexation. *J. Phys. Chem. C*, 125(3):1819–1832, January 2021. doi: 10.1021/acs.jpcc.0c08932.

[169] Hiroyuki Shibata. Fabrication of a MgB2 nanowire single-photon detector using Br2–N2 dry etching. *Appl. Phys. Express*, 7(10):103101, September 2014. ISSN 1882-0786. doi: 10.7567/APEX.7.103101.

[170] Hiroyuki Shibata, Tatsushi Akazaki, and Yasuhiro Tokura. Fabrication of MgB2 Nanowire Single-Photon Detector with Meander Structure. *Appl. Phys. Express*, 6(2):023101, February 2013. ISSN 1882-0786. doi: 10.7567/APEX.6.023101.

[171] Dahee Shim, Jihyun Kim, Yongjae Kim, and Heeyeop Chae. Plasma atomic layer etching for titanium nitride at low temperatures. *Journal of Vacuum Science & Technology B, Nanotechnology and Microelectronics: Materials, Processing, Measurement, and Phenomena*, 40(2):022208, February 2022. ISSN 2166-2746. doi: 10.1116/6.0001602.

[172] Y. M. Shy, L. E. Toth, and R. Somasundaram. Superconducting properties, electrical resistivities, and structure of NbN thin films. *J. Appl. Phys.*, 44 (12):5539–5545, December 1973. doi: 10.1063/1.1662193.

[173] Eun-Jin Song, Ji-Hye Kim, Jung-Dae Kwon, Se-Hun Kwon, and Ji-Hoon Ahn. Silicon atomic layer etching by two-step plasma process consisting of oxidation and modification to form (NH4)2SiF6, and its sublimation. *Jpn. J. Appl. Phys.*, 57(10):106505, 2018. ISSN 1347-4065. doi: 10.7567/JJAP.57.106505.

[174] Mark J. Sowa, Yonas Yemane, Jinsong Zhang, Johanna C. Palmstrom, Ling Ju, Nicholas C. Strandwitz, Fritz B. Prinz, and J. Provine. Plasma-enhanced atomic layer deposition of superconducting niobium nitride. *J. Vac. Sci. Technol., A*, 35(1):01B143, December 2016. ISSN 0734-2101. doi: 10.1116/1.4972858.

[175] Ilya A. Stepanov, Aleksandr S. Baburin, Danil V. Kushnev, Evgeniy V. Sergeev, Oksana I. Shmonina, Aleksey R. Matanin, Vladimir V. Echeistov, Ilya A. Ryzhikov, Yuri V. Panfilov, and Ilya A. Rodionov. Sputtered NbN films for ultrahigh performance superconducting nanowire single-photon detectors. *APL Mater.*, 12(2), February 2024. doi: 10.1063/5.0188420.

[176] Tuomo Suntola and Jorma Antson. Method for producing compound thin films. US Patent, November 1975.

[177] J. Tucker. Quantum limited detection in tunnel junction mixers. *IEEE J. Quantum Electron.*, 15(11):1234–1258, November 1979. doi: 10.1109/JQE.1979.1069931.

[178] John R. Tucker and Marc J. Feldman. Quantum detection at millimeter wavelengths. *Rev. Mod. Phys.*, 57(4):1055–1113, October 1985. doi: 10.1103/RevModPhys.57.1055.

[179] J. L. van Hemmen, S. B. S. Heil, J. H. Klootwijk, F. Roozeboom, C. J. Hodson, M. C. M. van de Sanden, and W. M. M. Kessels. Plasma and Thermal ALD of Al2O3 in a Commercial 200 mm ALD Reactor. *J. Electrochem. Soc.*, 154 (7):G165, May 2007. doi: 10.1149/1.2737629.

[180] A. Verevkin, J. Zhang, Roman Sobolewski, A. Lipatov, O. Okunev, G. Chulkova, A. Korneev, K. Smirnov, G. N. Gol'tsman, and A. Semenov. Detection efficiency of large-active-area NbN single-photon superconducting detectors in the ultraviolet to near-infrared range. *Appl. Phys. Lett.*, 80(25): 4687–4689, June 2002. doi: 10.1063/1.1487924.

[181] M. R. Vissers, J. Gao, D. S. Wisbey, D. A. Hite, C. C. Tsuei, A. D. Corcoles, M. Steffen, and D. P. Pappas. Low loss superconducting titanium nitride coplanar waveguide resonators. *Appl. Phys. Lett.*, 97(23), 2010. ISSN 0003-6951. doi: 10.1063/1.3517252.

[182] Vladimir Volynets, Yuri Barsukov, Gonjun Kim, Ji-Eun Jung, Sang Ki Nam, Kyuhee Han, Shuo Huang, and Mark J. Kushner. Highly selective Si3N4/SiO2 etching using an NF3/N2/O2/H2 remote plasma. I. Plasma source and critical fluxes. *J. Vac. Sci. Technol., A*, 38(2):023007, January 2020. ISSN 0734-2101. doi: 10.1116/1.5125568.

[183] M. Mitchell Waldrop. The chips are down for Moore's law. *Nature News*, 530:144, February 2016. doi: 10.1038/530144a.

[184] Danqing Wang, Yufeng Wu, Naomi Pieczulewski, Prachi Garg, Manuel C. C. Pace, Charlotte G. L. Bøttcher, Baishakhi Mazumder, David A. Muller, and Hong X. Tang. All-nitride superconducting qubits based on atomic layer deposition. *Nat. Mater.*, pages 1–6, January 2026. ISSN 1476-4660. doi: 10.1038/s41563-025-02448-8.

[185] Haozhe Wang, Azmain Hossain, David Catherall, and Austin J. Minnich. Isotropic plasma-thermal atomic layer etching of aluminum nitride using SF6 plasma and Al(CH3)3. *J. Vac. Sci. Technol., A*, 41(3), May 2023. doi: 10.1116/6.0002476.

[186] Jakob G. Wenninger. *Fabrication and DC Characterization of SIS Junctions for Applications in Sub-/Millimetre Astronomy*. PhD thesis, University of Manchester, School of Physics and Astronomy, 2019.

[187] Marc Wenskat, Jakub Čižek, Maciej Oskar Liedke, Maik Butterling, Martin Stiehl, Guilherme Dalla Lana Semione, Constanze Backes, Christopher Bate, Oksana Melikhova, Eric Hirschmann, Andreas Wagner, Hans Weise, Andreas Stierle, Martin Aeschlimann, and Wolfgang Hillert. Vacancy dynamics in niobium and its native oxides and their potential implications for quantum computing and superconducting accelerators. *Phys. Rev. B*, 106(9):094516, September 2022. doi: 10.1103/PhysRevB.106.094516.

[188] N. R. Werthamer, E. Helfand, and P. C. Hohenberg. Temperature and Purity Dependence of the Superconducting Critical Field, H_{c2}. III. Electron Spin and Spin-Orbit Effects. *Phys. Rev.*, 147(1):295–302, July 1966. doi: 10.1103/PhysRev.147.295.

[189] Lue Wu, Maodong Gao, Jin-Yu Liu, Hao-Jing Chen, Kellan Colburn, Henry A. Blauvelt, and Kerry J. Vahala. Hydroxyl ion absorption in on-chip high-Q resonators. *Opt. Lett.*, 48(13):3511–3514, July 2023. ISSN 1539-4794. doi: 10.1364/OL.492067.

[190] Wenyi Xie, Paul C. Lemaire, and Gregory N. Parsons. Thermally Driven Self-Limiting Atomic Layer Etching of Metallic Tungsten Using WF6 and O2. *ACS Appl. Mater. Interfaces*, 10(10):9147–9154, March 2018. doi: 10.1021/acsami.7b19024.

[191] Ziqin Yang, Xiangyang Lu, Weiwei Tan, Jifei Zhao, Deyu Yang, Yujia Yang, Yuan He, and Kui Zhou. XPS studies of nitrogen doping niobium used for accelerator applications. *Appl. Surf. Sci.*, 439:1119–1126, May 2018. doi: 10.1016/j.apsusc.2017.12.214.

[192] Taner Yildirim. The surprising superconductor. *Mater. Today*, 5(4):40–44, April 2002. ISSN 1369-7021. doi: 10.1016/S1369-7021(02)05424-X.

[193] Max N. Yoder. Atomic layer etching. US Patent, July 1988.

[194] Iryna Zaytseva, Aleksander Abaloszew, Bruno C. Camargo, Yevgen Syryanyy, and Marta Z. Cieplak. Upper critical field and superconductor-metal transition in ultrathin niobium films. *Sci. Rep.*, 10(19062):19062, November 2020. ISSN 2045-2322. doi: 10.1038/s41598-020-75968-9.

[195] H. Y. Zhai, H. M. Christen, L. Zhang, M. Paranthaman, P. H. Fleming, and D. H. Lowndes. Degradation of superconducting properties in MgB2 films by exposure to water. *Supercond. Sci. Technol.*, 14(7):425, July 2001. ISSN 0953-2048. doi: 10.1088/0953-2048/14/7/301.

[196] WeiJun Zhang, LiXing You, Hao Li, Jia Huang, ChaoLin Lv, Lu Zhang, XiaoYu Liu, JunJie Wu, Zhen Wang, and XiaoMing Xie. NbN superconducting nanowire single photon detector with efficiency over 90% at 1550 nm wavelength operational at compact cryocooler temperature. *Sci. China Phys. Mech. Astron.*, 60(12):1–10, December 2017. doi: 10.1007/s11433-017-9113-4.

[197] Weijun Zhang, Qi Jia, Lixing You, Xin Ou, Hao Huang, Lu Zhang, Hao Li, Zhen Wang, and Xiaoming Xie. Saturating Intrinsic Detection Efficiency of Superconducting Nanowire Single-Photon Detectors via Defect Engineering. *Phys. Rev. Appl.*, 12(4):044040, October 2019. doi: 10.1103/PhysRevApplied.12.044040.

[198] Zhiyan Zhang, Zongbiao Ye, Zhijun Wang, Fujun Gou, Bizhou Shen, Andong Wu, Yuan He, Pingni He, Hongbin Wang, Bo Chen, Jianjun Chen, Kun Zhang, and Jianjun Wei. The mechanism study of mixed Ar/O2 plasma-cleaning treatment on niobium surface for work function improvement. *Appl. Surf. Sci.*, 475:143–150, May 2019. doi: 10.1016/j.apsusc.2018.12.156.

[199] Chao Zhao and Jinjuan Xiang. Atomic Layer Deposition (ALD) of Metal Gates for CMOS. *Appl. Sci.*, 9(11):2388, 2019. ISSN 2076-3417. doi: 10.3390/app9112388.

[200] K. Zheng, D. Kowsari, N. J. Thobaben, X. Du, X. Song, S. Ran, E. A. Henriksen, D. S. Wisbey, and K. W. Murch. Nitrogen plasma passivated niobium resonators for superconducting quantum circuits. *Appl. Phys. Lett.*, 120(10):102601, March 2022. doi: 10.1063/5.0082755.

[201] Di Zhu, Linbo Shao, Mengjie Yu, Rebecca Cheng, Boris Desiatov, C. J. Xin, Yaowen Hu, Jeffrey Holzgrafe, Soumya Ghosh, Amirhassan Shams-Ansari, Eric Puma, Neil Sinclair, Neil Sinclair, Christian Reimer, Mian Zhang, Marko Lončar, and Marko Lončar. Integrated photonics on thin-film lithium niobate. *Adv. Opt. Photonics*, 13(2):242–352, June 2021. ISSN 1943-8206. doi: 10.1364/AOP.411024.

[202] Mario Ziegler, Ludwig Fritzsch, Julia Day, Sven Linzen, Solveig Anders, Julia Toussaint, and Hans-Georg Meyer. Superconducting niobium nitride thin films deposited by metal organic plasma-enhanced atomic layer deposition.

Supercond. Sci. Technol., 26(2):025008, December 2012. ISSN 0953-2048. doi: 10.1088/0953-2048/26/2/025008.

[203] Jonas Zmuidzinas, Jacob W. Kooi, Jonathan Kawamura, Goutam Chattopadhyay, Bruce Bumble, Henry G. LeDuc, and Jeffry A. Stern. Development of SIS mixers for 1 THz. In *Proceedings Volume 3357, Advanced Technology MMW, Radio, and Terahertz Telescopes*, volume 3357, pages 53–62. SPIE, July 1998. doi: 10.1117/12.317386.

[204] David R. Zywotko, Jacques Faguet, and Steven M. George. Rapid atomic layer etching of Al2O3 using sequential exposures of hydrogen fluoride and trimethylaluminum with no purging. *J. Vac. Sci. Technol., A*, 36(6), 2018. ISSN 0734-2101. doi: 10.1116/1.5043488.